SAPIENZA
UNIVERSITÀ DI ROMA

Speed of Gravity and Cosmology Constraints from Binary Neutron Stars using Time Delays between Gravitational Waves and Short Gamma-ray Bursts

Facoltà di Scienze Matematiche, Fisiche e Naturali
Laurea Magistrale in Fisica

Leonardo Iampieri
ID number 1845328

Advisor
Prof. Francesco Pannarale Greco

Co-Advisor
Dr. Simone Mastrogiovanni

Academic Year 2022/2023

Thesis defended on 25 September 2023
in front of a Board of Examiners composed by:

Prof. Paolo de Bernardis (chairman)
Prof. Chiara Cammarota
Prof. Giovanni Organtini
Prof. Giulio D'Agostino
Prof. Annalisa Di Bernardino
Prof. Giovanni Batignani
Prof. Neda Ghofraniha

Thesis Reviewer:

Dr. Cristiano Palomba

Speed of Gravity and Cosmology Constraints from Binary Neutron Stars using Time Delays between Gravitational Waves and Short Gamma-ray Bursts
Tesi di Laurea Magistrale. Sapienza University of Rome

This thesis has been typeset by LaTeX and the Sapthesis class.

Author's email: iampieri.1845328@studenti.uniroma1.it

Dedicated to my family.

Contents

Introduction

On August 17th 2017, at 12:41:04.4 UTC [1], the Advanced LIGO and Virgo observatories reported the detection of a Gravitational wave (GW) from a Binary Neutron Star (BNS) merger. Just 1.74 s after the GW luminosity peak, a short Gamma-ray burst (sGRB), named GRB 170817A, was detected by both the Fermi Gamma-ray Burst Monitor and the Anti-Coincidence Shield of the Spectrometer of the International Gamma-Ray Astrophysics Laboratory. This joint detection was the first solid evidence of BNS being precursors to sGRBs, a theory that had remained speculative for years.

GW170817 is a textbook example of how multi-messenger observations of BNS events can be used to study the cosmos and the formation of compact objects. Thanks to the sGRB, it was possible to identify the host galaxy of the BNS source. From the host galaxy, it was possible to measure the redshift of the GW event ($z = 0.009727$). With the BNS luminosity distance, derived solely from the GW signal, and the redshift, inferred from the galaxy, it was possible to measure the expansion rate of the universe, namely the Hubble constant (H_0). Specifically, H_0 was determined to be $70.0^{+12.0}_{-8.0}\ \frac{\text{km}}{s\ \text{Mpc}}$ at a 68% credible interval [2]. Besides the cosmic expansion, it was also possible to obtain stringent constraints on the speed of gravity. This was possible thanks to the measurement of the GW-sGRB time delay.

The enhanced sensitivities for future detector networks are expected to exponentially increase the rate of GW detections. Unfortunately, the current forecast for the number of joint GWs with **identified host galaxy** detections will decrease as the sensitivity of the GW detectors improves. For instance, the ET is designed to detect BNS mergers up to redshifts $z \approx 5$, expecting around 6×10^4 events annually, of which, for hundreds we will jointly detect GW-sGRB, while only for ~ 10 will we be able to identify the host galaxy [3]. In fact, as we detect GWs from distant sources, identifying the host galaxy, especially faint ones, becomes challenging, even if an associated sGRB is detected. During the ET era, BNS events with observed sGRBs but unidentified host galaxies will be commonly observed. Thus, it is crucial to develop methods that are able to study cosmology and speed of gravity even in the absence of a redshift measurement from the source's host.

This thesis has two objectives: The first objective is to check if future GW-sGRB detection will allow us to jointly infer the speed of gravity and prompt time delay distribution using joint observations of time delay and luminosity distances from BNS.

The second objective is to develop a new method to constrain H_0 from joint GW-sGRB detection in the absence of a direct redshift z measurement from the host galaxy. The general idea is to obtain from the observed GW-sGRB time delay an

implicit redshift evaluation, which, when combined with the luminosity distance derived from the GW, can be used for cosmology evaluation.
I will begin the dissertation by introducing, in Chapter 1, the background knowledge on which my thesis work is based. In particular, I will provide an introduction to cosmology and Binary Neutron Star merger emissions: short Gamma-ray burst gravitational waves. I will then conclude this part by describing the detection of GW170817, with its physical consequences, and the main thesis objectives.
In Chapter 2, I will describe how GWs and sGRBs are detected. This is a crucial aspect when simulating joint detection of GWs and sGRBs, I will discuss current and future GW detectors. Then I will present the Gamma-ray detector Fermi-GBM, whose sensitivity was used for this study.
In Chapter 3, I will describe how I generated a mock catalog of joint GW-sGRB detections from future GW detector observing runs (O4, O5, ET). I will begin by describing the simulation of a BNS population. Then, I will discuss how to generate and detect GW and sGRB signals, and I will present the prompt time delay models used for this study. I will then conclude this part with a short description of the simulated catalog.
Then, in Chapter 4, I will show how to infer population parameters from the mock catalogs. To do so, I will present the formalism of Bayesian Hierarchical Inference, which allows us to reconstruct an astrophysical population from observed data. I will then proceed by describing `icarogw`, a Phyton tool developed to perform Hierarchical Bayesian Inference, and I will show how it can be applied to the context of this thesis work.
Finally, in Chapter 5, I will present forecasts for the inference of cosmology, prompt time delay distribution, and speed of gravity from the mock catalogs generated according to Chapter 3. I will briefly present the priors used for the analysis, and then I will discuss which combination of these population parameters we will be able to infer: the speed of gravity, the cosmology, and the prompt time delay distribution.

Chapter 1

Introduction to Cosmology, Gravitational Waves and Electromagnetic Counterparts

In this chapter, I will introduce the background knowledge on which my thesis work is based. In Section 1.1, I will provide an introduction to cosmology and some of its open questions [4]. In Section 1.2, I will briefly sum up Binary Neutron Star Mergers (BNS) and their Emission, focusing on short Gamma-ray Bursts (sGRBs) and Gravitational Waves (GWs) [5, 4]. In Section 1.3, I will describe how the expression of the observed time delay between GWs and sGRBs from a BNS merger is affected by possible deviations from General Relativity [6]. In Section 1.4, I will focus on the detection of GW170817 and its main physical consequences [7, 2]. This observation in both gravitational and electromagnetic waves started the age of gravitational-wave multi-messenger astronomy. Finally, in Section 1.5, I will state the main thesis objectives in light of current background.

1.1 Cosmology

The standard cosmological model, commonly referred to as the ΛCDM model, is another successful test of Einstein's General Relativity (GR).
The model incorporates a cosmological constant Λ representative of dark energy and provides a robust description of our observable universe, accounting for its observed accelerated expansion.
The ΛCDM model is based on the so-called Friedmann-Lemaître-Robertson-Walker (FLRW) metric, which describes the universe as homogenous and isotropic on large scales (> 150 Mpc) [4]. A central parameter to the ΛCDM model is the scale factor $a(t)$. The scale factor describes how the universe is expanding with respect to the cosmic time t and can be used to calculate physical distances $D_{\rm phys}(t)$ in terms of comoving distances $D_{\rm com}$, namely

$$D_{\rm phys}(t) = a(t)\, D_{\rm com}. \tag{1.1}$$

The line element of the FLRW metric is:

$$ds^2 = -c^2dt^2 + a^2(t)\left(\frac{dr^2}{1-kr^2} + r^2d\theta^2 + r^2\sin^2\theta d\phi^2\right) \tag{1.2}$$

where r is the comoving distance, c the speed of light, θ and ϕ are the angular coordinates, and the curvature constant k is dimensionless and takes the values $k = 0, \pm 1$. The parameter $k = 0$ represents a geometrically flat universe. Observational evidence such as galaxy survey data or gravitational lensing of the Cosmic Microwave Background [8] points to a flat universe. Thus, for this work, we will assume a flat universe where $k = 0$.
The evolution of the scale factor can be linked to physical quantities through the Einstein equations:

$$G_{\mu\nu} = \frac{8\pi G}{c^4}T_{\mu\nu} \tag{1.3}$$

where G is the Newton's constant, $G_{\mu\nu}$ is the Einstein's tensor and $T_{\mu\nu}$ is the stress-energy tensor. For a homogenous and isotropic universe, the stress-energy tensor is

$$T_{\mu\nu} = \begin{pmatrix} -\rho & 0 & 0 & 0 \\ 0 & P & 0 & 0 \\ 0 & 0 & P & 0 \\ 0 & 0 & 0 & P \end{pmatrix} \tag{1.4}$$

where ρ is the energy density and P the pressure term. The energy density is the sum of all the contributions of dark matter. dark energy, and radiation.
In the flat ΛCDM model, by solving the 00 component of Einstein's equations we obtain:

$$\left(\frac{\dot{a}(t)}{a(t)}\right)^2 = H_0^2\left[\Omega_m(1+z)^3 + \Omega_\Lambda\right] \tag{1.5}$$

where H_0 is the Hubble Constant, i.e. the expansion rate of the universe today (which is also related to the critical density ρ_c through $H_0^2 = \frac{8\pi G}{3}\rho_c$), Ω_m is the current non-relativistic matter density parameter and $\Omega_\Lambda = 1 - \Omega_m$ is the cosmological constant dark energy density parameter.
The Hubble parameter is the expansion rate of the universe and it is defined as

$$\frac{\dot{a}(t)}{a(t)} = H(z) = H_0\sqrt{\Omega_m(1+z)^3 + \Omega_\Lambda} \equiv H_0E(z). \tag{1.6}$$

Another fundamental concept of Cosmology is the redshift. Consider two photons emitted in an infinitesimal time interval dt_s by the same source, propagating towards an observer situated at a fixed comoving distance r from the source. From Eq.1.2, given that light rays traverse null geodesics, we derive the following equation:

$$\int_{t_s+dt_s}^{t_d+dt_d} c\frac{dt}{a(t)} = \int_{t_s}^{t_d} c\frac{dt}{a(t)} \tag{1.7}$$

where t_d and $t_d + dt_d$ represent the arrival times of the two photons to the observer. From this equation, we can deduce that:

$$\frac{dt_d}{a(t_d)} = \frac{dt_s}{a(t_s)} \tag{1.8}$$

Or, equivalently,

$$dt_d = \frac{a(t_d)}{a(t_s)} dt_s = \frac{1}{a(t_s)} dt_s = (1+z) dt_s \tag{1.9}$$

where we chose the scale factor for the present epoch $a(t_d)$ to be 1. Here, z is what is known as the redshift parameter.

1.1.1 Hubble Tension

A significant discrepancy exists observationally between measurements of the Hubble constant derived from the Cosmic Microwave Background (CMB) [9] and those from local observations using Standard Candles [10].
A Standard Candle is an astronomical object with known intrinsic luminosity and for which it is possible to measure the redshift. These sources can be used to measure distances in the universe.
Using the relation between the luminosity in the observed frame $\mathrm{L_{obs}}$ and the one in the source frame $\mathrm{L_s}$

$$\mathrm{L_{obs}} = \frac{d\mathrm{E_{obs}}}{d\mathrm{t_{obs}}} = \frac{1}{1+z} \frac{d[h\nu_{\mathrm{obs}}]}{dt_s} = \frac{1}{(1+z)^2} \frac{d\mathrm{E_s}}{d\mathrm{t_s}}. \tag{1.10}$$

We can write the observed flux $\mathcal{F}$ of the Standard Candle as:

$$\mathcal{F} = \frac{L_{obs}}{4\pi D^2} = \frac{L_s}{4\pi D^2 (1+z)^2} = \frac{L_s}{4\pi D_L^2} \tag{1.11}$$

where D is the proper distance and D_L is the luminosity distance which is defined as:

$$D_L = D(1+z) \tag{1.12}$$

Thus, by comparing the known luminosity of a Standard Candle to its observed flux, we can determine its luminosity distance.
The luminosity distance is a function of both redshift z and Hubble constant H_0 [4]:

$$D_L = \frac{c(1+z)}{H_0} \int_0^z \frac{dz'}{E(z')}. \tag{1.13}$$

In the low redshift limit $z \ll 1$ this equation becomes:

$$\begin{aligned} D_L &= \frac{c(1+z)}{H_0} \int_0^z \frac{dz'}{E(z')} \\ &= \frac{c\, z}{H_0} + ... \end{aligned} \tag{1.14}$$

It then follows that a joint measurement of the spectroscopic redshift and the observed flux will allow us to set constraints on H_0. Type Ia supernova measurements from the Supernova H_0 for the Equation of State Experiment (SH0ES) [10] measured $H_0 = 73.24 \pm 1.74 \ \frac{\mathrm{km}}{s\ \mathrm{Mpc}}$.
Another probe to measure the universe's expansion is the Cosmic Microwave Background (CMB) radiation. The CMB radiation is the afterglow of the Big Bang and it is a snapshot of the universe when it was just 380,000 years old. Analyzing the CMB gives us insight into the early conditions and parameters of the universe,

including H_0.
The Planck satellite, launched by the European Space Agency, provided one of the most precise measurements of the CMB. By studying the spectra of temperature fluctuations of the CMB [9], the inferred value for the Hubble constant was found to be $H_0 = 67.74 \pm 0.46 \ \frac{\text{km}}{s \ \text{Mpc}}$.
However, H_0 measurements using standard candles have yielded different results. In fact, the Planck and SH0ES results exhibit an inconsistency at 3σ level. Fig.1.1 shows how measures of H_0 came to a tension during the years. This discrepancy between the values from different methods is what's referred to as the Hubble tension. The cause of this tension is currently one of the most significant debates in cosmology. The tension might either indicate the presence of new physics at cosmological scales or rise from a hidden systematic in one of the experiments. Gravitational waves open a new avenue to shed light on this tension.

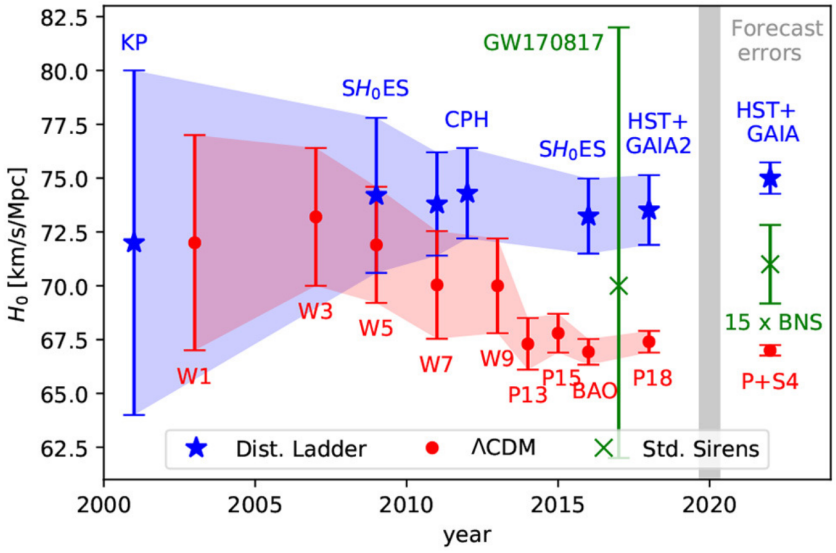

Figure 1.1. Depiction of the Hubble tension. Blue stars correspond to measurements of H0 in the local universe with calibration based on Cepheids. Red dots refer to derived values of H0 from the CMB assuming ΛCDM. Green crosses are direct measurements of H0 with standard sirens. The Figure is adapted from [11].

1.2 Binary Neutron Star Merger

A Binary Neutron Star (BNS) is composed of two Neutron Stars orbiting around each other. Neutron Stars are one the most dense objects in the universe. Each star has a mass of $M_{NS} \sim 1 - 3 \ M_\odot$, radius of $R_{NS} \sim 10 - 12$ km, and an average density of $\rho \sim 10^{14} \frac{\text{g}}{\text{cm}^3}$. We will now outline different types of radiations from BNS that allow for the BNS observation.

1.2.1 Electromagnetic Emission

In a general scenario involving BNS mergers, the emission of electromagnetic (EM) radiation is expected alongside gravitational waves (GWs). The standard model for EM emission is depicted in Fig.1.2 with different EM emission components. Below we describe in general the formation dynamics of the various EM counterparts. The

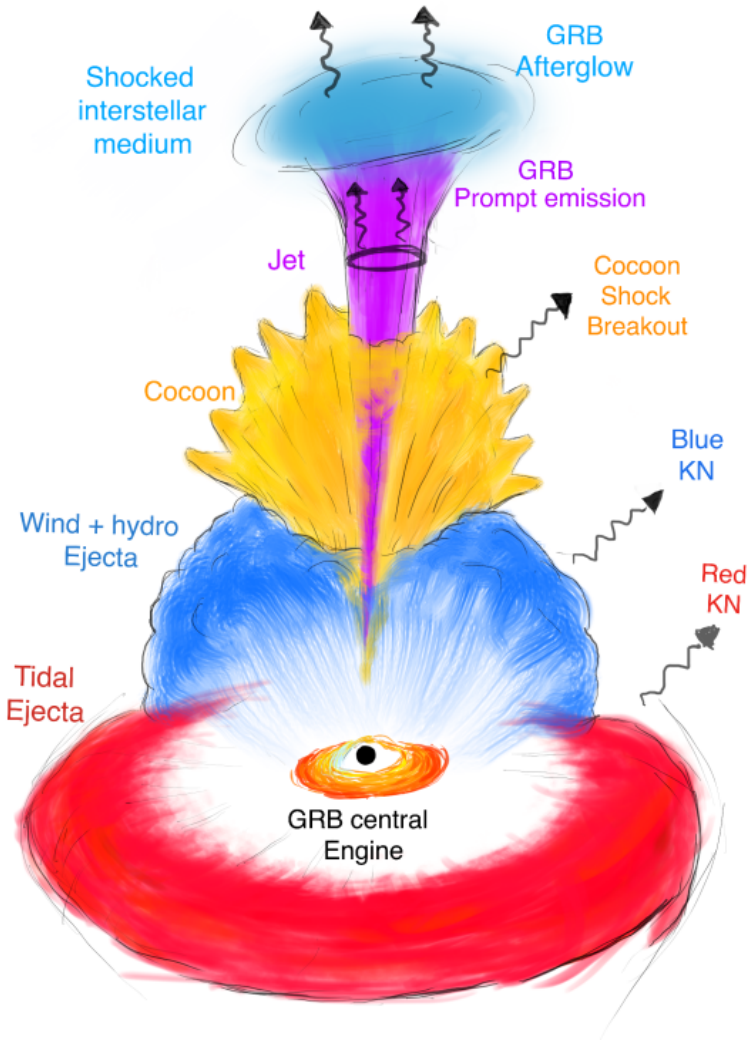

Figure 1.2. Artistic representation of the scenario following BNS merger [5], when an accreting Black Hole is formed. The red component denotes the tidal ejecta, the blue component the hydrodynamic and wind ejecta, the purple component the jet and the yellow component the matter of the ejecta heated by the jet (cocoon). The different components are not represented in scale.

jet of material expelled from the merger moves through a dense circum-burst medium formed by the remaining material of the merger (blue component in Fig.1.2). During this process, the material in front of the jet is heated and moved aside to form a hot structure known as a cocoon (yellow component in Fig.1.2). The cocoon can exert transverse pressure to confine and further collimate the jet [12, 13, 14]. Assuming

sufficient energy, the jet eventually emerges from the surrounding cocoon at a radius on the order of $\sim 10^{10}$ cm. If unsuccessful, the jet can be choked. At the distance range of $10^{13} - 10^{16}$ cm, the jet dissipates part of its kinetic energy by interacting with the interstellar medium. The interaction results in the emission of a gamma-ray burst (GRB). As the jet decelerates, it shocks the interstellar medium (in light blue in Fig. 1.2), resulting in a fading synchrotron emission from X-ray to radio known as the GRB afterglow. It has to be noted that the actual geometry and dissipation mechanics involved in the GRB and its afterglow production still present some open questions.
The remaining matter (blue and red components in Fig. 1.2), emitted during the merger and unbound from the central remnant, is rich of free neutrons and neutron-rich nuclei.
The remnant forms an ideal site for the r-process nucleosynthesis of heavy elements, whose radioactive decay heats the material [15, 16]. The thermal emission from this ejecta generates an EM transient known as a kilonova (KN). Additionally, the shock onto the interstellar medium of these mildly relativistic and sub-relativistic outflows could theoretically power a synchrotron emission, expected to be observable in radio frequencies [17].

1.2.2 Gamma-ray Burst

Gamma-ray bursts are high-energy transient astrophysical sources of extragalactic origin. Their non-thermal spectra peak at energies between 10 keV and 10 MeV. The γ-ray flaring activity, or the prompt emission, typically lasts for less than a hundred seconds showcasing a wide variety of morphologies in its light curve [18]. This prompt emission phase is then followed by a fainter afterglow across the entire EM spectrum that decays in time.
Currently, we classify GRBs in two classes: short GRBs (SGRBs) lasting from ~ 0.3 s to a few seconds and long GRBs (LGRBs) lasting ~ 30 s [19]. SGRBs have a harder spectrum, while LGRBs have a softer spectrum. This indicates that, within the gamma-ray domain, SGRBs exhibit higher energy emissions, while LGRBs display lower energy emissions.
Typically the energetic emission of a GRB is modeled with an isotropic energy, i.e. the energy that the source would emit if it was symmetric. The isotropic equivalent energy of the burst, derived from the γ-ray fluence and the source's distance, can reach $E_{\gamma,\mathrm{ISO}} \approx 10^{54}$ erg for the most energetic GRBs [20, 21]. However, there is compelling evidence to suggest that the emission is not isotropic but beamed [22, 23, 24]. The real energy is thereby reduced by a factor equal to the solid angle of collimation $\frac{\theta^2}{2}$, restricting it to the range $10^{49} - 10^{51}$ erg [24].
SGRBs and LGRBs are sourced by different progenitors, as determined through the studies of the GRB energy, redshift distribution, properties of their afterglow, their host galaxies, and recent observations of gravitational waves (GWs) [25, 26, 27]. On one hand, evidence of supernovae signatures in the late-time optical afterglow of a fraction of LGRBs observations, and the location of LGRBs in bright star-forming regions of their host galaxies suggest that massive stars (masses $M > 20M$) are the progenitors of LGRBs [28, 29].
On the other hand, the progenitors of SGRBs reside in galaxies with a lower star

formation rate and are associated with an older star population. Thus, they are expected to be sourced by older progenitors than those of LGRBs [30]. Astrophysical events that meet the requirements to be progenitors of SGRBs include mergers of NS-NS or NS-BH binaries [31, 32, 33] (see Fig. 1.3).

The first solid evidence of BNS being the progenitors of sGRB came with the joint

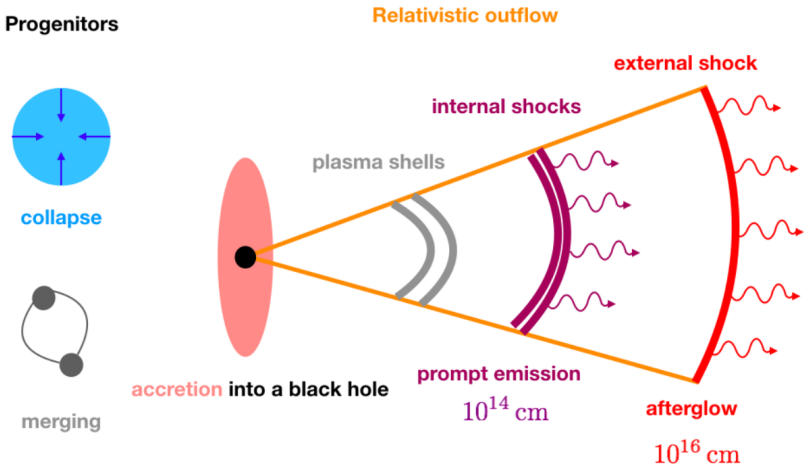

Figure 1.3. representation of the basic model of the GRB [5]: the core-collapse of a massive star or the coalescence of a BNS leads to the formation of an accreting BH, which launches an ultra-relativistic outflow in the form of a jet. Internal dissipation of the jet's kinetic energy through shocks produces the prompt emission in the keV-MeV range. The forward shock of the jet with ambient medium forms the afterglow radiation observed in the X-ray, optical, and radio bands.

detection of the GW signal from the BNS merger, GW170817, by the Advanced LIGO and Virgo interferometers and the sGRB, GRB170817A, by the γ-ray detectors FERMI-GBM and INTEGRAL [7].

1.2.3 Gravitational Waves from Inspiralling Compact Objects

Binary Neutron Stars are also GW sources. GWs are perturbations in the spacetime metric that, according to Einstein's GR, propagate at the speed of light. Being very weak, GWs were only detected in 2015 but now they are rapidly becoming a new way to explore the cosmo. For the sake of brevity, here I will just review some fundamental properties of GWs from BNS mergers. A more complete discussion can be found in [4].

Consider a binary system of two stars moving on a circular orbit around their common center of mass. For simplicity, we will assume that the two stars with masses m_1 and m_2 are point-like and have an orbital separation l_0. The total mass M is defined as

$$M \equiv m_1 + m_2 \tag{1.15}$$

and the reduced mass μ is

$$\mu \equiv \frac{m_1 m_2}{m_1 + m_2}. \tag{1.16}$$

We assume the weak-field, slow-motion approximation to hold, where the orbital motion is described by Newtonian gravity laws. Then, the GW signal emitted at a time t by a binary system moving on a circular orbit, and located at a distance r from the observer, is given by:

$$h_{ij}^{TT}(t,r) = -h_0 \, A_{ij}^{TT}\left(t - \frac{r}{c}\right) \tag{1.17}$$

h_0, the instantaneous wave amplitude, is given by

$$h_0 = \frac{4\mu M G^2}{l_0 c^4 r} \tag{1.18}$$

and $A_{ij}^{TT}\left(t - \frac{r}{c}\right) = P_{ijkl} A^{kl}\left(t - \frac{r}{c}\right)$, where P_{ijkl} is the projector to the Transverse Traceless (TT) gauge (in which the gravitational strain tensor has two degrees of freedom: h_+ and $h_\times$). The tensor A_{ij} is given by:

$$A_{ij} = \begin{pmatrix} \cos 2\omega_K t & \sin 2\omega_K t & 0 \\ \sin 2\omega_K t & -\cos 2\omega_K t & 0 \\ 0 & 0 & 0 \end{pmatrix}, \tag{1.19}$$

where ω_k is the Keplerian orbital speed. The GW is emitted at twice the Keplerian frequency, i.e.

$$\nu_{GW} = 2\nu_K = \frac{\omega_K}{\pi} = \frac{1}{\pi}\sqrt{\frac{GM}{l_0^3}}. \tag{1.20}$$

Fig. 3.1 shows the characteristic time evolution of both the amplitude and frequency of GWs originating from BNS mergers. In the adiabatic regime, where the orbital

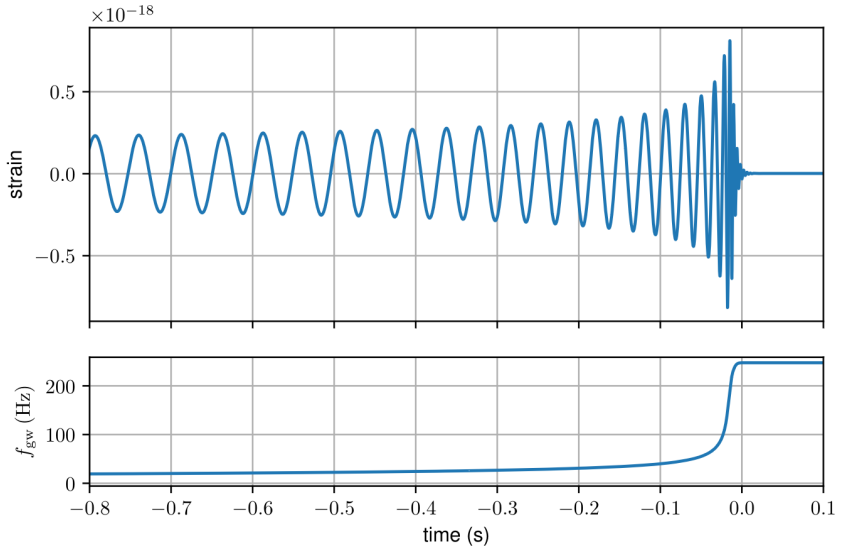

Figure 1.4. GW signal of the compact binary coalescence GW150914. The GW strain (above) and the GW frequency (below) are plotted as a function of the time before merging. The Figure was adapted from [11]

parameters do not change significantly over numerous periods (this condition is met

for BNS systems significantly far from merging), the system compensates for the energy lost in GWs by changing its orbital energy. As a consequence, the orbital separation l_0 decreases with time as:

$$l_0(t) = l_0^{\rm in}\left(1 - \frac{t}{t_c}\right)^{1/4}, \tag{1.21}$$

where $l_0(t=0) = l_{0,\rm in}$ is the orbital separation at some initial time $t = 0$ and t_c is the coalescence time:

$$t_c \equiv \frac{5}{256}\frac{c^5}{G^3}\frac{(l_0^{\rm in})^4}{\mu M^2}. \tag{1.22}$$

As the binary approaches the merger, the orbital frequency decreases and the wave frequency changes as (see Fig.3.1)

$$\nu_{\rm GW}(t) = \nu_{\rm GW}^{\rm in}\left(1 - \frac{t}{t_c}\right)^{-3/8}; \text{where } \nu_{\rm GW}^{\rm in} \equiv \frac{1}{\pi}\sqrt{\frac{GM}{(l_0^{\rm in})^3}} \tag{1.23}$$

If we write Equation (1.23) in the form

$$\nu_{GW}(t) = \nu_{GW}^{\rm in}\left(\frac{t_c}{t_c - t}\right)^{3/8}, \tag{1.24}$$

using Equation (1.22) one can show that

$$\nu_{\rm GW}^{\rm in} t_c^{3/8} = \frac{5^{3/8}}{8\pi}\left(\frac{c^3}{GM}\right)^{5/8}, \tag{1.25}$$

and $\nu_{\rm GW}(t)$ can be written as

$$\nu_{\rm GW}(t) = \frac{5^{3/8}}{8\pi}\left(\frac{c^3}{GM}\right)^{5/8}\left[\frac{1}{t_c - t}\right]^{3/8}. \tag{1.26}$$

In addition, since the orbital distance decreases according to Eq. (1.21), from Eq. (1.18) it follows that the wave amplitude changes with time as

$$h_0(t) = \frac{4\mu M G^2}{l_0(t)c^4 r} = \frac{4\mu M G}{rc^4}\frac{\omega_K(t)^{2/3}}{G^{1/3}M^{1/3}} = \frac{4\pi^{2/3}G^{5/3}\mathcal{M}^{5/3}}{rc^4}\nu_{GW}^{2/3}. \tag{1.27}$$

Where we define

$$\mathcal{M} = \mu^{3/5}M^{2/5} = \frac{(m_1 m_2)^{3/5}}{M^{1/5}}. \tag{1.28}$$

as the chirp mass of the binary. Eqs. (1.23) and (1.27) demonstrate that the frequency and the amplitude of the emitted signal from a binary system during the inspiral phase increase over time. This characteristic resembles the chirp of a bird, hence the term chirp for both this part of the signal and $\mathcal{M}$.

1.2.4 GWs from Binaries at Cosmological Distance

GWs that travel in an expanding universe display some important characteristics that make them optimal probes to measure the universe's expansion. Here i will derive these properties following [4]. Let me define

$$K = \frac{5^{3/8}}{8\pi}\left(\frac{c^3}{G\mathcal{M}}\right)^{3/8}, \tag{1.29}$$

then, Eq. (1.26) can be rewritten as

$$\nu_{\rm GW}(t) = \frac{K}{(t-t_c)^{3/8}}, \tag{1.30}$$

and

$$\dot{\nu}_{\rm GW} = \frac{3}{8}\frac{K}{(t_c-t)^{11/8}} \rightarrow \dot{\nu}_{\rm GW}\nu_{\rm GW}^{-11/3} = \frac{3}{8}K^{-8/3}. \tag{1.31}$$

Using the definition of K this last equation becomes

$$\left[\frac{8\pi}{5^{3/8}}\left(\frac{GM}{c^3}\right)^{5/8}\right]^{8/3} = \frac{8}{3}\dot{\nu}_{\rm GW}\nu_{\rm GW}^{-11/3} \tag{1.32}$$

which can be solved for $\mathcal{M}$ and gives

$$\mathcal{M} = \frac{c^3}{G}\left(\frac{5}{96}\frac{1}{\pi^{8/3}}\dot{\nu}_{\rm GW}\nu_{\rm GW}^{-11/3}\right)^{3/5}. \tag{1.33}$$

The chirp mass can thus be derived by observing the wave frequency and its time derivative during the inspiralling part of the signal.
When considering a source located at cosmological distance, it is no longer viable to assume the propagation of the gravitational wave in Minkowski's spacetime. The effects of cosmological expansion have to be taken into account. The frequency of the gravitational wave ($\nu_{\rm GW}^{\rm obs}$) measured at the detector will differ from the frequency ($\nu_{\rm GW}$) emitted by the source:

$$\nu_{\rm GW}^{\rm obs} = \frac{\nu_{\rm GW}}{1+z} \tag{1.34}$$

where z represents the usual cosmological redshift. Additionally, the observed time separation between two pulses is rescaled according to $dt_{\rm obs} = (1+z)dt_{\rm em}$. Following Eq.1.33, we can calculate the chirp mass for an observer sitting on earth as

$$\mathcal{M}_{\rm obs} = \frac{c^3}{G}\left[\frac{5}{96}\frac{1}{\pi^{8/3}}\left(\frac{d}{dt_{\rm obs}}\nu_{\rm GW}^{\rm obs}\right)(\nu_{\rm obs})^{-11/3}\right]^{3/5}. \tag{1.35}$$

From Eq.1.34 we derive

$$\left[\left(\frac{d}{dt_{\rm obs}}\nu_{\rm GW}^{\rm obs}\right)(\nu_{\rm GW}^{\rm obs})^{-11/3}\right]^{3/5} = [\nu_{\rm GW}^{-11/3}\dot{\nu}_{\rm GW}]^{3/5} \times (1+z), \tag{1.36}$$

and we can thus express $M_{\rm obs}$ as

$$\mathcal{M}_{\rm obs} = \frac{c^3}{G}\left(\frac{5}{96}\frac{1}{\pi^{8/3}}\nu_{\rm GW}^{-11/3}\dot{\nu}_{\rm GW}\right)^{3/5} \times (1+z) = \mathcal{M} \times (1+z) \tag{1.37}$$

Thus, the observed chirp mass $\mathcal{M}_{\rm obs}$ is related to the true chirp mass $\mathcal{M}$ (given by Eq.1.33) by a redshift factor. In other words, a cosmological observer measures a redshifted mass.
It can be shown [4] that the amplitude of a GW propagating in the curved background of an expanding universe has the same form as that of a wave propagating in Minkowski's space (Eq. 1.27), with the radial distance r replaced by the proper distance D at the time t. Hence, the amplitude of the wave emitted by a compact binary inspiral is

$$h_0(t) = \frac{4\pi^{2/3}G^{5/3}}{c^4} \times \frac{\mathcal{M}}{D} \times \left(\mathcal{M}\nu_{\rm GW}(t)\right)^{2/3}. \tag{1.38}$$

Let us now express Eq.1.38 in terms of detector frequency $\nu_{\rm GW}^{\rm obs}$ and chirp mass $\mathcal{M}_{\rm obs}$. It then follows that

$$\begin{aligned} h_0(t) &= \frac{4\pi^{2/3}G^{5/3}}{c^4} \times \frac{\mathcal{M}_{\rm obs}}{D(1+z)} \times \left(\mathcal{M}_{\rm obs}\nu_{\rm GW}^{\rm obs}\right)^{2/3} \\ &= \frac{4\pi^{2/3}G^{5/3}}{c^4} \times \frac{\mathcal{M}_{\rm obs}}{D_L} \times \left(\mathcal{M}_{\rm obs}\nu_{\rm GW}^{\rm obs}\right)^{2/3}. \end{aligned} \tag{1.39}$$

where $D_L = D(1+z)$ is the luminosity distance of the source.
Let us summarize the main message of this Section. From the GW frequency it is possible to obtain a measure of the redshifted, or detector, chirp mass. Then, from the GW amplitude in Eq.1.39 and the detector chirp mass it is possible to obtain a measure the luminosity distance.
GWs are the only known sources for which it is possible to measure the distance. To get the distance they do not require any sort of calibration. This makes GWs optimal sources for cosmological studies.
However, with GWs we cannot measure the redshift. In this thesis, I will study an innovative method to obtain the redshift information.

1.3 Modified Gravity

One potential solution to address the H_0 tension (see Section 1.1.1) is to consider modifications to GR at cosmological scales. A multitude of modified gravity models have been proposed. GWs can provide a good probe for these models.
In this thesis, I work with models that conserve the usual FLRW background for the cosmic expansion (Eq. 1.2): in other words, gravity acts on a perturbative level on tensor perturbations, namely GWs. We make the assumption that the evolution of the scale factor $a(t)$ adheres to standard ΛCDM cosmology.
We also assume that modifications of gravity act on large scale and therefore they only affect the propagation of the GW and not its emission. The propagation of a GW can be modified in three ways: by changing the speed of gravity, its damping, or adding extra polarizations. Here we focus on modifications of the speed of gravity and leave the rest to GR.
We start with a modified GWs dispersion relation given by

$$g_{\mu\nu}p^\mu p^\nu = -B_\alpha |cp|, \tag{1.40}$$

where $g_{\mu\nu}$ is the metric tensor, while

$$p^\mu = (E/c, \hbar k/a, 0, 0) \tag{1.41}$$

denotes the four-momentum of GWs emitted at $r_{\rm com}$ and propagating radially towards the observer. In this context, k is the comoving (costant) wave number, B_α are parameters encoding GR deviation, while $|p| = \sqrt{g_{ij}p^i p^j} = \hbar k/a$. The dispersion relation in Eq. 1.40 can be rewritten as

$$E^2 = c^2\frac{\hbar^2|k|^2}{a^2} + B_\alpha\left(c\frac{\hbar|k|}{a}\right)^\alpha. \tag{1.42}$$

This dispersion relation depends on the physical momentum $p_{\rm ph} = k/a$. In the absence of the coefficients B_α, Eq. 1.42 reduces to the standard dispersion relation for a massless particle in GR. For $\alpha = 0$ and $B_0 \neq 0$, Eq. 1.42 is the dispersion relation for the massive graviton with $B_0 = m_g^2c^4$ (in eV^2). Different theories predict different values for the coefficients B_α, which generally depend on conformal time [34].
Let us rewrite Eq. 1.42 in term of the GW phase velocity c_T as

$$E^2 = \hbar^2\omega^2 = c_T^2(\eta, k/a)\frac{\hbar^2|k|^2}{a^2}, \tag{1.43}$$

where

$$c_T^2(\eta, k/a) = c^2\left[1 + |B_\alpha|\left(c\frac{\hbar|k|}{a}\right)^{\alpha-2}\right]. \tag{1.44}$$

We expect GWs to travel almost at the speed of light. They thus satisfy

$$|B_\alpha|\left(c\frac{\hbar|k|}{a}\right)^{\alpha-2} \ll 1. \tag{1.45}$$

Then from Eq. 1.43 it follows that

$$\omega \simeq c\frac{|k|}{a} \tag{1.46}$$

This implies that the frequency of the emitted GW $f_{\rm s}^{\rm GW}$ is related to that of the observed GW $f_{\rm d}^{\rm GW}$ by the usual redshift relationship

$$a(t_d)f_{\rm d}^{\rm GW} \simeq a(t_s)f_{\rm s}^{\rm GW} \tag{1.47}$$

where the subscript "s" indicates the source and "d" the detector. We can thus identify the GW redshift with the usual photon redshift z of Eq. 1.9. This allows us to write

$$k \simeq \frac{1}{c}\omega(\eta_{\rm d})a(\eta_{\rm d}) = 2\pi\frac{f_d}{c} \tag{1.48}$$

since today $a(t_0) = 1$. Therefore, the phase velocity obtained from Eq. 1.44 can be expressed in terms of the detected GW frequency as

$$c_T^2(\eta, f_d/a) = c\left[1 + \hat{\alpha}_j\left(\frac{f_d}{a}\right)^j\right], \tag{1.49}$$

where

$$\hat{\alpha}_j = B_{j+2}(2\pi\hbar)^j, \tag{1.50}$$

and $j = \alpha - 2$. The dimensions of $[\alpha^j]$ are Hz^{-j}. The radial propagation velocity of the waves is given by

$$\frac{dr}{dt} = \frac{p^r}{p^t} = c^2 \frac{k}{a} \frac{1}{a\omega} = \frac{\mathrm{v_{GW}}}{a} = \frac{1}{a}\frac{dr}{d\eta} \tag{1.51}$$

where the group velocity $\mathrm{v_{GW}}$ can be written as

$$\mathrm{v_{GW}} \simeq c\left[1 - \frac{\hat{\alpha}_j}{2}\left(\frac{f_d}{a}\right)^j\right]. \tag{1.52}$$

To derive this expression we used the approximation of Eq. 1.45. For instance, for massive gravitons where $j = -2$, we have $\hat{\alpha}_{-2} = B_0(2\pi\hbar)^{-2}$ and $c_T > c$, yet the group velocity $\mathrm{v_{GW}}$ is lower than c.
In this thesis, we will consider $j = 0$, namely modifications of gravity that introduce a GW speed $\neq c$ that does not depend on the frequency of the GW. The fact that the speed of gravity is not c will introduce a time delay between the GW and the EM emission.
By setting $j = 0$ Eq. 1.52 becomes:

$$\mathrm{v_{GW}} \simeq c\left[1 - \frac{\hat{\alpha}_j}{2}\right]. \tag{1.53}$$

it immediately follows that $\hat{\alpha}_0$ can be written as

$$\hat{\alpha}_0 = 2\frac{\mathrm{v_{GW}} - \mathrm{v_{EM}}}{\mathrm{v_{EM}}} \tag{1.54}$$

with $\mathrm{v_{EM}} = c$ the speed of light.
We now compute the time delay at the detector between a GW and GRB emitted at two different conformal time η_s from the same source located at a fixed comoving distance r_{com}. We recall that the definition of conformal time is:

$$\eta_s = \int_0^{t_s} \frac{dt'}{a(t')} \tag{1.55}$$

We begin by considering a GW, which is emitted at η_s^{GW} and received at η_d^{GW}, with a detected frequency f_d^{GW}. Using Eq. 1.52, we can write:

$$r_{\mathrm{com}} = \int_{\eta_s^{\mathrm{GW}}}^{\eta_d^{\mathrm{GW}}} \mathrm{v_{GW}}\, d\eta = \int_{\eta_s^{\mathrm{GW}}}^{\eta_d^{\mathrm{GW}}} c\left[1 - \frac{1}{2}\hat{\alpha}_0\right] d\eta = c\left[1 - \frac{1}{2}\hat{\alpha}_0\right]\left[\eta_s^{\mathrm{GW}} - \eta_s^{\mathrm{GW}}\right] \tag{1.56}$$

Proceeding similarly for the GRB we derive:

$$r_{\mathrm{com}} = \int_{\eta_s^{\mathrm{GRB}}}^{\eta_d^{\mathrm{GRB}}} \mathrm{v_{EM}}\, d\eta = \int_{\eta_s^{\mathrm{GRB}}}^{\eta_d^{\mathrm{GRB}}} c\, d\eta = c\left[\eta_s^{\mathrm{GRB}} - \eta_s^{\mathrm{GRB}}\right]. \tag{1.57}$$

Since the source is at the same comoving distance, we can equate Eq. 1.56 and Eq. 1.57. By doing so, we can write the conformal time delay at the detector between GWs and GRB as:

$$\Delta\eta_d^{\text{GW-GRB}} = \Delta\eta_s^{\text{GW-GRB}} + \frac{1}{2}\int_{\eta_s^{\mathrm{GW}}}^{\eta_d^{\mathrm{GW}}} \hat{\alpha}_0\, d\eta \tag{1.58}$$

To a good approximation, the GWs are emitted and detected on timescales considerably smaller than the cosmological timescale (the variational timescale of a). As a consequence, we can write the time delay, denoted as $\Delta t_d^{\text{GW-GRB}}$, as:

$$\Delta t_d^{\text{GW-GRB}} = (1+z_s)\Delta t_s^{\text{GW-GRB}} + \frac{\hat{\alpha}_0}{2}\mathrm{T}_l \tag{1.59}$$

where $\Delta t_s^{\text{GW-GRB}}$ is the time delay at the source, and T_l is the lookback time, i.e the time elapsed since the light we observe was emitted from a source of redshift z, and is defined as:

$$\mathrm{T}_l = \int_0^z dz' \frac{1}{H_0 E(z')} \tag{1.60}$$

Where, in the low redshift limit $z \ll 1$, the right-hand side of this equation can be rewritten as:

$$\begin{aligned} \mathrm{T}_l &= \int_0^z dz' \frac{1}{H_0 E(z')} \\ &= \frac{z}{H_0} + ... = \frac{D_L}{c} + ... \end{aligned} \tag{1.61}$$

1.4 GW170817

The GW event GW170817 was detected by Advanced LIGO and Virgo on 17th August 2017 [1] at 12:41:04.4 UTC and it is consistent with the merger of a BNS. Following the GW event, a series of EM signals were detected. The detection of GW and EM counterparts is depicted in Fig. 1.5. After just (1.74 ± 0.05) s from the GW luminosity peak, a short gamma-ray burst, GRB 170817A, was identified by both the Fermi Gamma-ray Burst Monitor and the Anti-Coincidence Shield of the Spectrometer of the International Gamma-Ray Astrophysics Laboratory (INTEGRAL) [36].
The probability of the near-simultaneous spatial and temporal occurrence of these phenomena happening by pure chance was proved to be 5.0×10^{-8} [7], reinforcing the hypothesis of BNS mergers as precursors to sGRBs.
Subsequently, a Kilonova was observed spanning from X-rays (9 days after the merger) to radio (16.4 days after the merger).

1.4.1 LIGO–Virgo Observation of GW170817

GW170817 marks the first GW observation from a BNS coalescence [35]. The event was initially observed as a single-detector trigger in the LIGO-Hanford. Automated comparison of the single-detector trigger with the Fermi-GBM Gamma-ray Coordinates Network notice immediately enabled the identification of the temporal proximity of GRB170817A with GW170817.
The combined observations from aLIGO and AdV allowed for a highly accurate sky position localization to an area of $28\,\mathrm{deg}^2$ with a 90% confidence level (green area in Fig. 1.6). A time-frequency representation of the LIGO data containing GW170817 is shown in the upper panel of Fig. 1.5. The GPS time of the GW170817 merger was measured to be $T_0^{\text{GW}} = 1187008882.43$.
In terms of mass components, assuming dimensionless spins with magnitude up to

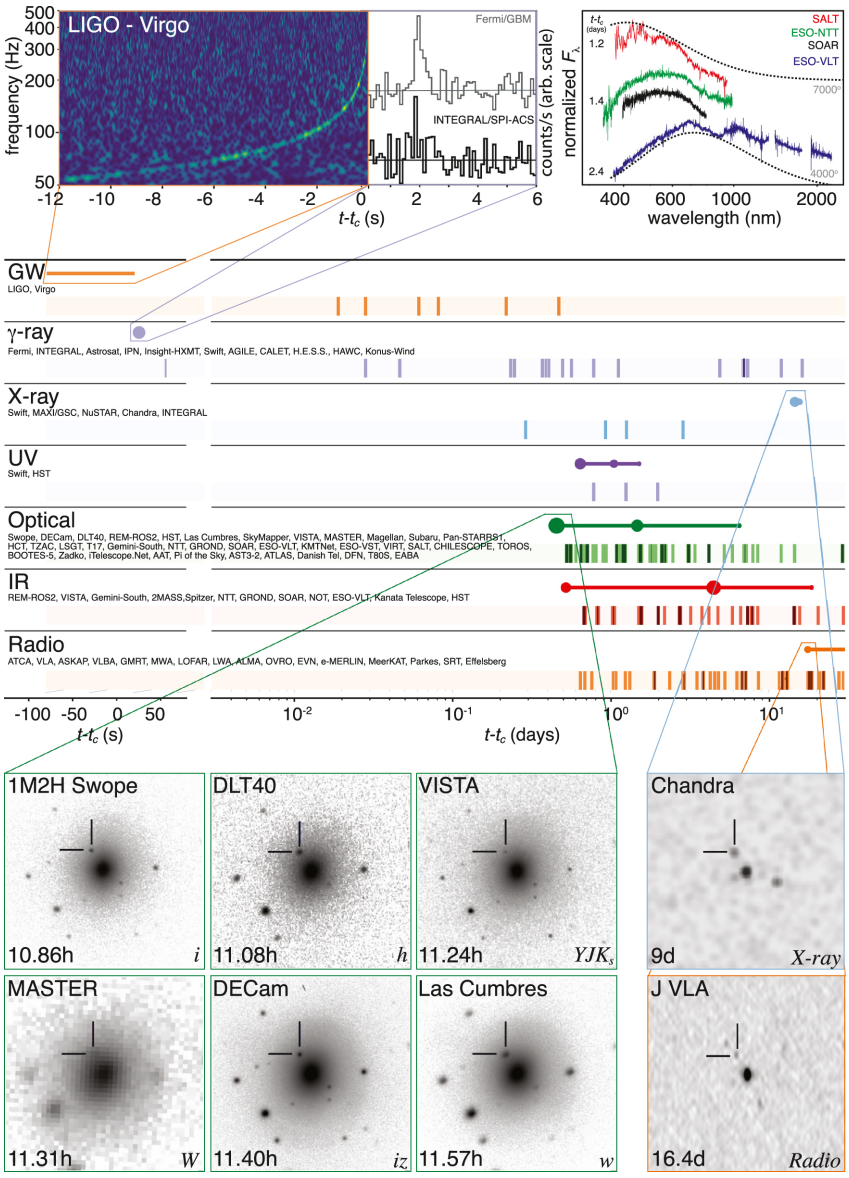

Figure 1.5. Timeline of the discovery of GW170817, GRB 170817A, SSS17a/AT 2017gfo (optical detection), and the follow-up observations are shown on each row by messenger and wavelength relative to the time t_c of the gravitational-wave event. The names of the relevant instruments, facilities, or observing teams are collected at the beginning of the row. Pictures are shown of the first detections in the GW, γ-ray, optical, X-ray, and radio bands. Figure adapted from [35].

0.89, the 90% credible intervals are $m_1 \in (1.36, 2.26)\, M_\odot$ and $m_2 \in (0.86, 1.36)\, M_\odot$ with a total mass of $2.82^{+0.47}_{-0.09}\, M_\odot$. If the dimensionless spin is limited at magnitude 0.05, then the masses intervals become $m_1 \in (1.36, 1.60)\, M_\odot$, $m_2 \in (1.17, 1.36)\, M_\odot$, and the total mass is $2.74^{+0.01}_{-0.01}\, M_\odot$. These findings align well with all currently known binary neutron star systems [37, 38].

The event distance, solely derived from the gravitational wave data, is reported to be 40^{+8}_{-14} Mpc, making GW170817 the closest gravitational wave event ever recorded [1].

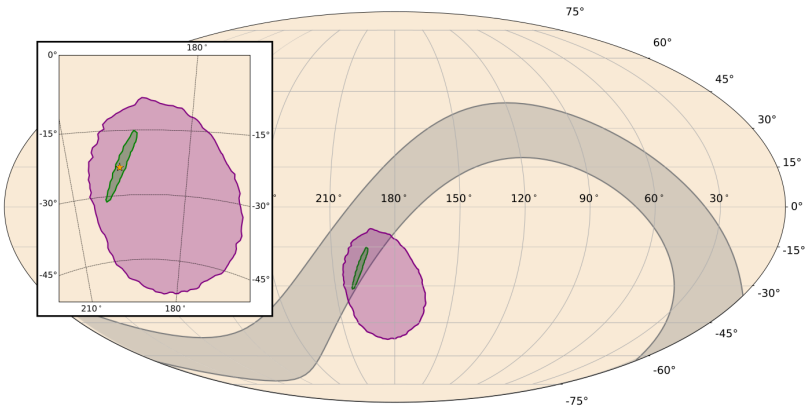

Figure 1.6. Final localizations [7]. The 90% contour for the final sky-localization map from LIGO–Virgo is shown in green. The 90% GBM targeted search localization is overlaid in purple. The 90% area determined with Fermi and INTEGRAL timing information is shaded in gray. The zoomed image also shows the position of the optical transient marked as a yellow star. The axes are right ascension and declination in the Equatorial coordinate system

The GW data restrict the inclination angle ι, the angle between the total angular momentum of the system and the line of sight, to be anti-aligned, with $\cos\iota \leq -0.54$ [1].

1.4.2 Speed of Gravity

It is possible to constrain the speed of gravity by using Eq. 1.59. From Eq. 1.61, we find that in the local universe, i.e $z \ll 1$, the lookback time T_l can be written as a function of the luminosity distance D_L:

$$\mathrm{T}_l \approx \frac{D_L}{c} \tag{1.62}$$

By using this relation and Eq. 1.59 we can write:

$$\hat{\alpha}_0 = 2c\frac{\Delta t_d - \Delta t_s}{D_L} \tag{1.63}$$

where Δt_s and Δt_s are the GW-GRB time delay at the detector and source respectively.
We remind the reader that:

$$\hat{\alpha}_0 = 2\frac{\mathrm{v_{GW}} - \mathrm{v_{EM}}}{\mathrm{v_{EM}}} \tag{1.64}$$

with $\mathrm{v_{GW}}$ GW's group velocity and $\mathrm{v_{EM}} = c$ speed of light.
Eq. 1.63 is less constraining for smaller distances, therefore, as done in [7], we conservatively use the lower bound on the luminosity distance measurement $D_L = 26$ Mpc [1].
Assuming conservatively that the GW luminosity peak (merger) and the sGRB were emitted at the same time (attributing the entirety of the (1.74 ± 0.05) s time delay to a faster GW signal) gives us an upper bound on α_0.

To set a lower bound on $\hat{\alpha}_0$, we assume a prompt time delay Δt_s of +10 s, namely the GRB is prompted 10 seconds before the GW. This is a deliberate choice in [7] and motivated by the uncertainties we currently have on GRB prompt emission. These assumptions led to the following constraints [7]:

$$-3 \times 10^{-15} \leq \frac{\Delta \mathrm{v}}{\mathrm{v}_{EM}} \leq +7 \times 10^{-16} \tag{1.65}$$

The impact of the intergalactic medium dispersion on the gamma-ray photon speed is negligibly small, with an expected propagation delay many orders of magnitude smaller than these constraints on v_{GW}.

1.4.3 Hubble Constant

The multi-messenger observation (encompassing GWs, sGRBs, and optical transients) of GW170817 allowed us to identify its host galaxy: NGC4993 in the Hydra constellation [7]. From the host galaxy, it is possible to measure the redshift of the GW event ($z = 0.009727$).
Given a measure of the BNS luminosity distance (derived solely from the GW signal) and the redshift (inferred from the galaxy), it is possible to measure the cosmology. This method bypasses the need for any cosmic "distance ladder" [39], enabling GW analysis to directly measure the luminosity distance, without intermediate astronomical distance measurements.
To method used to constrain H_0 from the multi-messenger observation of GW170817 is the following: at nearby distances (≤ 50 Mpc) H_0 is well approximated by the expression $D_L = \frac{c\,z}{H_0}$ (see Eq. 1.14).
Then, having determined the luminosity distance and redshift from the GW and EM data, the Hubble constant H_0 was found to be $70.0^{+12.0}_{-8.0}\ \frac{\mathrm{km}}{s\ \mathrm{Mpc}}$ (68% credible interval) [2]. This estimate, derived by using Bayesian analysis, aligns with other measurements of this quantity, such as CMB measurements from Planck and Type Ia supernova measurements from SH0ES (see Section 1.1.1).
Comparing this result with the previous measurements suggests that, despite the potential influence of varying systematic uncertainties on each method, we do not currently observe any systematic difference between GW and established EM-based estimates.

1.5 Summary and Goal of this thesis

As we have seen in the previous Sections, multi-messenger observations of BNS mergers offer a great opportunity for testing the speed of gravity and cosmology.
To test the speed of gravity we just need the joint observation of a GW and GRB. The speed of gravity can be constrained with the distance inferred from the GW and the detected time delay (provided a prompt time delay model).
For the cosmology, we need the additional measure of the galaxy host redshift. This thesis has two objectives:

- As shown in Section 1.4.2, the joint observation of GW170817 and GRB170817A was used to constrain the speed of gravity by applying conservative fixed bounds

for the prompt time delay Δt_s distribution. Thus, the first objective of this work is to check if future observations will allow us to jointly infer the speed of gravity and prompt time delay distribution using joint observations of time delay and luminosity distances from BNS.

- The second objective is to develop a new technique to constrain H_0 in the absence of a direct redshift z measurement. To understand how, consider the Equation for the time delay between GW and GRB at low redshifts:

$$\Delta t_d^{\text{GW-GRB}} = (1 + z_s)\Delta t_s^{\text{GW-GRB}} + \frac{\hat{\alpha}_0}{2}\frac{D_L}{c} \tag{1.66}$$

From a single joint observation of GW-sGRB, we can measure both D_L and Δt_d. If the value of Δt_s is known and $\hat{\alpha}_0 = 0$, then it is possible to obtain an implicit redshift evaluation to use for cosmology.
Of course, we do not know the distribution of Δt_s and we will fit for it. This method is inspired by the source frame mass method that uses the same idea but applies it to the chirp mass $\mathcal{M}_{\text{obs}} = \mathcal{M} \times (1 + z)$ [40].

Chapter 2

Principles of detections for GWs and sGRBs

In this Chapter, I will introduce the detection processes for GWs and GRBs. This introduction is necessary to understand the next Chapter, where I will describe how I performed the simulations for this thesis.
I will begin the Chapter by describing how to detect GWs, and current and future GWs detectors (LIGO, Virgo, Einstein Telescope) [41, 42, 43], in Section 2.1. Then, in Section 2.2, I will describe the γ-ray detector Fermi-GBM [44]. Finally, in Section 2.3 I will report on the latest studies for future prospects of EM-GW detectors [3].

2.1 GWs detection

Gravitational waves induce changes in the proper distance between objects, while the objects themselves remain at rest locally. In GR, the changes exhibit an opposing sign for orthogonal directions, as shown in Fig. 2.1. The effect can be measured as a

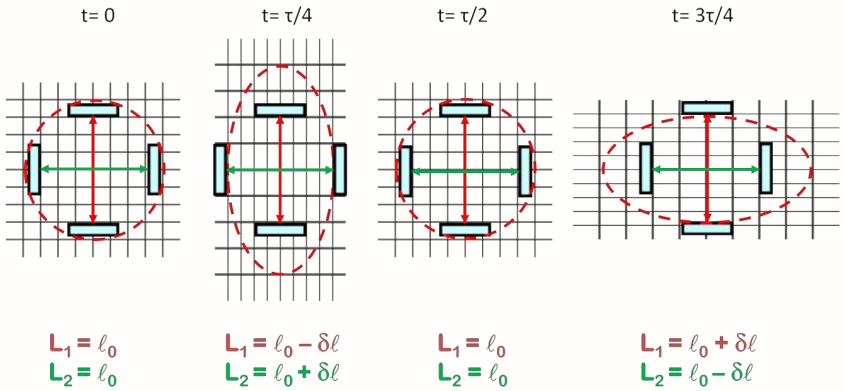

Figure 2.1. The effect of gravitational waves on the distances between objects [45]. While the mirrors remain locally at rest the metric gets changed by the gravitational wave. The figure shows the effect of a sinusoidal gravitational wave with period τ, for different times t. The distances measured between the mirrors change by $\pm\delta L$.

relative length change $\delta L/L$ and it is generally smaller than 10^{-22}.

GW detectors are based on the concept of a Michelson interferometer as depicted in Fig. 2.2. A laser beam is split into two beams that traverse the interferometer arms.

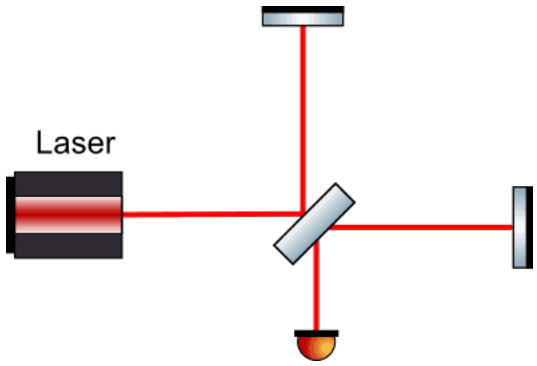

Figure 2.2. Michelson interferometer principle for gravitational wave detection.

Since the GW is changing the arms' length, the two beams of light will take a slightly different time to travel along the arms and recombine at the beam splitter. Given the two different travel times, the recombined beam will show an interferometric pattern that can be detected on the photodetector at the output.
Despite the straightforwardness of the measurement principle, achieving optimal sensitivity necessitates the minimization of all influences that could alter the geometrical or optical arm length, or generate a signal that mimics a gravitational wave in the detected photo-current. As a result, these instruments are extremely sophisticated and complex.
The basis for current and next-generation GW detectors is a dual recycled Fabry-Perot arm cavity Michelson interferometer. Given that a Michelson interferometer with a kilometer-scale arm length fails to provide the sensitivity required for GW detection, modern GW observatories integrate multiple optical cavities with a Michelson interferometer to enhance sensitivity. Consequently, two Fabry-Pérot optical cavities are incorporated into the arms, which consist of input mirrors and end mirrors, effectively extending the interferometer's arm length. For instance, in KAGRA (see Section 2.1.3 for more details), the arm cavities augment the effective arm length by a factor of approximately 1000, resulting in a GW sensitivity improvement by the same factor.

2.1.1 Signal-to-Noise Ratio

A metric for the detection of GW signals is the Signal-to-Noise Ratio (SNR) [41]. The SNR measures the signal strength with respect to the detector's noise fluctuations. These fluctuations can be described by the power spectral density $S_n(|f|)$, where f is the frequency. The power spectral density quantifies the noise fluctuations with respect to the frequency, i.e. $S_n(|f|) = \langle|\tilde{n}(f)|^2\rangle$, where $\tilde{n}(f)$ is the Fourier transform of the noise signal and $\langle\cdot\rangle$ denotes the average over noise realizations.
The amount of detector noise determines the strength of the weakest detectable signals and thus, the maximum distance at which a BNS can be observed.
Let $h(t)$ be the detector response to a gravitational radiation signal from any source. For a detector noise with power spectral density $S_n(|f|)$ the SNR squared ρ^2 is

defined to be:

$$\rho^2 = 4 \, \mathrm{Re} \left[\int_0^\infty \frac{\tilde{h}(f)\tilde{h}^*(f)}{S_n(|f|)} df \right] \tag{2.1}$$

where $\tilde{h}$ is the Fourier transform of the detector response and $\tilde{h}^*$ is its complex conjugate. If ρ is sufficiently large then one can assert with high confidence that a GW has been detected. Typically, when we get an SNR of $\rho \geq 4.9$ in each detector for a three-detector network, a GW has been detected with confidence greater than 99%[46].
In general, the combined signal-to-noise ratio ρ for a network of detectors is defined as

$$\rho \equiv \sqrt{\sum_a \rho_a^2} \tag{2.2}$$

where ρ_a is the SNR in the a^{th} detector.

2.1.2 Antenna Patterns

A single interferometric gravitational-wave detector cannot measure both polarizations of GW, but only a linear combination of the two given by:

$$h(t) = F_+(t, \theta, \phi, \psi) h_+(t) + F_\times(t, \theta, \phi, \psi) h_\times(t) \tag{2.3}$$

F_+ and $F_\times$ are the antenna pattern response functions of the interferometers to the two polarizations of the wave h_+ and $h_\times$ [47]. They describe the relative sensitivity of the detectors in different directions, and they are functions of the time t, the source sky location (θ, ϕ), and the polarization angle ψ. These functions reach the maximum value of 1 when the polarization of the GW aligns perfectly with the detector arms.
By defining an overall antenna pattern F, Eq. 2.3 can be written as:

$$h(t) = F(\cos\xi \; h_+(t) + \sin\xi \; h_\times(t)), \quad F = \sqrt{F_+^2 + F_\times^2}, \quad \tan\xi = \frac{F_\times}{F_+} \tag{2.4}$$

It can be shown that F is independent of the polarization angle $F = F(t, \theta, \phi)$ and it thus measures the sensitivity of the detector with respect to different sky locations. Fig. 2.3 plots F for an L-shaped interferometer such as Virgo (panel on the left) and for a triangular ET (panel on the right).

2.1.3 2nd Generation GWs Detectors

The Advanced LIGO (aLIGO) [48] and Advanced Virgo (AdV) [49] detectors operate as enhanced "L" shaped Michelson interferometers, having arm lengths of 4 km and 3 km respectively. The former comprises two detectors situated in Hanford, WA, and Livingston, LA while the latter is situated in Cascina, close to Pisa, Italy. Fig. 2.4 shows a photograph of the Advanced Virgo detector.
The GEO 600 detector [50], a British-German interferometric GW detector (with lower sensitivity than aLIGO and AdV), is equipped with 600 m arms and located near Hannover, Germany. KAGRA is an underground laser interferometer with 3-km arms, situated in the Kamioka Observatory, Gifu Prefecture, Japan. A crucial

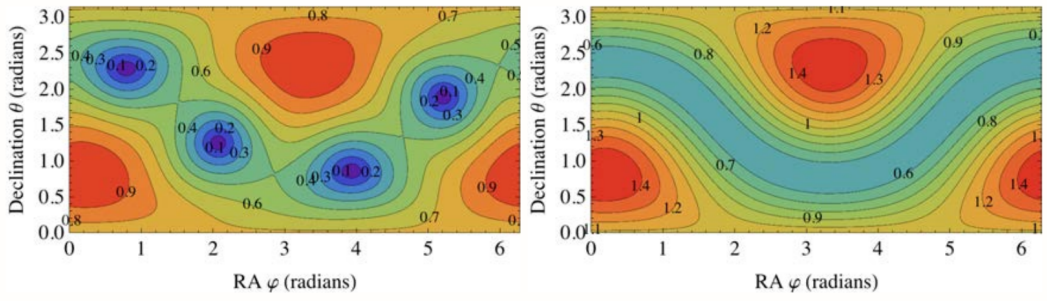

Figure 2.3. Antenna pattern of ET (right panel) compared to that of Virgo (left panel) [45]. ET is assumed to be at the same location as Virgo. Note that Virgo is a single L-shaped detector while ET consists of three V-shaped interferometers rotated relative to one other by 120 deg.

Figure 2.4. Aerial view of Advanced Virgo. The "L" shape of the detector is clearly visible here.

feature of KAGRA is its cooling system, designed to maintain the large mirrors of the interferometer at cryogenic temperature (approximately 20 K) to mitigate thermal noise [51].

In 2011, proposals for the installation of one of the Advanced LIGO Hanford detectors at a new observatory in India were presented by the LIGO Lab and the IndIGO5 consortium [52]. In 2015, this interferometer was put into long-term storage in preparation for its intended use in India. The Indian government approved the LIGO-India project in February 2016. The planned operation for this detector, identical to the configuration of the other LIGO instruments including any upgrades, is anticipated to commence in 2025. The current scheduled plan for the advanced GW detectors is depicted in Fig.2.5. Below we highlight the past, current, and future observing runs for 2nd generation detectors.

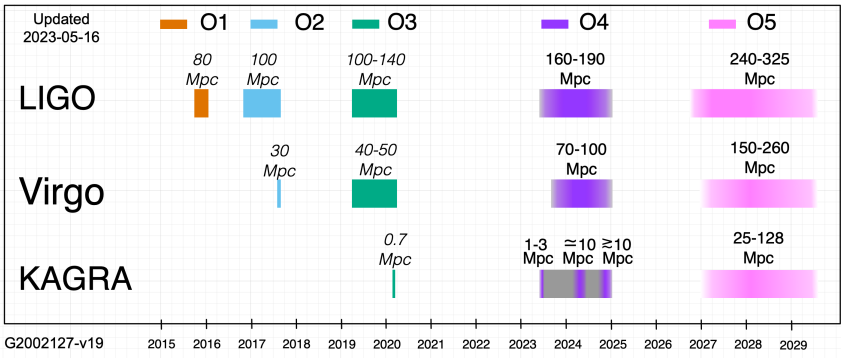

Figure 2.5. The planned sensitivity evolution and observing runs of the aLIGO, AdV, and KAGRA detectors over the coming years. The colored bars show the observing runs, with achieved sensitivities in O1, O2, and O3, and the expected sensitivities given by the data in Fig. 2.6 for future runs. Uncertainty in start or finish dates is represented by shading.

1. **O1**: The first observing run (O1) began on September 18, 2015, and concluded on January 12, 2016, with engineering period data of sufficient quality to be incorporated into the analysis. This implies observational data was collected from September 12, 2015, to January 19, 2016. The two detectors involved in this run were Hanford (H) and Livingston (L), achieving an 80 Mpc BNS range. During this run, 3 Binary Black Hole (BBH) mergers were detected.

2. **O2**: Subsequently, the second observing run (O2) began on November 30, 2016, and terminated on August 25, 2017. It was preceded by an engineering run which began on 31 October 2016 at Livingston and on 14 November 2016 at Hanford. The delay at Hanford was to facilitate extra commissioning activities. The achieved sensitivity was a BNS range of typically 80-100 Mpc. The AdVirgo interferometer [49] joined O2 on August 1, 2017, hence, forming the three-detector network LIGO-Hanford, LIGO-Livingston, and Virgo (HLV) for the concluding month of the run. AdV reached a BNS range of 30 Mpc. GW170817, the first detection of a BNS merger, was localized to a 90% credible region of 16 deg^2. The enhanced accuracy is due to the addition of AdV to the network. During this run, 10 BBHs were detected.

3. **O3**: The third observing run, extending from April 1, 2019, to April 21, 2020, primarily collected data from the three-detector network (HLV) of aLIGO and AdVirgo. It comprised two main operational phases: O3a (April 1, 2019, to October 1, 2019), and O3b (November 1, 2019, to March 27, 2020), with a month-long maintenance break in between. Initially, KAGRA was expected to join O3 but this plan was altered due to the COVID-19 outbreak. Instead, KAGRA and GEO 600 operated during an extended observing phase, O3GK, from April 7 to April 21, 2020. The median values of the BNS range over the entire observing run were 108 Mpc, 135 Mpc, and 45 Mpc for Hanford, Livingston, and Virgo respectively during O3a, and 115 Mpc, 133 Mpc, and 51 Mpc during O3b for the same detectors. The median values of the BNS range

over the O3GK period were 0.66 Mpc for KAGRA and 1.06 Mpc for GEO 600. During this run 90 compact binaries were detected.

Future observing runs are anticipated to involve the upgraded aLIGO and AdV detectors, referred to as A+ and AdV+ respectively. Such upgrades will enhance LIGO and Virgo's range compared to the aLIGO and AdV detector design sensitivities. In Fig 2.6 we show the expected sensitivities for current and future observational runs. These sensitivities will be used for this study.

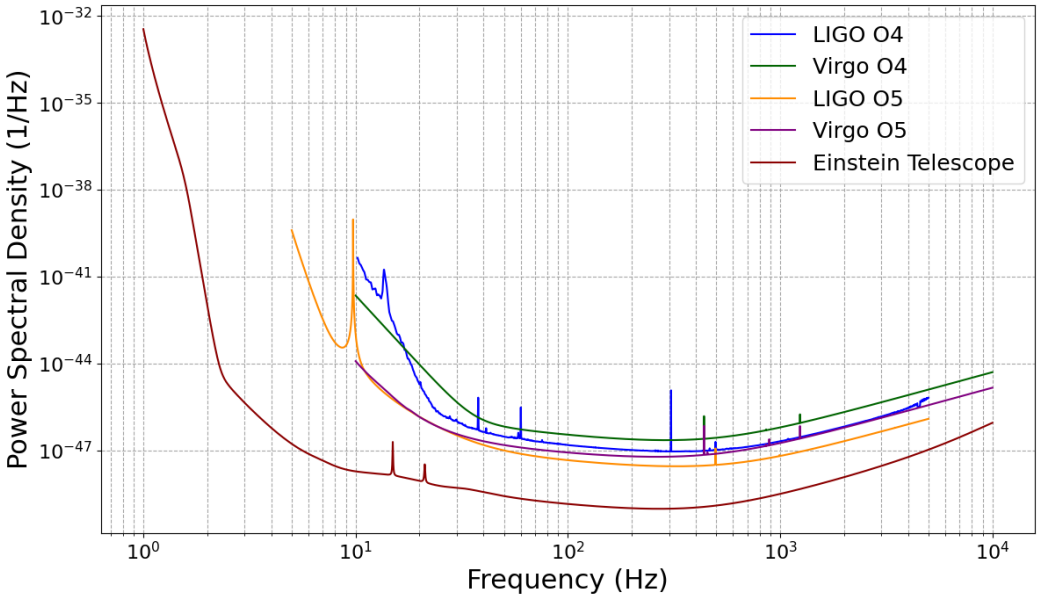

Figure 2.6. Power Spectral Density (PSD) as a function of frequency for current (O4) and future observational runs (O5, ET).

1. **O4**: The fourth observing run (O4) began on May 24, 2023. The observing run will last 20 calendar months including up to 2 months of commissioning breaks for maintenance. It will involve a four-detector network with the two aLIGO instruments at 160-190 Mpc; Phase 1 of AdV+ at 70-100 Mpc. In the last months of the observational run, KAGRA is expected to reach a sensitivity $\geq$ 10Mpc.

2. **O5**: The fifth observing run (O5) is planned to start in late 2026 or early 2027, and extend till 2030. O5 will incorporate the A+ upgrade for the aLIGO instruments and the AdV+ Phase 2 upgrade for Virgo. With the addition of an upgraded aLIGO interferometer in India by 2025, a five-detector network is expected to be operational. The target range for aLIGO is 240-325 Mpc and for AdV it is 150-260 Mpc. KAGRA is expected to operate at a sensitivity range of 25-128 Mpc.

2.1.4 Einstein Telescope

The Einstein Telescope (ET) is a proposed third-generation ground-based GW detector in Europe [43, 45]. It represents an advancement from second-generation

detectors like aLIGO, AdV, and KAGRA. It is predicted that ET will begin operation around the mid-2030s. The sensitivity of ET, compared to its predecessors, is anticipated to increase by an order of magnitude across the detection frequency band that is currently available to ground-based detectors, varying between 10 Hz to a few kHz. Moreover, ET will give access to the low-frequency band in the region $\sim 2 - 10$ Hz.
For frequent and precise observations of low-frequency sources, an extension of the detection range towards lower frequencies is also required. To achieve the desired sensitivity, ET will need to harness all state-of-the-art technologies, pushing them to their technical limits.
To achieve the sensitivity goal the detector's size must be increased beyond the 3 km (for Virgo) and 4 km (for LIGO) size of current devices. It also requires positioning the detector underground where the seismic noise is far less than on the surface. Only by increasing the arm length to 10 km can the influence of unavoidable displacement noises be lowered to a tolerable level.
In its final configuration, the ET will comprise of three nested detectors arranged in a triangular shape with the angles between the arms being 60°, thus differing from the traditional L-shaped geometry of earlier detectors. Fig. 2.7 shows a schematic view of the ET Observatory. This layout is uniformly sensitive to both polarisations

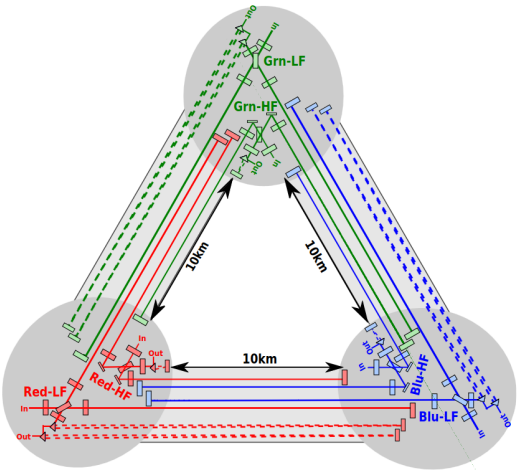

Figure 2.7. Schematic full view of the optical layout of the ET Observatory [53] It consists of 3 pairs of km-scale interferometers positioned such that they form a triangular shape. Each interferometer pair represents one wide-band detector, in which one interferometer is optimized for gravitational waves at low frequencies and the other for high frequencies.

of the GW and shows a more isotropic antenna pattern, as shown in Fig. 2.3. The overall frequency range will span from 3 Hz to several kHz. Each detector will contain two interferometers - one optimized for detecting low-frequency gravitational waves (i.e., < 100 Hz) and the other for the high-frequency range (i.e., > 100 Hz). Every interferometer will possess a classical dual-recycled Michelson topology with Fabry-Perot arm cavities. Figure 2.6 shows the sensitivity curve for ET.
The resulting sensitivity in comparison to a single 90° detector (such as aLIGO and

AdV) depends on the source location in the sky and its orientation, as the angular antenna pattern (see Fig. 2.3) and the polarization dependence (independent in the triangular case) influence the signal strength differently.
On average the sensitivity of the triple 60° detector is slightly better than a single, optimally oriented 90° one.

2.2 The Fermi Gamma-ray Burst Telescope

Here we briefly describe the Fermi Gamma-ray Burst Monitor [44] which is the instrument with which we model our simulation studies.
On 11 June 2008, a Delta II heavy rocket transported the Gamma-ray Large Area Space Telescope into orbit. By August of the same year, both the Gamma-ray Burst Monitor (GBM) and the Large Area Telescope (LAT) were fully operational. The satellite was then renamed the Fermi Gamma-ray Burst Space Telescope (FERMI), in tribute to Enrico Fermi's groundbreaking work in high-energy astrophysics.
Fig. 2.8 shows the FERMI observatory configuration while Fig. 2.9 shows the actual observatory before lunch. More than 13 years later, the observatory remains

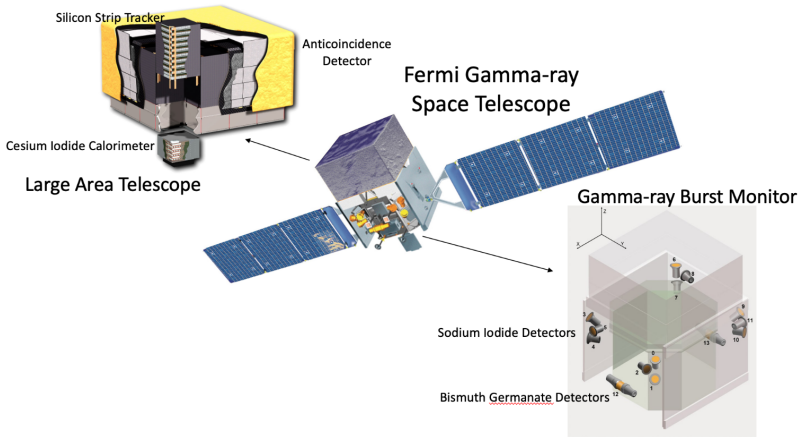

--

Figure 2.8. Overview of Fermi Gamma-ray Burst Space Telescope and its scientific instruments [54].

operational, with the instrument performance exceeding its initial state. Fermi's instruments observe γ rays from sources as close as Earth's atmosphere to as distant as high-redshift GRBs.
The Fermi Large Area Telescope (LAT) detects γ rays that interact by pair production in the field of an atomic nucleus, using measurements of the electron-positron pair to derive arrival time, arrival direction, and energy for individual photons [55].
For this work, however, we will focus on the Gamma-ray Burst Monitor.

2.2.1 Gamma-ray Burst Monitor

The GBM detects hard X-rays and γ rays as they interact with scintillation crystals [54]. The γ-rays produce light in the scintillation crystal which is then detected with

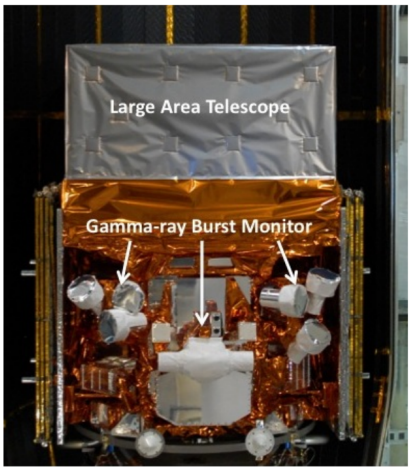

Figure 2.9. Photo of Fermi Gamma-ray Space Telescope atop the rocket before launch.

an attached photomultiplier tube. The number of photons produced in the crystal is proportional to the energy of the γ ray.
GBM comprises two types of detectors: twelve Thallium activated Sodium Iodide detectors (NaI(Tl)), oriented in groups of three on the corners of the spacecraft, and two Bismuth Germanate (BGO) detectors, one on each side of the spacecraft. This arrangement allows GBM to detect GRBs in any part of the sky not blocked by the Earth that roughly corresponds to a field of view of 500 deg^2
The NaI(Tl) detectors consist of a cylindrical crystal with a 12.7 cm diameter and 1.27 cm thickness coupled with a 12.7 cm diameter photomultiplier tube (PMT). A Beryllium entrance window enables these detectors to be sensitive to energies from 8 keV to 1 MeV.
The BGO detectors each consist of a cylindrical crystal with a 12.7 cm diameter and length. A PMT is coupled to each end of the BGO crystal, providing better light collection than a single PMT. The BGO detectors have an energy range from 200 keV to about 40 MeV, bridging the energy ranges of the GBM NaI detectors and the Fermi Large Area Telescope (Energy range:20 MeV – >300 GeV). Fig. 2.10 and 2.11 show the two detectors.
In the 10-1000 keV energy band (this range matches the one chosen in the Fermi Gamma-ray Burst catalogs [56]), the GBM has a flux threshold of $\sim 0.5\ \frac{\mathrm{ph}}{\mathrm{s\ cm^2}}$.
Signals from each GBM detector are processed by the digital processing unit and digitized into 4096 linear energy channels. If the signal exceeds a programmable threshold, the peak height of the pulse is measured and converted into energy channel and 8 energy channel data types. The primary data from GBM are packaged into two types, continuous data, and trigger data, as Flexible Image Transport System files at the GBM Instrument Operations Center in Huntsville, Alabama.

2.3 Multi-messanger prospects for ET

BNS events with detected sGRBs and unidentified host galaxies will be commonly observed in the ET era. ET is designed to detect BNS coalescences up to $z \approx 5$ with

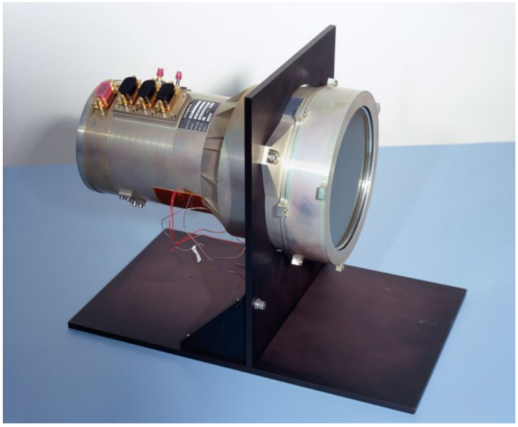

Figure 2.10. Fermi GBM NaI Detector [54].

Figure 2.11. Fermi GBM BGO Detector [54].

an estimated rate of 6×10^4 events annually. The detection range reaches the peak of the star formation rate, thereby covering the vast majority of BNS coalescing in the universe. This will enable the exploration of their formation mechanisms, evolution, and population rate. Fig. 2.12 shows the expected redshift distribution of GW detections by ET. Moreover, the high-frequency sensitivity of ET will grant access to the gravitational wave signal of the merger phase that is inaccessible to second-generation detectors, providing detailed insights into the internal structure of neutron stars and their equation of state.
When considering ET+Fermi-GBM, it was predicted that 68^{+13}_{-18}% of all the sGRBs with a detectable prompt emission will also have a detectable GW counterpart [3]. For this configuration, we thus expect 33^{+14}_{-11} joint GW-SGRB detections per year.
In general, the γ-ray missions that are more suited to maximize the joint detection rates are those with a large field of view and best sensitivity around MeV energies (as is the case for FERMI-GBM). However, another parameter to take into account is the localization accuracy by the EM detectors, which defines what are the instruments that are able to drive the follow-up observations by ground-based telescopes, which is crucial for obtaining the source redshift.
For this reason, instruments such as X/Gamma-ray Imaging Spectrometer on board

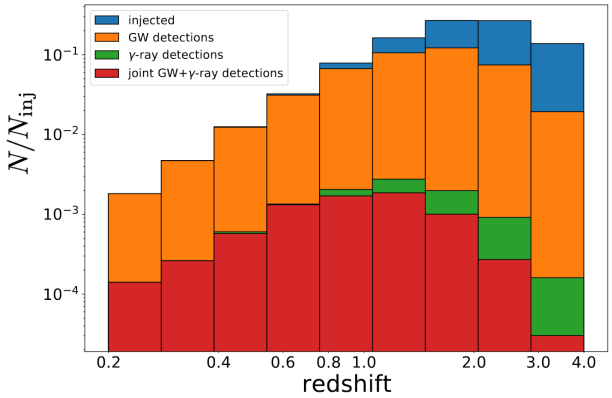

Figure 2.12. Histogram of the joint ET+Fermi-GBM detections (red), together with the distribution of injected BNS (blue), the mergers detected by ET (orange), the mergers detected by Fermi-GBM (green). The histogram is normalized to $N_{\rm inj} = 10^5$, which is the number of injected BNS mergers in the viewing angle range $0° < \theta_{\rm view} < 15°$ and in the redshift range $0 < z < 4$. Figure adapted from [3]

the Transient High-Energy Sky and Early Universe Surveyor (THESEUS) [57, 58] (up to now it is just a mission concept), with a proposed localization accuracy < 15 arcmin, will play a crucial role in the observation of γ-ray and X-ray counterparts, by detecting per year between 10^{+5}_{-4} well-localized SGRBs (with detectable GW counterpart) up to high redshifts, for which also the host galaxy can be identified [3].

Chapter 3

Generation of the GW-sGRB Mock catalog

In this chapter, I will describe the procedure we followed to generate a mock catalog of joint GW-sGRB observation (see Fig.3.1). I will begin by describing the simulation

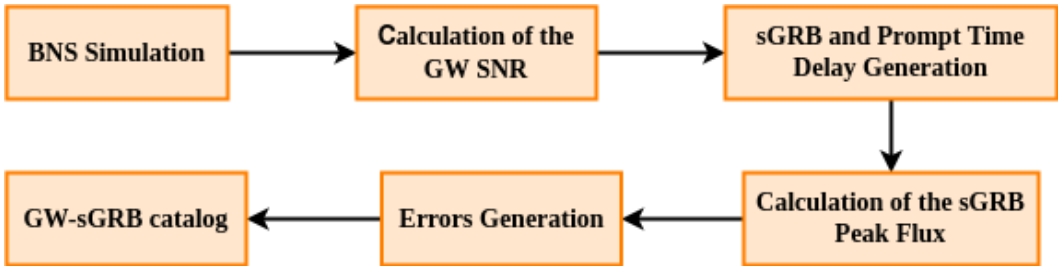

Figure 3.1. Scheme of the procedure followed to generate the GW-sGRB mock catalog.

of a BNS population in Section 3.1. Moving on, in Section 3.1.1 I will discuss the model for the detection of the GW signal [59]. In Section 3.2, I will treat the problem of generating both sGRB signal and GW-sGRB time delays in the source frame [60, 61]. In Section 3.3, I will focus on the detection of sGRB [62]. Finally, in Section 3.4, I will briefly describe the simulated catalog.
For generating the mock catalog, we chose a flat ΛCDM cosmology whose parameters match those derived from the final full-mission Planck measurements of the CMB anisotropies [63] ($H0 = 67.66 \frac{\text{km}}{\text{s Mpc}}$,$\Omega_m = 0.315$), and we assumed the speed of gravity to be equal to c ($\hat{\alpha}_0 = 0$).

3.1 BNS simulation

The first step of this study was to simulate a BNS population. This was achieved by developing a Python code capable of drawing BNS parameters relevant to GW and GRB emission. The parameters of interest are: right ascension α, declination δ, the orbital inclination angle ι, the polarization angle ψ, the single component masses and spins m_1, m_2, χ_1, χ_2 and the merger redshift z. In the following, I list which population models have been employed to draw BNS parameters.

1. The celestial coordinates, right ascension α and declination δ, are sampled from an isotropic distribution in the sky since we expect BNS mergers to equally happen in all directions. The right ascension α is uniformly distributed in the interval $[0, 2\pi]$, while $\cos\delta$ is uniformly distributed in $[-1, 1]$ (this corresponds to $p(\delta) \propto \sin\delta$).

2. The cosine of the inclination angle ι (angle between the BNS total angular momentum and the line of sight) is uniformly sampled in the interval $[-1; 1]$. This corresponds to an isotropic distribution of the inclination angle with respect to our line of sight.

3. The polarization angle ψ (angle between the direction of h_+ and some reference direction) of the GW signal is uniformly sampled from the interval $[0, 2\pi)$.

4. The single component masses m_1 and m_2 are uniformly distributed in the interval $(1, 3)M_\odot$, with the condition $m_2 < m_1$. This assumption is consistent with the last rate models inferred from the LVK detections during O3 [64].

5. We assumed all NSs to be spinless $\chi_1 = \chi_2 = 0$. This is consistent with the expectations from BNS since they are low-spinning objects.

6. The BNS merger rate as a function of redshift has not yet been measured. Typically we parametrize the rate as:

$$\frac{dN}{dz dt_s} = \frac{dN}{dV_c dt_s} \frac{dV_c}{dz} \tag{3.1}$$

where t_s is the source-frame time and V_c is the comoving volume, i.e. a volume measurement in comoving coordinates. In this work, we assume that the evolution of the merger rate $\frac{dN}{dV_c dt_s}$ is perfectly known to follow the Madau-Dickenson star formation rate (SFR) [65]:

$$\Phi(z) = \frac{R(z)}{R_0} = [1 + (1 + z_p)^{-\gamma-k}] \frac{(1+z)^\gamma}{1 + \left(\frac{1+z}{1+z_p}\right)^{\gamma+k}} \tag{3.2}$$

where the model parameters (γ, k, z_p) are set to (2.7, 6.0, 2.0) respectively, while R_0 is the BNS merger rate per $\mathrm{Gpc}^{-3}\ \mathrm{yr}^{-1}$ today. The parameters chosen are in agreement with the Binary Black Hole (BBH) merger rate inferred from O3. The BBH rate has been measured and found to be proportional to $\frac{R(z)}{R_0} \propto (1+z)^{2.7}$ [64]. The redshift dependence of the Madau-SFR is depicted in Fig. 3.2. At low redshifts, the rate increases as $(1+z)^\gamma$. It then reaches a peak around $z = z_p$ and it then decreases as $(1+z)^{-k}$. The Python code is able to generate BNS mergers up to a maximum, user-defined, redshift value $z_{\max}$. Depending on the detector network configuration (see Section 3.1.1), we chose $z_{\max} = 0.1$ for O4, 0.2 for O5, and 2 for ET, ensuring the redshift range is deep enough to capture all detectable events.
In Eq 3.1, the comoving volume $V_c(z)$ as a function of redshift is given by:

$$V_c(z) = \int_0^z d\Omega dz' \frac{dV_c}{dz' d\Omega}, \tag{3.3}$$

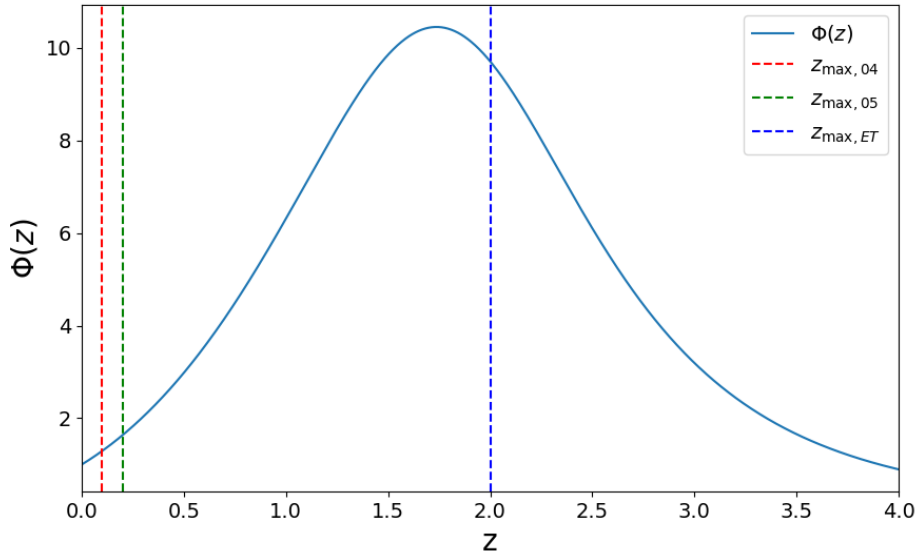

Figure 3.2. Madau-Dickinson rate $\Phi(z) = \frac{R(z)}{R_0}$ and values of $z_{\max}$ for each detection sensitivity. The vertical dashed lines are the maximum redshift measurements $z_{\max}$ used for this simulation. Their values differ with respect to the detector network configuration: O4, O5, or ET.

where:

$$\frac{dV_c(z)}{dz d\Omega} = \frac{c^3}{H_0^3} \frac{1}{E(z)} \left[\int_0^z \frac{dz'}{E(z')} \right]^2 . \tag{3.4}$$

We calculate the differential of the comoving volume with `astropy` [66].

In Table 3.1 we report the BNS parameters with their distribution.

Table 3.1. List of BNS population parameters with their distribution model and range as described in Section 3.1

Parameter	Distribution Model	Distribution range
α	Uniform	[0,π)
$\cos\delta$	Uniform	[-1,1]
$\cos\iota$	Uniform	[-1,1)
ψ	Uniform	[0,2π)
m_1, m_2	Uniform	$(1,3)M_\odot$
χ_1, χ_2	Fixed to 0	
z	Madau	[0,z_{max})

.

3.1.1 GW Detection

To assess the GW detection we use a SNR criterion. If the observed network SNR is greater than 12 we assume the signal to be detected. This is a conservative threshold for the detection of GW events.

The first step to calculate the optimal GW SNR is to calculate the luminosity distance. With this quantity and the other binary parameters of the previous Section, we can adopt a simplified model to compute the optimal SNR. We use the 0-th post-Newtonian order approximation of the SNR [41] which is given by:

$$\rho^2_{\rm opt} = \frac{4A^2}{D_L^2}\left[F_+^2(t,\alpha,\rho,\psi)(1+\cos^2\iota) + 4F_\times^2(t,\alpha,\rho,\psi)\cos^2\iota\right] I \tag{3.5}$$

where A is given by

$$A = \sqrt{\frac{5}{96}}\left(\frac{G\mathcal{M}_{\rm obs}}{c^3}\right)^{5/6} c\pi^{-2/3}, \tag{3.6}$$

while $\mathcal{M}_{obs}$ is the redshifted chirp mass, D_L is the luminosity distance, ι is the inclination angle, and F_+ and $F_\times$ are the antenna patterns for each detector network configuration (see Section 2.1.2 for their definition). We computed the antenna patterns with `pycbc` [67].
The noise curve of the detector is encapsulated in I which integrates the detector's power spectral density $S_n(f)$ as follows:

$$I = \int_{10\,\rm Hz}^{f_{\rm isco}} \frac{f^{-7/3}}{S_n(f)} df, \tag{3.7}$$

where $f_{\rm isco}$ is the orbital frequency of the innermost circular orbit for the BNS system and is approximately $4.4\,{\rm kHz}\,(M_\odot/M_{\rm tot})$, with $M_{\rm tot}$ being the total mass of the BNS system at the observer.
The optimal network SNR is then given by

$$\rho^2_{\rm opt,net} = \sum_\alpha \rho^2_{{\rm opt},\alpha} \tag{3.8}$$

where $\rho_{{\rm opt},\alpha}$ is the optimal SNR in the a^{th} detector.
However, the optimal SNR is not the one that we observe as noise fluctuations can change its value. To mimic this effect we draw an observed SNR from a Gaussian distribution with $\sigma^2 = 1$ centered around the true SNR. The selection criterion is then applied to the observed SNR. For this work, we use the detector sensitivities of the next observational runs of aLIGO-AdV [O4, O5] and of ET (see Table 3.2 for more details and Fig.2.6 for their PSD). We assume that the detectors have 100% duty cycle.

3.2 sGRB and Prompt Time Delay Simulation

We approach the simulation of the sGRB signals by establishing several simplifying assumptions for the physical properties of sGRBs. First, we assume that the matter ejected from a BNS merger emits radiation in the form of an axisymmetric gamma-ray jet, parallel to the orbital angular momentum. Consequently, the inclination angle ι of the BNS accurately represents the viewing angle of the sGRB. The jet viewing geometry is depicted in Fig.3.3
Secondly, we assumed that every BNS merger can produce a sGRB and that sGRBs have a universal jet structure. This assumption is motivated by the fact that a

Table 3.2. List of Detector Networks used for this thesis work. See Fig.2.6 for the detector sensitivities.

Detector Networks	Single Detectors	Location
O4	LIGO Hanford	Hanford, Washington, USA
	LIGO Livingston	Livingston, Louisiana, USA
	Virgo	Cascina, Italy
O5	LIGO Hanford	Hanford, Washington, USA
	LIGO Livingston	Livingston, Louisiana, USA
	LIGO India	Maharashtra, India
	Virgo	Cascina, Italy
ET	3 x ET Detectors	Italy

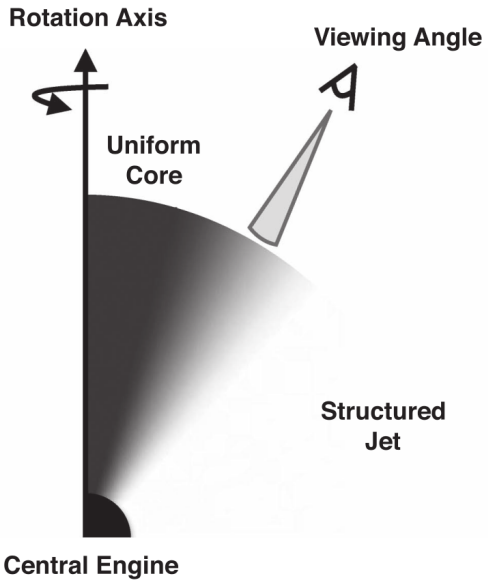

Figure 3.3. Jet viewing geometry as described in Section 3.3. Figure adapted from [7].

universal structured jet model of sGRBs is consistent with the observed distribution of viewing angles [68].
We chose a simplified model to describe the sGRB luminosity with respect to its geometry and the observer. The intrinsic luminosity of a sGRB $L(\iota;\theta_B, L_{\max})$ was set to depend solely on the viewing angle ι of the observer, the luminosity at the center of the jet $L_{\max}$ and the jet aperture angle θ_B. More precisely, we chose a Gaussian model for the jet luminosity:

$$L(\iota;\theta_B, L_{\max}) = L_{\max} e^{-\frac{\iota^2}{2\theta_B^2}}. \tag{3.9}$$

The parameters involved in our GRB simulations are:

1. The intrinsic luminosity $L(\iota;\theta_B, L_{\max})$ in the source frame, as a function of viewing angle. We assume a universal angular dependence for all sGRBs, hence $\frac{L}{L_{\max}}$ is the same for every jet.

2. The width of the jet, θ_B. For a Gaussian jet, it's just the standard deviation of the angular profile. The value chosen for θ_B is 4.5° [62], which is compatible with other SGRBs with a known jet opening angle[69, 70].

3. $L_{\max}$ is drawn from a log-normal distribution with a mean of 5×10^{51} erg s^{-1} and width of 0.56 dex, following the method of Salafia et al. [71]. This distribution is consistent with most of the observed sGRBs with known redshift [7]. Even though the angular dependence of the jet luminosity is assumed to be universal, drawing $L_{\max}$ from a distribution allows for variations in the overall luminosity of different sGRBs. These variations are the product of different energy reservoirs in the remnants or different component masses in the progenitor systems.

4. ι is the viewing angle, or the inclination of the system relative to our line of sight. It is defined as the angle between our line of sight to the binary system and the system's angular momentum.

Fig.3.4 shows the isotropic equivalent luminosity of three Gaussian jet models with different θ_B values. As the viewing angle departs from the direction orthogonal to the orbital plane, the sGRB luminosity becomes highly suppressed.

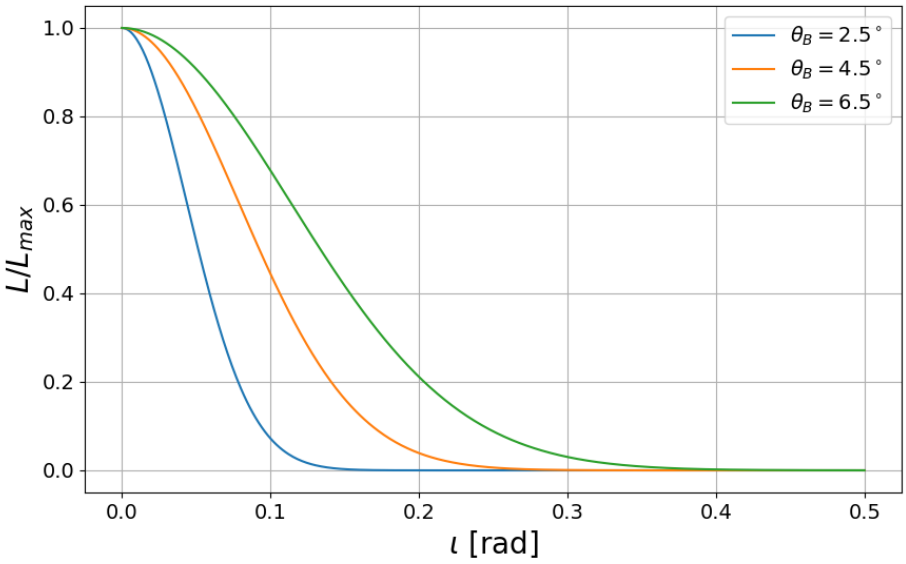

Figure 3.4. Luminosity of three Gaussian jets, with $\theta_B = 2.5°, 4.5°, 6.5°$, as a function of the inclination angle ι.

Besides the sGRB luminosity, we also need to model the GW-sGRB prompt time delay distribution. We decided to model the prompt time delay distribution as a Gaussian due to the large uncertainties on the actual prompt time delay Δt_s distribution. Zhang et al. [61] suggest a prompt time delay range: 10 ms to a few seconds. However, beyond this specific range, the knowledge about the prompt time delay distribution remains unknown. This is mainly because of two factors: an

incomplete knowledge of the sGRB jet formation mechanism and the fact that only one such event (GW170817) has been detected so far.
In this work, we assumed the prompt time delay to be distributed according to 3 different Gaussian models. These Gaussian have means $\mu_{\Delta t} = 1.7$ s and standard deviation equal to $\sigma_{\Delta t} = [1.7, 0.17, 0.017]$ s respectively.
The motivation for assuming three different values of $\sigma_{\Delta t}$ is that we want to study how the constraints on the speed of gravity and cosmology are affected by the "sharpness" of the prompt time delay distribution. In general, we expect that a "sharper" Δt_s distribution will improve our ability to constrain both z and $\hat{\alpha}_0$.
In Section 1.3 we showed that the observed time delay $\Delta t_{\rm d}$ is expressed as the sum of two terms: the time delay predicted by GR, $\Delta t_{\rm d,GR} = \Delta t_s \times (1+z)$, and an additional term representing non-GR effects, $\Delta t_{\rm d,\ non\text{-}GR} \propto \hat{\alpha}_0$. Then, if we assume GR to hold ($\hat{\alpha}_0 = 0$), the redshift z can be written as:

$$z = \frac{\Delta t_d}{\Delta t_s} - 1, \tag{3.10}$$

and the uncertainty associated with a measure of z is given by:

$$\sigma_z^2 = \left(\frac{\sigma_{\Delta t,d}}{\Delta t_s}\right)^2 + \left(\frac{\sigma_{\Delta t}\Delta t_d}{\Delta t_s^2}\right)^2 \tag{3.11}$$

where $\sigma_{\Delta t,d} \sim 0.05$ s is the measurement error on Δt_d, while $\sigma_{\Delta t}$ is the spread of the prompt time delay distribution. Consequently, a "sharper" Δt_s distribution leads to more accurate estimates of the redshift z. If we consider non-GR effects ($\hat{\alpha}_0 \neq 0$), following the previous reasoning but with a few additional steps, we can easily prove that a smaller $\sigma_{\Delta t}$ results in stricter constraints on both z and $\hat{\alpha}_0$.

3.3 sGRB detection

To model the sGRB detection we use a Fermi-GBM like experiment. We consider as detected only bursts that have a peak photon flux, calculated in the 10-1000 keV energy band, exceeding 5 $\frac{\rm ph}{s\ {\rm cm}^2}$. This is a conservative threshold when compared to the Fermi-GBM threshold of 0.5 $\frac{\rm ph}{\rm s\ cm^2}$.
Short GRB spectra typically exhibit an observer frame peak energy distribution centered between 0.5 and 1 MeV. In this work, we assume that all the energy is emitted at the flux peak.
In order to compute the energy of the peak flux we use the following E_p–$L(\iota; \theta_B, L_{\rm max})$ correlation [62]:

$$\log_{10}\left(\frac{E_p}{670\,{\rm keV}}\right) = q + m\log_{10}\left(\frac{L}{10^{52}\ \frac{\rm erg}{s}}\right) \tag{3.12}$$

where E_p is the sGRB peak energy in the source frame and the parameters q and m are set to 0.034 and 0.82, respectively. To compute the peak flux in the observer frame, it is assumed that the entire luminosity is radiated at E_p.
Then, the peak flux is:

$$F_p = \frac{L}{4\pi D_L^2}\frac{1}{E_p(1+z)} \tag{3.13}$$

In summary, a sGRB is considered detected if the peak flux surpasses the detection threshold of 5 $\frac{\text{ph}}{\text{s cm}^2}$ and E_p falls within the 10–1000 keV energy band.
For each simulated GRB, the following scheme is followed:

- First, the luminosity distance D_L and inclination angle ι of the BNS are sampled following the procedure described in Section 3.1.
- Second, as described in Section 3.2, we sample the luminosity at the center of the jet $L_{\max}$. Using ι and $L_{\max}$ the intrinsic luminosity $L(\iota; \theta_B, L_{\max})$ is derived.
- Third, using the E_p–L correlation, a peak energy value E_p is assigned.
- Finally, using the source luminosity L, peak energy E_p, and luminosity distance D_L, the peak flux F_p in the observer frame energy band (10–1000 keV) is obtained.

3.4 Catalog of Simulated GW-sGRB Detections

The procedures described in the previous Sections were used to generate a catalog of joint GW-sGRB detections for the O4, O5, and ET detector networks. Here we will discuss the population distribution obtained from these simulations, focusing on three parameters that are crucial to this study: the luminosity distance D_L, the inclination angle ι, and the observed time delay Δt_d.
Fig. 3.5, 3.6, and 3.7 show the fractions, in the cosmological inclination angle ($\cos\iota$) - luminosity distance (D_L) space, of BNS mergers for which we detect GWs and for which we simultaneously detect both GWs and sGRB relative to a mock catalog of $N = 10^6$ simulated BNS mergers. The three Figures vary with respect to the GW detector network configurations: O4, O5, or ET. Upon analyzing the figures, it is

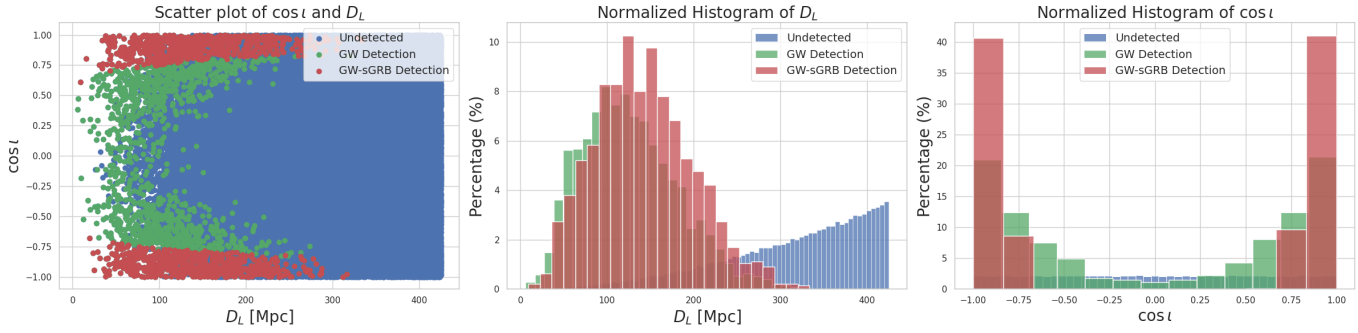

Figure 3.5. O4 detector network: fraction of BNS mergers for which we detect GWs and for which we jointly detect GWs and sGRBs relative to a mock catalog of $N = 10^6$ simulated BNS mergers. **Left panel:** fraction of BNS merger detection in the $\cos\iota - D_L$ space. **Center and Right panel:** normalized histogram of the luminosity distance and inclination angle for the different BNS merger detections.

evident that the distributions of BNS mergers, for which we detect both GW and simultaneously GW-sGRB, exhibit two pronounced peaks centered approximately at $\cos\iota \sim -1$ and $\cos\iota \sim 1$. This is a direct result of the dependence of the GW

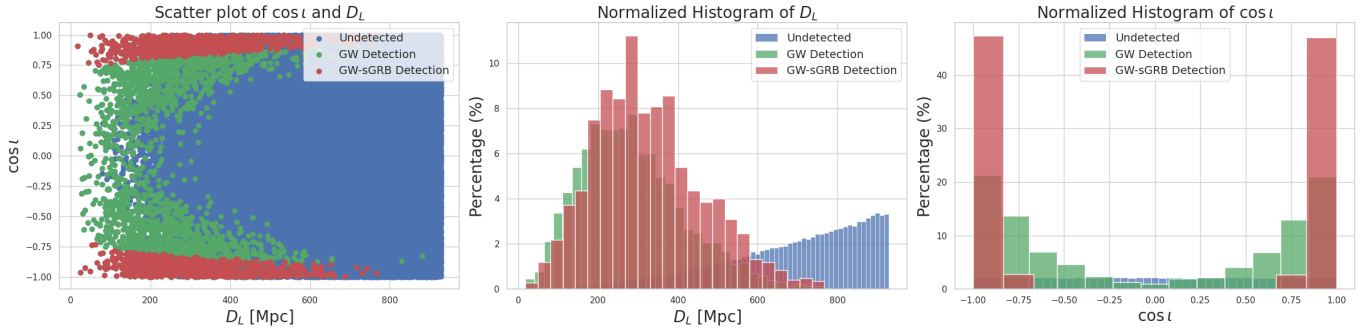

Figure 3.6. O5 detector network: fraction of BNS mergers for which we detect GWs and for which we jointly detect GWs and sGRBs relative to a mock catalog of $N = 10^6$ simulated BNS mergers. **Left panel:** fraction of BNS merger detection in the $\cos\iota - D_L$ space. **Center and Right panel:** normalized histogram of the luminosity distance and inclination angle for the different BNS merger detections.

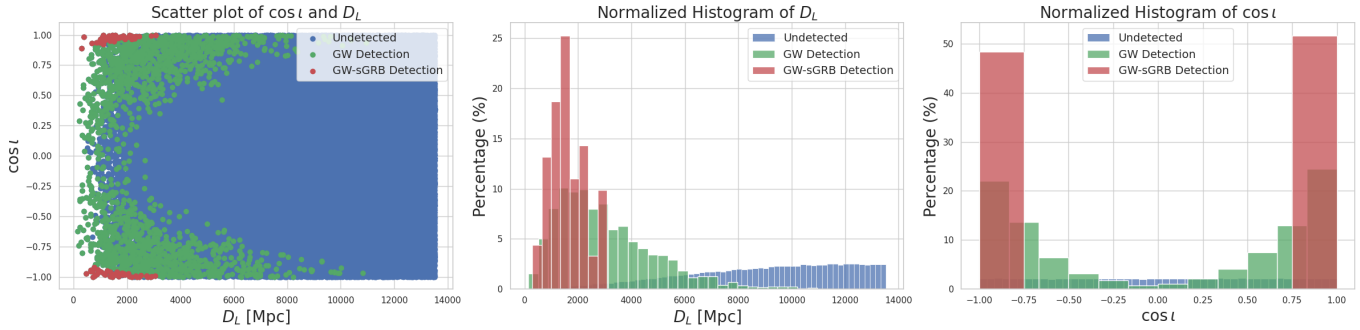

Figure 3.7. ET detector network: fraction of BNS mergers for which we detect GWs and for which we jointly detect GWs and sGRBs relative to a mock catalog of $N = 10^6$ simulated BNS mergers. **Left panel:** fraction of BNS merger detection in the $\cos\iota - D_L$ space. **Center and Right panel:** normalized histogram of the luminosity distance and inclination angle for the different BNS merger detections.

SNR and the GRB intrinsic luminosity on the inclination angle ι, which is expressed in Eq.3.5 and Eq.3.9. From these equations, we can deduce that the likelihood of detecting GWs and sGRBs is maximized when the orbital angular momentum of the BNS mergers is either aligned or anti-aligned with the line of sight of the observer. From Fig. 3.5 and 3.6, we observe that $\sim 55\%$ of GW detections in O4 and $\sim 45\%$ in O5 have a detectable sGRB emission. The detected BNS mergers reach luminosity distance values of up to $D_L \sim 300$ Mpc for O4 and $D_L \sim 800$ Mpc for O5.
For the inclination angle ι, we find that GW detections cover the entire $\cos\iota$ range, while for joint GW-sGRB detections, we will be unable to detect BNS mergers in the range $\cos\iota \in (-0.75, 0.75)$.
From Fig. 3.7 we observe that $\sim 5\%$ of GW detections in ET have a detectable sGRB emission. For GW detections, the observed BNS mergers reach $D_L \sim 11000$ Mpc, while for joint GW-sGRB detections, they reach a value of $D_L \sim 3000$ Mpc.
Fig. 3.8 show the fractions, in the luminosity distance (D_L) - detected time delay (Δt_d) space, of simulated BNS mergers for which we detect GWs and for which we jointly detect both GWs and sGRBs relative to the same mock catalog as the one of the $\cos\iota - D_L$ distribution Figures.

We can observe how, for all plots, an increase in D_L is associated with a shift as well as a broadening in the observed time delay Δt_d distribution. This is a consequence of their shared dependency on the merger redshift, z (refer to Sections 1.1 and 1.3). The D_L - Δt_d distribution could then be used to extract implicit redshift information from a set of detected time delays and luminosity distances. Intuitively, if we can measure the D_L - Δt_d relation we will be able to say something about the redshift and underlying cosmology.
However, as can be seen from Fig. 3.8, for BNS merger events detected by either O4 or O5, the observed time delay distribution does not evolve significantly with the luminosity distance. Moreover, for cases in which $\sigma_{\Delta t,d}/\Delta t_d$ is high, it will be difficult to appreciate the evolution of Δt_d as a function of D_L. For such cases, the effect of the redshift is very small and it will likely be difficult to measure it in the upcoming chapters.

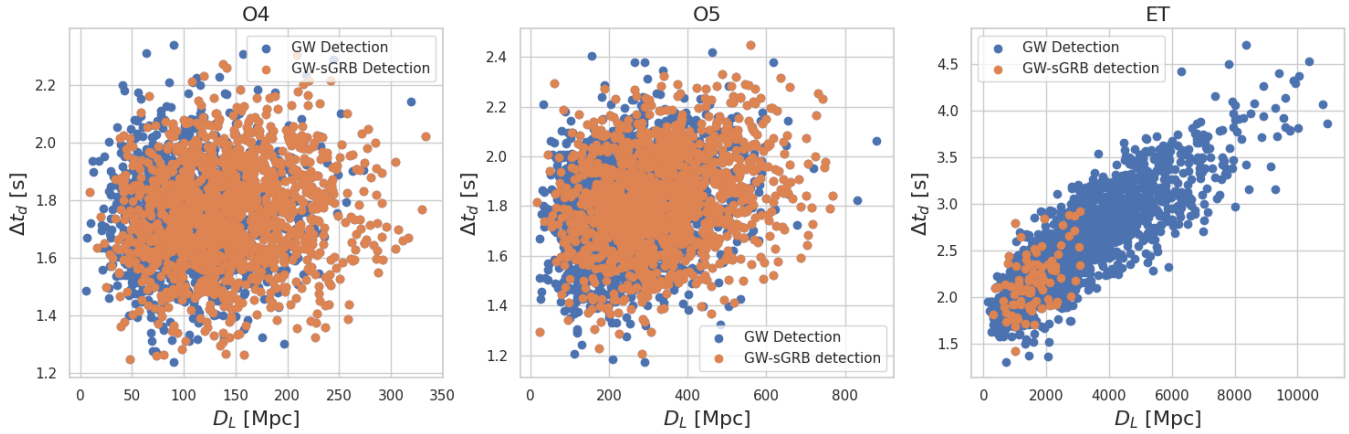

Figure 3.8. Scatter plots of the $D_L - \Delta t_d$ relation for a mock catalog of $N_{\rm obs} = 10^6$ simulated BNS mergers. Each plot corresponds to a particular detector network configuration: O4, O5, or ET. For the prompt time delay distribution, we set $\sigma_{\Delta t} = 0.17$ s. The blue points represent undetected events, while the orange points are the fraction of detected ones. Here detection means joint GW-sGRB observation. For these plots, we used the BNS merger catalogs of Fig.3.5, Fig.3.6 and Fig.3.7.

Chapter 4

Analysis

In this Chapter, I will describe how to infer the population parameters from the mock catalogs of the previous Chapter.
I will begin the Chapter in Section 4.1 with a general description, following [72], of Bayesian Hierarchical Inference. Then, in Section 4.2, I will discuss how to generate errors and posterior samples for the simulated observables. In Section 4.3, I will present `icarogw`, the Python tool that I used to infer the population properties for this work [73]. Finally, in Section 4.4, I will describe in detail the method used to carry out this analysis.

4.1 Bayesian Hierarchical Inference

In this work, we introduce a selection bias on GW-GRB detections by setting a threshold for both GW SNR and sGRB photon counting. In fact, as discussed in the previous chapter, the selection cuts prevent us from observing the entire astrophysical distribution in the $\iota - D_L$ space and creates a non-trivial observed distributions.
The goal of Bayesian Hierarchical Inference [72, 74] is to reconstruct the astrophysical population from observed data by fitting population parameters such as H_0 and $\hat{\alpha}_0$. Bayesian Hierarchical Inference allows us to compute the likelihood of obtaining $N_{\rm obs}$ observed events, each one described by a set of measured data $\vec{d_i}$ ($i \in [1, N_{\rm obs}]$), given a set of population parameters $\vec{\lambda}$.
Here, I do not derive the full expression of the Bayesian hierarchical likelihood; instead, I provide a brief discussion to explain how it is connected to this thesis work.
Given a set of population properties $\vec{\lambda}$, such as H_0 and $\hat{\alpha}_0$, the hierarchical likelihood of obtaining $N_{\rm obs}$ GW detections in a data collection $\{\vec{d}\}$, where for each event $\vec{d_i}$ is the noisy measurement of the true GW parameters $\vec{\theta_i}$, is expressed as

$$\mathcal{L}(\{\vec{d_i}\}|\vec{\lambda}) = e^{-N_{\rm exp}(\vec{\lambda})} \prod_{i=1}^{N_{\rm obs}} \int \mathcal{L}(\vec{d_i}|\vec{\theta}, \vec{\lambda}) \frac{dN}{dt_d d\vec{\theta}}(\vec{\lambda})\, d\vec{\theta}\, dt_d. \tag{4.1}$$

In the above equation, $N_{\rm exp}(\vec{\lambda})$ is the number of expected GW detections, while $\mathcal{L}(\vec{d_i}|\vec{\theta}, \vec{\lambda})$ is the GW likelihood, which quantifies how well we can measure $\vec{\theta}$ and $\vec{\lambda}$

from a single event detection $\vec{d}$. The quantity $\frac{dN}{dt_d d\vec{\theta}}$ is the source rate in detector time t_d. The likelihood of Eq. 4.1 is similar to the one of a Poisson process; however, it incorporates selection biases. By assuming a $\pi(N_{\rm exp}) \propto 1/N_{\rm exp}$ prior on the expected number of detections, Eq. 4.1 can be written in a more compact form:

$$\mathcal{L}(\{\vec{d}_i\}|\vec{\lambda}) = \prod_{i=1}^{N_{\rm obs}} \frac{\int \mathcal{L}(\vec{d}_i|\vec{\theta},\vec{\lambda}) \frac{dN}{dt_d d\vec{\theta}}(\vec{\theta}|\vec{\lambda})\, d\vec{\theta}\, dt_d}{\int p_{\rm det}(\vec{\theta},\vec{\lambda}) \frac{dN}{dt_d d\vec{\theta}}(\vec{\theta}|\vec{\lambda})\, d\vec{\theta}\, dt_d}, \tag{4.2}$$

where $p_{\rm det}(\vec{\theta},\vec{\lambda})$ is a detection probability that includes all selection thresholds. The detection probability $p_{\rm det}(\vec{\theta},\vec{\lambda})$ is given by:

$$p_{\rm det}(\vec{\theta},\vec{\lambda}) = \int_{\vec{d}>\rm threshold} \mathcal{L}(\vec{d}|\vec{\theta},\vec{\lambda}) d\vec{d} \tag{4.3}$$

where we integrate over the detectable values of $\vec{d}$ (above detection threshold).
Let us now calculate the rate. For this work, the single event parameters $\vec{\theta}$ are the luminosity distance D_L and the detector GW-GRB time delay Δt_d. Then, in Eq. 4.2, the rate model is

$$\frac{dN}{dt_d d\vec{\theta}} = \frac{dN}{dt_d dD_L d\Delta t_d}. \tag{4.4}$$

However, all our population models are written in terms of source frame parameters (see the previous Chapter for more details), namely Δt_s and z. We then need to perform a change of variables. The detection rate is written in terms of the source rate as:

$$\frac{dN}{dt_d dD_L d\Delta t_d} = \frac{dN}{dt_s dz d\Delta t_s}\frac{dt_s}{dt_d}\frac{1}{{\rm det}J_{D\to S}} = \frac{dN}{dt_s dz d\Delta t_s}\frac{1}{(1+z)^2|\frac{\partial D_L}{\partial z}|} \tag{4.5}$$

In the above equation, a factor $\frac{1}{1+z}$ results from the difference between source-frame t_s and detector-frame time t_d, while ${\rm det}J_{D\to S}$ is the determinant of the Jacobian associated to the change of variables between the detector and source frames:

$${\rm det}J_{D\to S} = |\frac{\partial D_L}{\partial z}(1+z)| \tag{4.6}$$

with:

$$\frac{\partial D_L}{\partial z} = \frac{D_L(z)}{1+z} + \frac{c(1+z)}{H_0}\frac{1}{E(z)}. \tag{4.7}$$

In Eq. 4.5, the factor $\frac{dN}{dz d\Delta t_s dt_s}$ is the source rate in terms of the redshift z and prompt time delay Δt_s. This can be written as:

$$\frac{dN}{dt_s dD_L d\Delta t_s} = \frac{dN}{dt_s dV_c}\frac{dV_c}{dz} p_{\rm pop}(\Delta t_s|\vec{\lambda}), \tag{4.8}$$

where $p_{\rm pop}(\Delta t_s|\vec{\lambda})$ is the prompt time delay Gaussian distribution, which was described in Section 3.2. The rate, as discussed in Section 3.1, is given by $\frac{dN}{dt_s dV_c} = R(z,\vec{\lambda}) = R_0\Phi(z,\vec{\lambda})$, where Φ is the Madau parametrization, while R_0 is the merger

rate today (see Section 3.1 for more details).
Putting everything together, the detector rate model can be rewritten as:

$$\frac{dN}{dt_d dD_L d\Delta t_d} = R(z,\vec{\lambda})\frac{dV_c}{dz}p_{\rm pop}(\Delta t_s|\vec{\lambda})\frac{1}{(1+z)^2|\frac{\partial D_L}{\partial z}|} \tag{4.9}$$

By substituting Eq. 4.9 in Eq. 4.2, we find that the full expression of the hierarchical likelihood is given by:

$$\mathcal{L}(\{\vec{d_i}\}|\vec{\lambda}) = \prod_{i=1}^{N_{\rm obs}} \frac{\int \mathcal{L}(\vec{d_i}|D_L,\Delta t_d,\vec{\lambda})R(z,\vec{\lambda})\frac{dV_c}{dz}p_{\rm pop}(\Delta t_s|\vec{\lambda})\frac{1}{(1+z)^2|\frac{\partial D_L}{\partial z}|}\,dD_L d\Delta t_d\,dt_d}{\int p_{\rm det}(D_L,\Delta t_d,\vec{\lambda})R(z,\vec{\lambda})\frac{dV_c}{dz}p_{\rm pop}(\Delta t_s|\vec{\lambda})\frac{1}{(1+z)^2|\frac{\partial D_L}{\partial z}|}\,dD_L d\Delta t_d\,dt_d}, \tag{4.10}$$

where z is to be understood as a function of the luminosity distance D_L and the cosmological model.

4.2 Errors and Posterior Samples Generation

In real-world experiments, the measurements of luminosity distance and time delay are recorded by an experimental apparatus contaminated by noise. As such, both the luminosity distance and detector time delay are not perfectly measured. Typically, errors for GW signals are generated using complex Bayesian sampling techniques, which rely on sampling from the GW likelihood. For this study, however, in order to ease the computational load, we chose to use simplified likelihood models to generate errors.
For each simulated value of the luminosity distance, we decided to generate the "noisy" value of D_L by using the following likelihood [75]:

$$\mathcal{L}_{\rm noise}(D_L^{\rm obs}|D_L^{\rm true}) = \mathcal{N}(D_L^{\rm obs}|\mu = D_L^{\rm true}, \sigma = 0.2\cdot D_L^{\rm true}). \tag{4.11}$$

where $D_L^{\rm true}$ is the true physical value of the luminosity distance (D_L in the previous section), while $D_L^{\rm obs}$ is its measured noisy counterpart. For detected time delays Δt_d, we decided to sample the noise from a Gaussian distribution:

$$\mathcal{L}_{\rm noise}(\Delta t_d^{\rm obs}|\Delta t_d^{\rm true}) = \mathcal{N}(\Delta t_d^{\rm obs}|\mu = \Delta t_d^{\rm true}, \sigma = 0.05s). \tag{4.12}$$

where the small standard deviation reflects the high precision with which we can measure the GW-sGRB time delay in real experiments, such as in the case of GW170817.
We also remember that noise fluctuations in the detector alter the observed SNR relative to its intrinsic value which is given by (see Section 3.1.1):

$$\rho_{\rm opt}^2 = \frac{4A^2}{D_L^2}\left[F_+^2(t,\alpha,\rho,\psi)(1+\cos^2\iota) + 4F_\times^2(t,\alpha,\rho,\psi)\cos^2\iota\right] I. \tag{4.13}$$

To include this effect, for each simulated event, we sample the observed SNR from a Gaussian distribution with standard deviation of 1:

$$\mathcal{L}_{\rm noise}(\rho_{\rm obs}|\rho_{\rm true}) = \mathcal{N}(\rho_{\rm obs}|\mu = \rho_{\rm true}, \sigma = 1). \tag{4.14}$$

Given Eq.4.11, 4.12, and 4.14, the overall GW likelyhood of Eq. 4.10 is given by:

$$\mathcal{L}(\rho_{\rm obs}, D_L^{\rm obs}, \Delta t_d^{\rm obs}|\rho_{\rm true}, D_L^{\rm true}, \Delta t_d^{\rm true}) = \mathcal{L}(D_L^{\rm obs}|D_L^{\rm true})\mathcal{L}(\Delta t_d^{\rm obs}|\Delta t_d^{\rm true})\mathcal{L}(\rho_{\rm obs}|\rho_{\rm true}). \tag{4.15}$$

However, in `icarogw`, for each GW detection, we need to provide posterior samples (PEs), namely the possible values of ($\Delta t_d^{\rm true}$,$D_L^{\rm true}$) from which the observed ($\Delta t_d^{\rm obs}$,$D_L^{\rm obs}$) were generated. PEs are sampled from the posterior $p(\rho_{\rm true}, D_L^{\rm true}, \Delta t_d^{\rm true}|\rho_{\rm obs}, D_L^{\rm obs}, \Delta t_d^{\rm obs})$.
Before going on, we note that $\rho_{\rm true}$ is a function of $D_L^{\rm true}$ (see Eq. 4.13). For this study, we assume that we can perfectly measure all BNS parameters of Eq. 4.13, except D_L. Then, if all other BNS parameters are known, $\rho_{\rm true}$ can be directly derived from $D_L^{\rm true}$. We can thus work with a posterior that is a sole function of $D_L^{\rm true}$ and $\Delta t_d^{\rm true}$. Using the Bayes theorem, the posterior on $D_L^{\rm true}$ and $\Delta t_d^{\rm true}$ is given by:

$$\begin{aligned} p(D_L^{\rm true}, \Delta t_d^{\rm true}|D_L^{\rm obs}, \Delta t_d^{\rm obs}) = \mathcal{L}(D_L^{\rm obs}|D_L^{\rm true})\mathcal{L}(\Delta t_d^{\rm obs}|\Delta t_d^{\rm true}) \\ \times \mathcal{L}(\rho_{\rm obs}|\rho_{\rm true}(D_L^{\rm true}))\pi_{PE}(D_L^{\rm true}, \Delta t_d^{\rm true}) \end{aligned} \tag{4.16}$$

We used a rejection sampling technique to draw PEs from Eq. 4.16. In doing so, we used uniform priors for $D_L^{\rm true}$ and $\Delta t_d^{\rm true}$.
In Fig. 4.1 we show the corner plots for the posterior samples of $D_L^{\rm true}$ and $\Delta t_d^{\rm true}$ for a signal with SNR $\rho_{\rm obs} = 13$ and one with SNR $\rho_{\rm obs} = 102$. The true values of

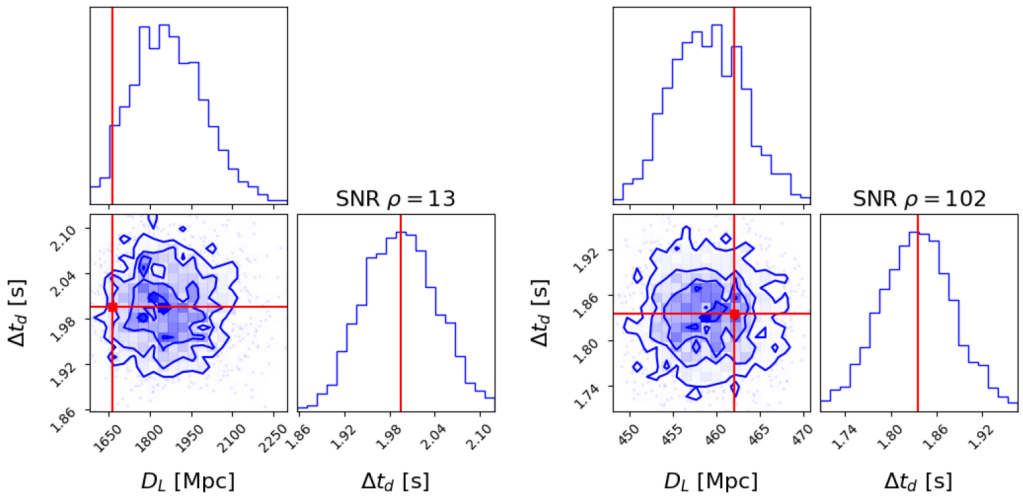

Figure 4.1. Posterior samples of $D_L^{\rm true}$ and $\Delta t_d^{\rm true}$ for a signal with SNR $\rho_{\rm obs} = 13$ and one with SNR $\rho_{\rm obs} = 102$. Both events have been detected by ET. The red lines represent the true values of $D_L^{\rm true}$ and $\Delta t_d^{\rm true}$.

$D_L^{\rm true}$ and $\Delta t_d^{\rm true}$ are usually included in a reasonably credible interval. It has to be noted that the only Gaussian posterior is the one on $\Delta t_d^{\rm true}$. The posterior on $D_L^{\rm true}$ has a non-trivial structure, which is the result of the dependency of the likelihood's standard deviation on $D_L^{\rm true}$, and the inverse proportionality of $\rho^{\rm true}$ to $D_L^{\rm true}$. This usually results in an asymmetric posterior for high distances.

4.3 Numerical Evaluation of the Hierarchical Likelihood with icarogw

The hierarchical likelihood in Eq. (4.2) incorporates several crucial quantities to the inference problem. In the following, I will outline how we can compute these quantities and use them to calculate the full hierarchical likelihood.
The first central quantity is the single-event GW likelihood $\mathcal{L}(\vec{d_i}|\vec{\theta},\vec{\lambda})$. In general, we are provided with $N_{s,i}$ posterior samples (PEs) which are drawn via stochastic sampling from the following distribution

$$p(\vec{\theta}|\vec{d_i},\vec{\lambda}) \propto \mathcal{L}(\vec{d_i}|\vec{\theta},\vec{\lambda})\pi_{\rm PE}(\vec{\theta}), \tag{4.17}$$

where $\pi_{\rm PE}(\vec{\theta})$ is the prior used to generate the samples. In layman's terms, PE samples represent the possible true values of $\vec{\theta}$, given the observed ones $\vec{d}$. We can thus evaluate the likelihood integral in the numerator of Eq. (4.10) by summing over PE samples:

$$\int \mathcal{L}(\vec{d_i}|\theta)\frac{dN}{dtd\vec{\theta}}(\vec{\lambda})d\vec{\theta} \approx \frac{1}{N_{s,i}}\sum_{j=1}^{N_{s,i}}\frac{1}{\pi_{\rm PE}(\vec{\theta}_{i,j})}\frac{dN}{dtd\vec{\theta}}(\vec{\lambda})\Big|_{i,j} = \frac{1}{N_{s,i}}\sum_{j=1}^{N_{s,i}} w_{i,j}, \tag{4.18}$$

where the index i refers to the event and the index j to the posterior samples of the events. Here, $w_{i,j}$ is a weight of dimension equal to the number of events generated per unit of time.
Since Eq. (4.18) is evaluated with a finite sum over posterior samples, we introduce a numerical stability estimator, which is the effective number of posterior samples per event i [76]:

$$N_{{\rm eff},i} = \frac{(\sum_j^{N_{s,i}} w_{i,j})^2}{\sum_j^{N_{s,i}} w_{i,j}^2}. \tag{4.19}$$

This estimator quantifies how many samples per event are contributing to the evaluation of the integral. Typically, in population analyses such as [77], it is required to have at least an effective number of posterior samples equal to 20 for each event and population model supported by the analysis. If this requirement is not met, we assign a null likelihood to the population model, as the model's reliability cannot be confirmed.
The second central quantity is the normalization factor in the denominator of Eq. 4.10 $\rm I_{norm}$, which accounts for selection biases. This integral is a function of the detection probability. Typically, we lack an analytical form for the detection probability. The current approach to assess selection biases is to use Monte Carlo simulations of injected and detected events, commonly referred to as "injections" [78]. Injections help evaluate the accessible volume within the parameter space and correct for any selection bias.
We can thus compute the integral in the denominator of Eq.4.10 through Monte Carlo integration over detected injections:

$$\rm I_{norm} \approx \frac{1}{N_{gen}}\sum_{j=1}^{N_{det}}\frac{dN}{dtd\vec{\theta}_j}\frac{1}{\pi_{\rm inj}(\vec{\theta}_j)} = \frac{1}{N_{gen}}\sum_{j=1}^{N_{det}} s_j \tag{4.20}$$

where $N_{\rm det}$ are the detected injections out of $N_{\rm gen}$ total injections generated from a prior $\pi_{\rm inj}(\vec{\theta})$. Here, s_j is a weight with the dimension of a rate of events. However, it's important to note the fundamental difference with Eq. 4.18: the injection prior $\pi_{\rm inj}(\vec{\theta})$ must be correctly normalized to obtain a reasonable value of $N_{\rm det}$. While an incorrect normalization of $\pi_{\rm PE}(\vec{\theta})$ used in Eq. 4.18 results only in an overall normalization factor to the overall hierarchical likelihood [76] .
In a similar way to Eq. 4.19, we can define a numerical stability estimator, the effective number of injections:

$$N_{\rm eff,inj} = \frac{\left[\sum_{j=1}^{N_{\rm det}} s_j\right]^2}{\left[\sum_{j=1}^{N_{\rm det}} s_j^2 - N_{\rm gen}^{-1}(\sum_{j=1}^{N_{\rm det}} s_j)^2\right]} \tag{4.21}$$

A standard value for numerical stability is $N_{\rm eff,inj} > 4N_{\rm obs}$. In summary, putting everything together, we find that the hierarchical likelihood of Eq. 4.10 can be rewritten as:

$$\ln[\mathcal{L}(\{\vec{d}\}|\vec{\lambda})] \approx -N_{\rm obs} \ln\left[\frac{1}{N_{\rm gen}} \sum_{j=1}^{N_{\rm det}} s_j\right] + \sum_{i=1}^{N_{\rm obs}} \ln\left[\frac{1}{N_{s,i}} \sum_{j=1}^{N_{\rm s,i}} w_{i,j}\right] \tag{4.22}$$

4.3.1 Structure of the code

The ***I**nferring **C**osmology and **A**st**r**ophysics with **O**bservations of **G**ravitational **W**aves* (`icarogw`) is a Python tool developed to infer the population properties of compact binary coalescences (CBCs) observed through GWs [73]. `icarogw` uses a user-friendly Python environment for performing Hierarchical Bayesian Inference, which requires few essential "ingredients": (i) PE samples from a finite number of observations, (ii) a set of injections for calculating the explorable volume in the parameter space, and (iii) a rate, or parameter population distributions model.
`icarogw` contains a range of modules used for numerically computing the hierarchical likelihood of Eq. 4.22. The modules are separated into core and support modules. The core modules are necessary for calculating the hierarchical likelihood, even when applying `icarogw` for non-GW applications. The support modules are composed of utility functions, which may be used by the core modules. These modules predominantly contain functions for GW applications. A general description of the modules is as follows: the `wrappers.py` module contains Python classes dedicated to the events production rate $\frac{dN}{dt_d d\vec{\theta}}$. It is essential for each rate class to specify which are the event-level parameters $\vec{\theta}$ and the population-level parameters $\vec{\lambda}$. In addition, instructions for updating the rate model from the population parameters $\vec{\lambda}$ are also included in each rate class.
The `posterior_samples.py` module hosts classes for allocating PE samples which represent possible true values for the event parameters. In parallel, the `injections.py` module contains a class used to assign the injections required for the assessment of selection bias. Both the single-event PE samples and injections are expected to be provided with the prior samples used for their generation.
The hierarchical likelihood used by the Python package bilby [79] is contained within the `likelihood.py` module.

In the schematic view of the icarogw modules (Fig. 4.2), the core modules are displayed in red boxes while the support modules are highlighted in a yellow box. The logic of icarogw operation proceeds in the following sequence:

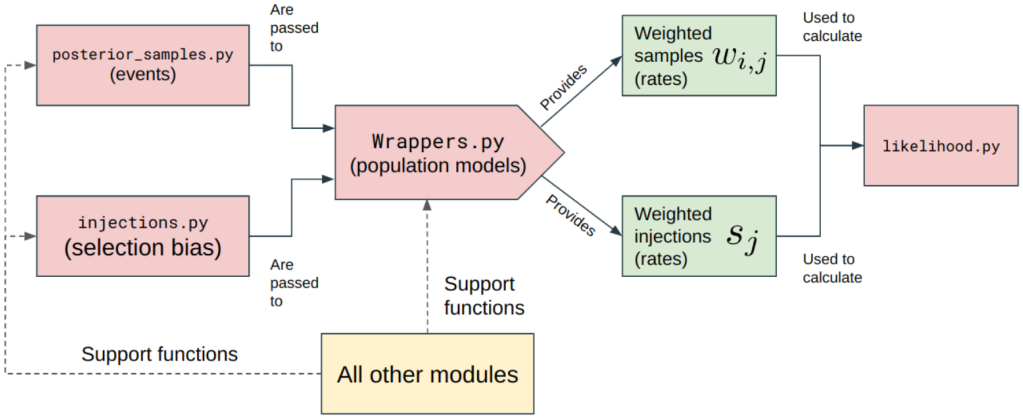

Figure 4.2. icarogw modules structure [73] Core modules used for the general hierarchical Bayesian inference are colored in red, while support modules mostly used for GW applications are colored in yellow. The green boxes highlight the computation of the rate weights which are needed for the calculation of the hierarchical likelihood.

1. First, injections and PE samples are allocated using classes from `injections.py` and `posterior_samples.py`.

2. Second, these injections and PE samples are passed to the population models in the `wrappers.py` module to evaluate the coefficients $w_{i,j}$ and s_j defined in Eq. 4.22. If required, support modules can be invoked, e.g. for utilizing cosmological models or specific probabilistic distributions. The most common routines stem from the `priors.py` module, which contains probabilistic models, and the `cosmology.py` module, containing routines for cosmological calculations.

3. Finally, the calculated rate coefficients $w_{i,j}$ and s_j are sent to the `likelihood.py` module to compute the hierarchical likelihood as per Eq, 4.22. icarogw calculates two numerical stability estimators for each population model: the effective number of posterior samples for each event in Eq. 4.19 and the effective number of injections in Eq. 4.21. If the numerical estimators fall below the user-set threshold, Icarogw outputs $\ln[\mathcal{L}(\{\vec{d}\}|\vec{\lambda})] = -\infty$, thus rejecting the population model.

4.4 Extension and Application of icarogw to Time Delays

As stated before, icarogw has primarily been developed for GW science involving CBCs. Hence, the module `wrappers.py` in icarogw already includes coded CBC

merger rate models (expressed in terms of source frame masses and redshifts). However, before this work, `icarogw` did not contain either rate models or utilities capable of handling GW-GRB time delays.
One of the first steps in my thesis work was to implement in `icarogw` utility functions to compute the time delay in modified gravity for both the source and detector frame. I then implemented the rate model defined in Eq. 4.10.
This rate is handled by the custom class `time_delay_rate()` in the `wrappers.py` module. The initialization of the rate model requires a cosmological model, a model for the prompt time delay distribution, and a model for the rate evolution in redshift. As discussed in Section 3, we initialized the source rate model with a standard flat ΛCDM cosmology, a Gaussian prompt time delay distribution, and a Madau-SFR rate for the merger redshift (see List. 4.1).

```
cw=icarogw.wrappers.FlatLambdaCDM_wrap(zmax=10.) #Initialize a
    wrapper for the cosmological model
tdw=icarogw.wrappers.time_delay_prior_gaussian() #Initialize a time
    delay Gaussian model
rw=icarogw.wrappers.rateevolution_Madau() #Initialize a Madau model
    for the rate
rate_model = icarogw.wrappers.time_delay_rate(cw,tdw,rw,scale_free=
    True) # Collate everything in one single rate, note the flag
    scale_free that tells we don't want to use R0/
```

Listing 4.1. source model inizialization.

In order to evaluate the hierarchical likelihood and correct for selection bias, we need to generate both a set of PE of injections.
In `icarogw`, the process of generating a set of detected injections is logically equivalent to the one of creating a set of observed events, albeit with certain distinct choices. We must generate the injection set from a prior wide enough so that we are sure that our injection set captures all possible values of the *noiseless* GW parameters $\vec{\theta}$ that we might be able to detect even with noise fluctuations. Remember that injections are used to measure the fraction of detectable events.
The approach we used is the following: we generate a set of $N_{\rm gen}$ BNS events (with joint GW-sGRB emission) in the exact same way as in Section 3. Thus, the luminosity distance $D_L^{\rm true}$ is generated from the usual Madau-Dickinson prior [65]. However, the $\Delta t_d^{\rm true}$ values are directly generated from a flat prior with different ranges for different detection scenarios. These ranges are chosen to be wide enough to capture all detectable observables.
We then save the *noiseless* $\vec{\theta}=(D_L^{\rm true},\Delta t_d^{\rm true})$ values for each event with observed SNR and peak Flux above the detection thresholds. These are our injections. For this work, we chose $N_{\rm gen}=10^5$. We load the set of PE samples and injections into the `posterior_samples_catalog()` and `injections()` classes respectively (see List. 4.2 and List. 4.3). Both the PE samples and injections are passed along with their generation priors. The `injections()` class requires the prior to be correctly normalized.

```
# Icarogw wants that you store all the PE in a dict of
    posterior_samples classes
posterior_dict = {}
for i in range(len(pe_lum_distance)): # Loop on all the events you
    detect
```

```
    posterior_dict[str(i)] = icarogw.posterior_samples.posterior_samples({
        'observed_time_delay': pe_observed_time_delay[i],
        'luminosity_distance': pe_lum_distance[i]
    },  # You need to provide the PE in a dict, IMPORTANT field of the dict is
        # equal to the variable needed to evaluate the rate
        prior=np.ones(2000) # PE have been generated with uniform prior, so here
        # I pass a constant. NOT IMPORTANT if not normalized
    )
posterior_dict = icarogw.posterior_samples.posterior_samples_catalog(posterior_dict)
```

Listing 4.2. allocation of PEs in the `posterior_samples_catalog()` class.

```
injections_dict={'observed_time_delay':inj_observed_time_delays,'luminosity_distance':inj_lum_distance} # Initialize the dictionary

# Here we initialize the injection set
inj=icarogw.injections.injections(injections_dict,
                                  prior=inj_prior,
                                  ntotal=len(inj_lum_distance),
                                  Tobs=1)
```

Listing 4.3. allocation of injections in the `injections()` class.

We initialize the hierarchical likelihood using the PE samples, injections, and rate model, to derive the posterior on the Δt_s distribution, $\hat{\alpha}_0$, and $H0$ (we assume all other parameters involved in the rate as known). To accomplish this, we employ a Markov Chain Monte Carlo (MCMC) algorithm, specifically the `emcee` sampling algorithm from `bilby`, to sample these parameters.

4.4.1 EMCEE

Emcee, or the MCMC Hammer, is an ensemble-based Markov chain Monte Carlo (MCMC) sampling tool [80, 79].
This algorithm utilizes a modified version of the Metropolis-Hastings (M–H) algorithm [81, 82] with the inclusion of a parallel stretch move [83]:

1. **Initialization**: An ensemble of "walkers" is initialized, each representing a point in the parameter space $\vec{\lambda}$.

2. **Movement (Parallel Stretch Move)**: For each walker i at time step t, a new position $x_i(t+1)$ is proposed. This position is a random step from the current position of another randomly chosen walker $x_j(t)$:

$$x_i(t+1) = x_j(t) + Z \times [x_i(t) - x_j(t)]. \tag{4.23}$$

   Here, Z is a stretch factor following a distribution $p(Z) = \frac{1}{\sqrt{Z}}$ if $Z \in [\frac{1}{a}, a]$ and 0 otherwise, where $a > 1$ is a scale parameter, typically set to 2 [83].

3. **Probability Calculation**: The posterior probability of the proposed position is calculated $P(x_i(t+1)|D)$ (here D represent the observed events).

4. **Decision (Metropolis-Hastings Acceptance Rule)**: The Metropolis-Hastings rule is applied to decide whether to move the walker to the proposed position. The acceptance probability (α) is calculated as:

$$\alpha = \min(1, (P(x_i(t+1)|D)/P(x_i(t)|D)) \times (Z^{n-1})). \tag{4.24}$$

   If α equals or exceeds 1, the proposed move is always accepted. If α is less than 1, the proposed move may still be accepted, but only with a probability of α. This provision allows for occasional exploratory moves towards less probable positions, mitigating the risk of local maxima entrapment.

5. **Repetition and Convergence**: Steps 2-4 are iteratively performed until the walker ensemble's distribution aligns closely with the target probability distribution. The final positions of the walkers then provide estimates of the parameters and their uncertainties.

In this work, for all different inference Scenarios, we chose to run emcee for 10000 iterations using 10 independent Markov chains.

Chapter 5

Forecast on Speed of Gravity and Cosmology

In this Chapter, I present the results derived from applying the inference scheme of Chapter 4 over the mock catalog of joint GW-sGRB observations, described in Chapter 3. This scheme is employed to estimate the following population parameters: speed of gravity $\hat{\alpha}_0$, Hubble constant H_0, and prompt time delay distribution parameters $(\mu_{\Delta t}, \sigma_{\Delta t})$.
I will start the Chapter by describing the data and priors used for the inference process in Section 5.1. Then I will discuss the 3 different inference Scenarios considered for this thesis:

- Scenario I: joint inference of $(\hat{\alpha}_0, \mu_{\Delta t}, \sigma_{\Delta t})$, with H_0 fixed to the Planck value, i.e. $H_0 = 67.66 \frac{\text{km}}{s\ \text{Mpc}}$ [63].
- Scenario II: joint inference of $(H_0, \mu_{\Delta t}, \sigma_{\Delta t})$, with $\hat{\alpha}_0$ fixed to the GR value, i.e., $\hat{\alpha}_0 = 0$.
- Scenario III: joint inference of all four parameters $(\hat{\alpha}_0, H_0, \mu_{\Delta t}, \sigma_{\Delta t})$.

I will analyze the results for Scenarios I, II, and III in Sections 5.2, 5.3, and 5.4 respectively.

5.1 Data and Priors Used for the Analysis

For this work, we chose to analyze sets of $N_{\text{obs}} = [4, 10, 100, 1000]$ detected events, generated according to Section 3. The choice to start with $N_{\text{obs}} = 4$ detections is motivated by the fact that in Scenario III, where we jointly infer 4 parameters, it would be impossible to jointly constrain all parameters with less than 4 observations. Each set will differ by the number of observations N_{obs}, the detector network configuration [O4, O5, ET], and the standard deviation of the prompt time delay Δt_s distribution $\sigma_{\Delta t} = [1.7, 0.17, 0.017]$ s.
For the prompt time delay distribution, I used a uniform prior between $[0, 5]$ s for the mean $\mu_{\Delta t}$ and a flat-in-log prior between $[10^{-3}, 10]$ s for the standard deviation $\sigma_{\Delta t}$. The choice to use a flat-in-log prior within this range stems from the different Δt_s parameters: $\sigma_{\Delta t} = [1.7, 0.17, 0.017]$ s. The flat-in-log distribution guarantees

a uniform prior distribution across all these orders of magnitude. For the Hubble constant, we chose a uniform prior distribution between $[30, 140]$ km/s/Mpc. Finally, for $\hat{\alpha}_0$ we used a uniform prior with a range dependent on the detection and simulation Scenario, spanning an order of magnitude from $\sim 10^{-15}$ to $\sim 10^{-19}$. The value of the remaining population parameters is fixed for all inference Scenarios. In Tab. 5.1 we list the population parameters with their prior distribution. For the

Table 5.1. List of priors for the population parameters as described in Section 5.1

Parameter	True Value	Prior Distribution	Distribution range
$\mu_{\Delta t}$	$1.7s$	Uniform	[0,5] s
$\sigma_{\Delta t}$	[1.7,0.17,0.017] s	logUniform	[10^{-3},10] s
H_0	67.66 km/s/Mpc	Uniform	[30,140] km/s/Mpc
Ω_M	0.315	Fixed	
$\hat{\alpha}_0$	0	Uniform	Variable
γ	2.7	Fixed	
k	6	Fixed	
z_p	2.4	Fixed	

hierarchical analysis, we used 2000 posterior samples for each event. The posterior samples encode our uncertainties on the true value of the luminosity distance D_L and the observed time delay Δt_d and they are generated according to Section 4.2. Also, it is crucial to set a threshold value for both the numerical stability estimators $N_{\text{eff,PE}}$ and $N_{\text{eff,inj}}$. These two thresholds quantify the minimum number of injections and PEs per event that are necessary to evaluate the selection biases. If, for a given population model, we do not reach these numbers the MCMC will not accept the population model.
For this work, following [73] we set the following thresholds: $N_{\text{eff,PE}} > 20$ and $N_{\text{eff,inj}} > 4N_{\text{obs}}$. During our runs, we never experienced any problem with $N_{\text{eff,inj}}$. However, for 1000 GW signals, and true value of $\sigma_{\Delta t} = 0.017$ s, we were unable to impose $N_{\text{eff,PE}} > 20$.
The sharpness of the prompt time delay Δt_s (Gaussian) distribution and the large number of detections significantly increase the chances for at least one noisy measurement of the observed time delay $\Delta t_d^{\text{noise}}$ to deviate considerably from the true values Δt_d^{true} distribution. This is depicted in Fig. 5.1. As a result, the weights $w_{i,j}$, calculated over the PEs of such noisy measure $\Delta t_d^{\text{noise}}$, are more likely to yield extremely small or zero values). This is what prevents us from getting $N_{\text{eff,PE}} > 20$ for each single detected event and it makes the computation of the hierarchical likelihood numerically unstable. To solve this problem, we opted to lower the threshold and set $N_{\text{eff,PE}} > 5$ just for these particular Scenarios. However, this constraint is insufficient to ensure numerical stability. As a consequence, the results of this type of case are not as reliable as the others.

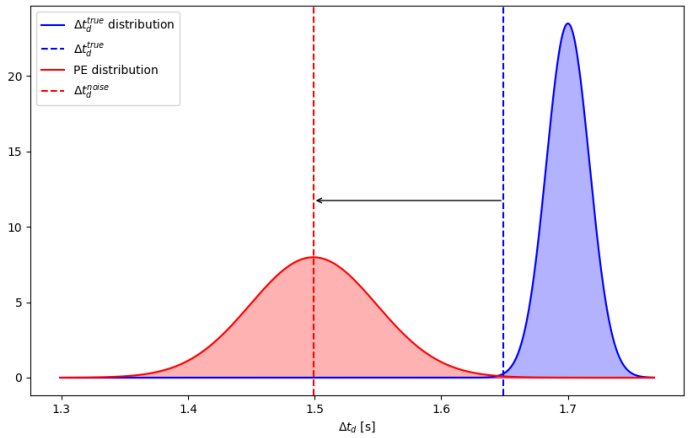

Figure 5.1. Schematic view of the problem encountered in this Section. Since $\sigma_{\Delta t} = 0.017s < 0.05$ s, The PE distribution of the noisy measurement $\Delta t_d^{\rm noise}$ only partially overlaps with the true value $\Delta t_d^{\rm true}$, making the numerical integration difficult.

5.2 Scenario I: Joint Constraints on Speed of Gravity and Prompt Time Delay Distribution

For Scenario I, we find that future observations will allow us to jointly constraint the speed of gravity and the prompt time delay distribution.
In Tab. 5.2 we report our forecasts on the constraints for $(\hat{\alpha}_0, \mu_{\Delta t}, \sigma_{\Delta t})$, while, Fig. 5.2 shows the relative error on the parameters that we obtain as we analyze more GW-sGRB events. All parameters are found within 3σ of their true values. We find that the speed of gravity can be constrained with an uncertainty $\Delta\hat{\alpha}_0$ of order $\sim 2 \cdot 10^{-16} - 10^{-19}$ (see Tab. 5.2). These constraints are up to 10^4 times better than those derived from the GW170817 measurement (refer to Section 1.4.2). In other words, we find that we will be able to jointly constrain the speed of gravity and prompt time delay distribution. Moreover, the strength of the $\hat{\alpha}_0$ constraints depend on the number of observed events $N_{\rm obs}$, and on both the detection (O4, O5, ET) and prompt time delay model ($\sigma_{\Delta t} = [1.7, 0.17, 0.017]$ s) Scenarios.
In fact, the Bernstein-von Mises theorem [84] asserts that under mild assumptions (such as the smoothness and continuity of the likelihood and prior distribution) and with a large sample size $N_{\rm obs}$, the posterior distribution converges to a normal distribution centered at the maximum likelihood estimate with a standard deviation $\propto \frac{1}{\sqrt{N_{\rm obs}}}$. For $\hat{\alpha}_0$, this gaussian regime is qualitatively reached when $N_{\rm obs} \gtrsim 4$.
We find, in agreement with Section 3.2, that a "sharper" prompt time delay Δt_s distribution, i.e. $\sigma_{\Delta t}$ is 10 (100) times smaller than $\sigma_{\Delta t} = 1.7$ s, decreases the uncertainty of an $\hat{\alpha}_0$ measure by a factor, which averaged over both the detection Scenarios and the observations numbers with $N_{\rm obs} \gtrsim 10$, is equal to ~ 0.1 (0.035). Meanwhile, we find that using more sensitive detectors will improve the constraints on $\hat{\alpha}_0$. Specifically, O5 will be able to constrain $\hat{\alpha}_0$ 2 times better than O4, while ET will constrain it 5 times better.

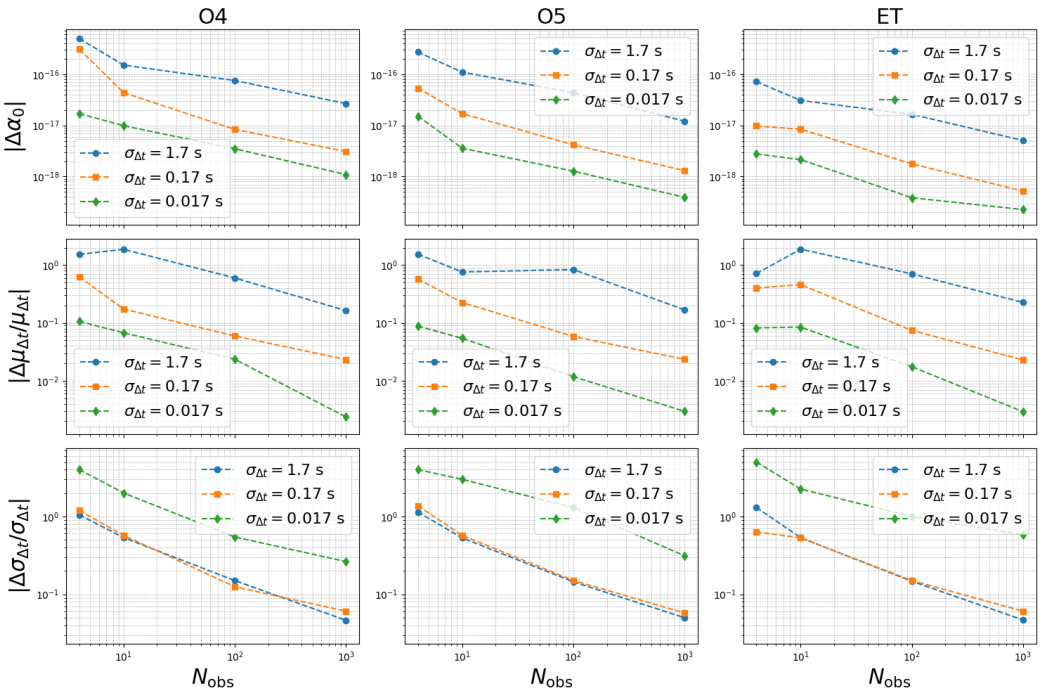

Figure 5.2. Precision for Scenario I on the population parameters when we combine more and more joint GW-sGRB detections. Each row of subplots represents a deduced population parameter $(\hat{\alpha}_0, \mu_{\Delta t}, \sigma_{\Delta t})$ while each column represents a distinct configuration of the detector network (O4, O5, ET). Each subplot shows 3 curves; one for each prompt time delay model ($\sigma_{\Delta t} = [1.7, 0.17, 0.017]$ s).

The measures of the prompt time delay mean $\mu_{\Delta t}$ and standard deviation $\sigma_{\Delta t}$ are constrained with an uncertainty of $\sim 0.6 - 0.01$ s and $\sim 0.5 - 0.005$ s respectively. As for $\hat{\alpha}_0$, the strength of these constraints depends on both $N_{\rm obs}$ and the prompt time delay model Scenarios.

Also, we find that, for the $\sigma_{\Delta t} = 1.7$ s Scenario, the Gaussian convergence is qualitatively reached when $N_{\rm obs} \gtrsim 100$ and $N_{\rm obs} \gtrsim 10$ for $\mu_{\Delta t}$ and $\sigma_{\Delta t}$ respectively. This result holds true for all detector network configurations and it implies that with 4 detected events we will not be able to jointly constrain the speed of gravity and prompt time delay distribution.

From our results, we derive that, for the $\sigma_{\Delta t} = 0.17$ s Scenario, $\mu_{\Delta t}$ and $\sigma_{\Delta t}$ reach the asymptotic regime when $N_{\rm obs} \gtrsim 10$ and $N_{\rm obs} \gtrsim 4$.

While, for the $\sigma_{\Delta t} = 0.017$ s Scenario, the Gaussian regime is reached when $N_{\rm obs} \gtrsim 4$ for both prompt time delay population parameters.

The uncertainty of the ($\mu_{\Delta t}$, $\sigma_{\Delta t}$) measurements varies with the "sharpness" of the prompt time delay distribution in the same way as the uncertainty of $\hat{\alpha}_0$.

Moreover, from Fig. 5.2, we conclude that the constraints on the prompt time delay population parameters are almost independent of the GW detector sensitivities.

As an example, in Fig.5.3, we present the joint posterior distribution for 100 events detected by ET. The interplay between source-frame time delay parameters and the speed of gravity is clearly evident in Fig.5.3. The posterior distribution exhibits a

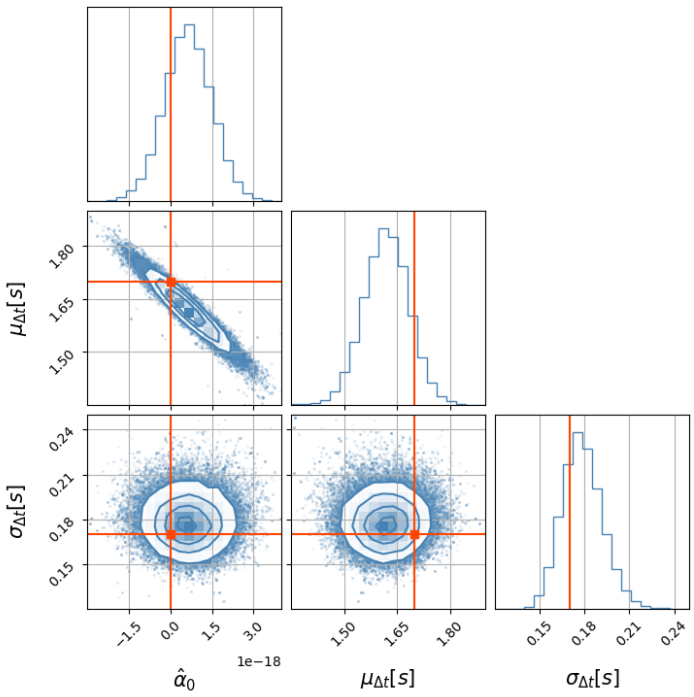

Figure 5.3. Joint and marginalized posterior distributions for $\hat{\alpha}_0$, $\mu_{\Delta t}$ and $\sigma_{\Delta t}$ in the case of 100 events detected by ET and true value of $\sigma_{\Delta t} = 0.17$ s. The orange lines represent the true value of the parameters.

strong correlation between the determination of $\hat{\alpha}_0$ and $\mu_{\Delta t}$. Indeed, the determination of $\mu_{\Delta t}$ influences the estimation of $\hat{\alpha}_0$ in the following way: considering the expression of the detected time delay, as shown in Section 1.3, a lower $\hat{\alpha}_0$ must be compensated by a higher source-frame time delay to keep the observed time delay value fixed at its detected value.

5.3 Scenario II: Cosmology and Prompt Time Delay

For Scenario II, we find that we will be able to constrain H_0 with hostless joint GW-sGRB detections. In Tab. 5.3 we report our measurements of $(H_0, \mu_{\Delta t}, \sigma_{\Delta t})$ while Figure 5.4 shows the error on these parameters. Again, all parameters are recovered to within 3σ of their true values. By observing the marginalized posterior distribution for H_0, we find that, for the $\sigma_{\Delta t} = 1.7$ s scenario, we will not be able to measure the Hubble constant.
However, for the $\sigma_{\Delta t} = 0.17$ s scenario, we will be able to measure H_0 with $N_{obs} \gtrsim 1000$ for O4-O5 and $N_{obs} \gtrsim 100$ for ET.
Finally, for the $\sigma_{\Delta t} = 0.017$ s scenario, we find that even for 100 events detected by O5 it might be possible to constrain H_0 with this method.
As an example, for $N_{\rm obs} = 1000$, ET and $\sigma_{\Delta t} = 0.017$ s, we obtain a value for the Hubble constant of $H_0 = 64.70^{+1.14}_{-1.12} \frac{\rm km}{s\ \rm Mpc}$. In general, from Tab. 5.3, we observe that the constraining power on H_0 increases as the detector network sensitivity improves.

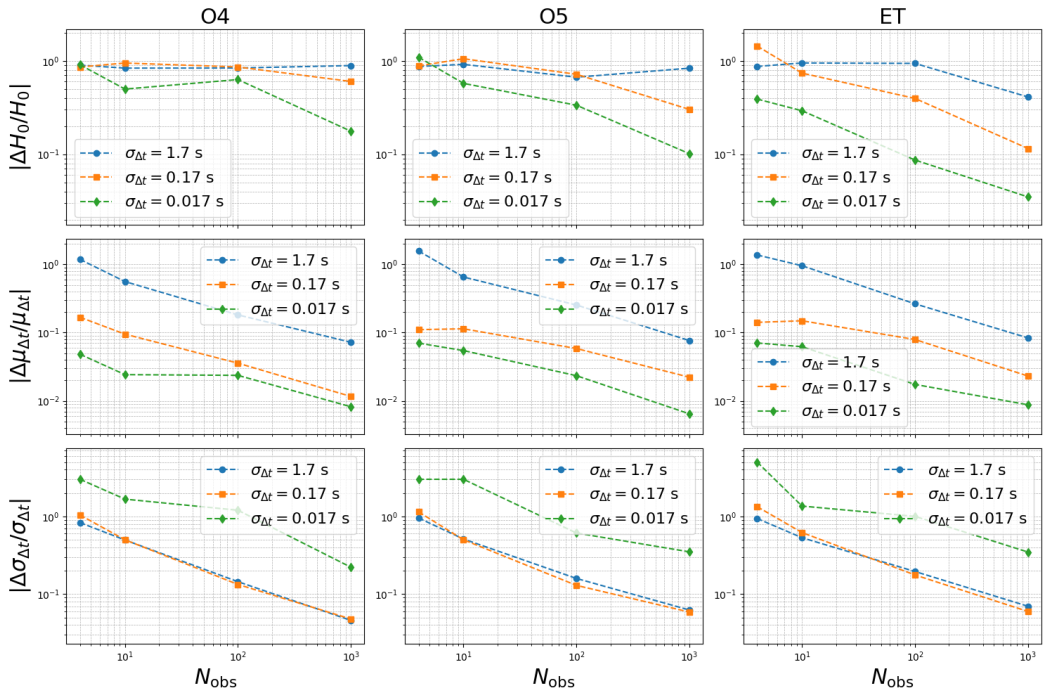

Figure 5.4. Precision for Scenario II on the population parameters when we combine more and more joint GW-sGRB detections. Each row of subplots represents a deduced population parameter $(H_0, \mu_{\Delta t}, \sigma_{\Delta t})$ while each column represents a distinct configuration of the detector network (O4, O5, ET). Each subplot shows 3 curves; one for each prompt time delay model ($\sigma_{\Delta t} = [1.7, 0.17, 0.017]$ s).

Using the O4 scenario as a benchmark, we find that for O5 (ET) the uncertainty on the H_0 measurement decreases by an average factor of ~ 0.6 (0.2). Instead, with respect to the $\sigma_{\Delta t} = 0.17$ s Scenario, we find that, if $\sigma_{\Delta t}$ is 10 times smaller, the uncertainty of an H_0 measurement decreases by an average factor of ~ 0.3.
The prompt time delay parameters $\mu_{\Delta t}$ and $\sigma_{\Delta t}$ are constrained with an uncertainty of $\sim 0.2 - 0.008$ s and $\sim 0.5 - 0.002$ s, respectively. These values depend on the number of detected events and the prompt time delay distribution.
By comparing Fig. 5.4 with Fig. 5.2, we find that the qualitative behavior for these two parameters is analogous to what was found in Scenario I. In Fig. 5.5, we show the joint posterior distribution for 100 events detected by ET. The posterior distribution shows a strong correlation between the measurement of H_0 and $\mu_{\Delta t}$.
We remind the reader that, for this inference Scenario, $\hat{\alpha}_0$ is fixed to its GR value $\hat{\alpha}_0 = 0$. Thus, the observed time delay simplifies to (see Section 1.3):

$$\Delta t_d = \Delta t_s (1 + z). \tag{5.1}$$

As a consequence, since lower H_0 values lead the observed BNS to lower redshifts, $\mu_{\Delta t}$ must increase to keep Δt_d fixed to its detected value.
In general, we also observe a weak correlation for the pairs (H_0, $\sigma_{\Delta t}$) and ($\mu_{\Delta t}$, $\sigma_{\Delta t}$). In fact, a larger H_0 results in a larger spread of the BNS redshifts. Then, (see Eq. 5.1) an increase in H_0 also widens the spread of Δt_d beyond the actual observed range. To reconcile this, the standard deviation of the prompt time delays

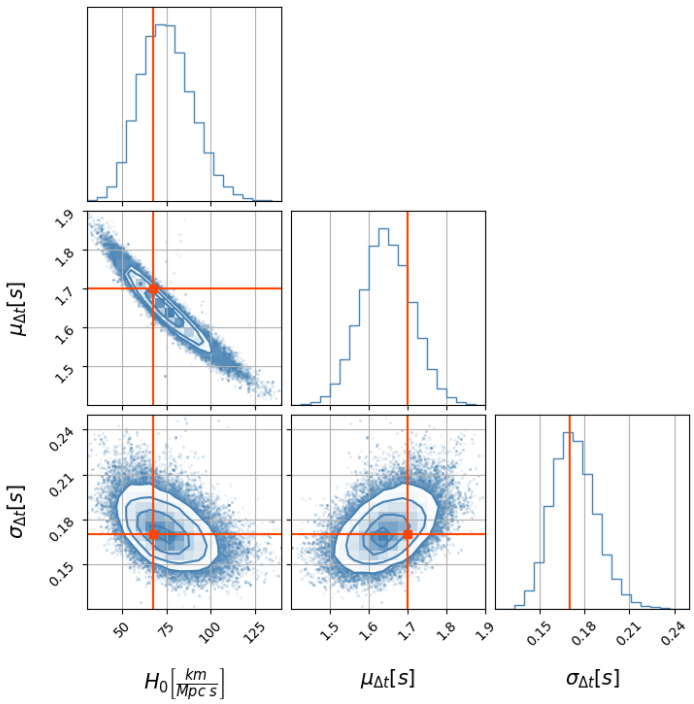

Figure 5.5. Joint and marginalized posterior distributions for H_0, $\mu_{\Delta t}$ and $\sigma_{\Delta t}$ in the case of 100 events detected by ET and true value of $\sigma_{\Delta t} = 0.17$ s. The orange lines represent the true value of the parameters.

$\sigma_{\Delta t}$ needs to be reduced. Then H_0 is correlated with both $\mu_{\Delta t}$ and $\sigma_{\Delta t}$: this induces a correlation between them in the marginalized posterior distribution.

5.4 Scenario III: Cosmology, Speed of Gravity and Prompt Time Delay

For Scenario III, we find that we will be unable to jointly constrain all four population parameters. In Tab. 5.4, we report our measurements of $(\hat{\alpha}_0, H_0, \mu_{\Delta t}, \sigma_{\Delta t})$ while Figure 5.6 displays the error on these parameters obtained from analyzing more GW-sGRB events. All parameters are recovered to within 3σ of their true values. The parameters $\hat{\alpha}_0$,$\mu_{\Delta t}$ and $\sigma_{\Delta t}$ are constrained with uncertainty of $\sim 2 \cdot 10^{-16} - 5 \cdot 10^{-19}$, $\sim 0.5 - 0.005$ s and $\sim 0.5 - 0.005$ s respectively. These values depend on the number of observed events, the detector network and the prompt time delay model.
By observing both Fig. 5.6 and 5.2, we derive that the qualitative behavior of these three parameters is analogous to what was found in Scenario I. Specifically, by observing the marginalized probability density functions for $\hat{\alpha}_0$, we deduce that the Gaussian regime is qualitatively reached when $N_{\rm obs} \gtrsim 4$ for all detection and prompt time delay model scenarios.
Instead, for H_0, we find that, for each detector and prompt time delay model Scenario, we will not be able to measure the Hubble constant since $N_{obs} = 1000$ detected events are not sufficient to reach Gaussian convergence.

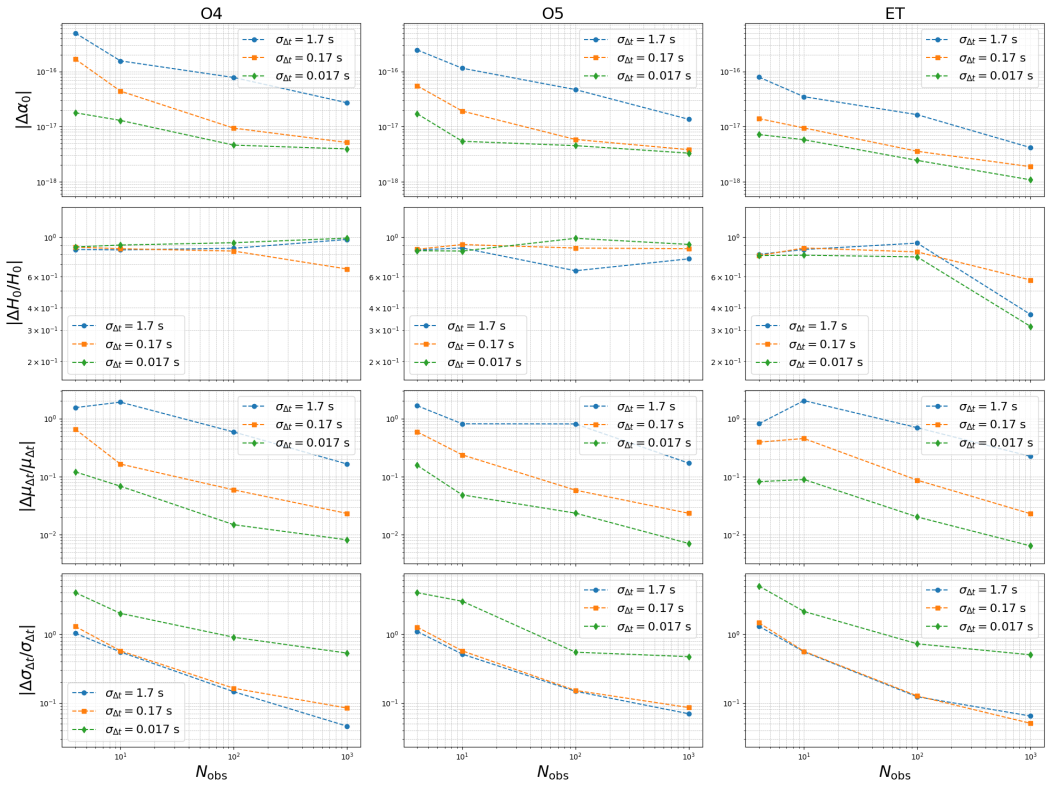

Figure 5.6. Precision for Scenario III on the population parameters when we combine more and more joint GW-sGRB detections. Each row of subplots represents a deduced population parameter $(\hat{\alpha}_0, H_0, \mu_{\Delta t}, \sigma_{\Delta t})$ while each column represents a distinct configuration of the detector network (O4, O5, ET). Each subplot shows 3 curves; one for each prompt time delay model ($\sigma_{\Delta t} = [1.7, 0.17, 0.017]$ s).

This is a consequence of the fact that the marginalization on $\hat{\alpha}_0$ is contributing to the error budget of H_0 and vice versa. In other words, the Cosmology and the GW speed are correlated with each other. The two parameters are degenerate, since different combinations of their values can result in the same observed time delay. We can easily understand how this degeneracy leads to the $(\hat{\alpha}_0, H_0)$ correlation by drawing parallels to the correlations of the $(\hat{\alpha}_0, \mu_{\Delta t})$ and $(H_0, \mu_{\Delta t})$ pairs discussed in the previous 2 inference Scenarios. As an example, In Fig.5.7, we show the joint posterior distribution for 100 events detected by ET.

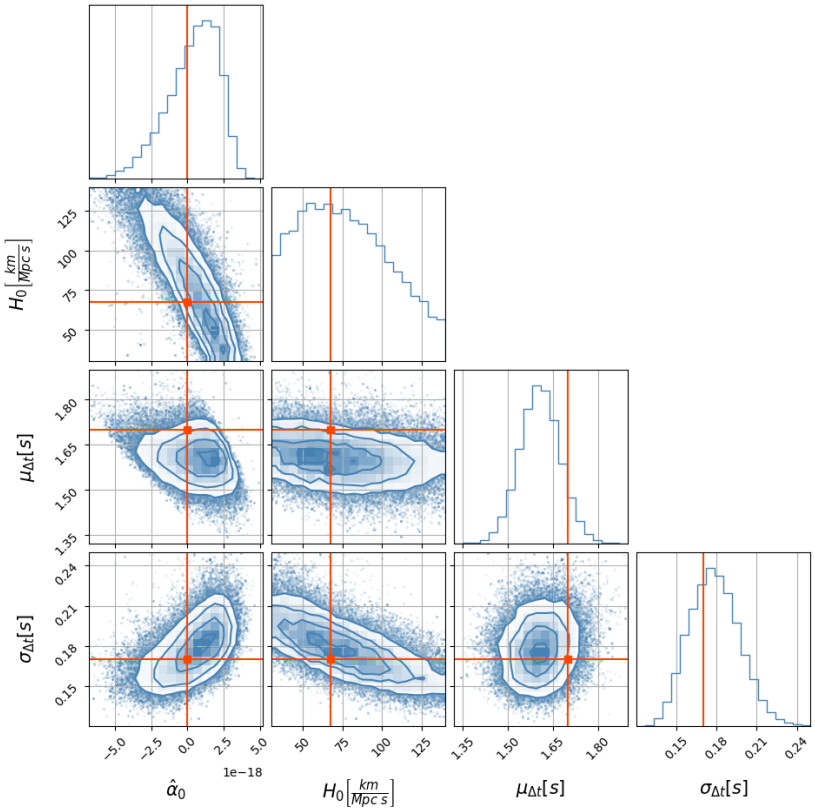

Figure 5.7. Joint and marginalized posterior distributions for $\hat{\alpha}_0$, H_0, $\mu_{\Delta t}$ and $\sigma_{\Delta t}$ in the case of 100 events detected by ET and true value of $\sigma_{\Delta t} = 0.17$ s. The orange lines represent the true value of the parameters.

Table 5.2. Parameter measurement results for Scenario I. We divide the measurements by number of observation N_{obs}, and detection (O4, O5, ET) and prompt time delay model ($\sigma_{\Delta t} = [1.7, 0.17, 0.017]$ s) Scenario. If the "-" symbol appears, it means that Gaussian convergence was not reached for the inferred parameter.

$\sigma_{\Delta t} = 1.7$ s				
$N_{\rm obs}$	Detector Network	$\hat{\alpha}_0 \cdot 10^{-16}$	$\mu_{\Delta t}$ [s]	$\sigma_{\Delta t}$ [s]
4	O4	-0.15 ± 2.47	–	–
	O5	-0.80 ± 1.35	–	–
	ET	-0.388 ± 0.357	–	–
10	O4	1.39 ± 0.75	–	$1.42^{+0.45}_{-0.31}$
	O5	-0.515 ± 0.547	–	$2.15^{+0.68}_{-0.46}$
	ET	-0.040 ± 0.153	–	$1.37^{+0.43}_{-0.30}$
100	O4	0.318 ± 0.375	$1.45^{+0.43}_{-0.44}$	$1.60^{+0.13}_{-0.11}$
	O5	0.125 ± 0.217	$1.18^{+0.50}_{-0.49}$	$1.80^{+0.14}_{-0.12}$
	ET	-0.0139 ± 0.0819	$1.70^{+0.59}_{-0.61}$	$1.77^{+0.14}_{-0.12}$
1000	O4	-0.215 ± 0.133	$1.90^{+0.16}_{-0.15}$	$1.73^{+0.04}_{-0.04}$
	O5	-0.0289 ± 0.0603	$1.78^{+0.15}_{-0.15}$	$1.60^{+0.04}_{-0.04}$
	ET	0.0143 ± 0.0253	$1.68^{+0.19}_{-0.19}$	$1.71^{+0.04}_{-0.04}$

$\sigma_{\Delta t} = 0.17$ s				
$N_{\rm obs}$	Detector Network	$\hat{\alpha}_0 \cdot 10^{-16}$	$\mu_{\Delta t}$ [s]	$\sigma_{\Delta t}$ [s]
4	O4	0.01 ± 1.52	–	$0.31^{+0.25}_{-0.12}$
	O5	0.009 ± 0.267	–	$0.19^{+0.18}_{-0.08}$
	ET	-0.0500 ± 0.0487	–	$0.03^{+0.06}_{-0.03}$
10	O4	-0.396 ± 0.217	$2.18^{+0.19}_{-0.19}$	$0.21^{+0.07}_{-0.05}$
	O5	-0.133 ± 0.085	$2.08^{+0.23}_{-0.24}$	$0.21^{+0.07}_{-0.05}$
	ET	0.0416 ± 0.0420	$1.39^{+0.32}_{-0.32}$	$0.34^{+0.11}_{-0.07}$
100	O4	0.0087 ± 0.0416	$1.68^{+0.05}_{-0.05}$	$0.16^{+0.01}_{-0.01}$
	O5	0.0095 ± 0.0208	$1.71^{+0.05}_{-0.05}$	$0.166^{+0.013}_{-0.12}$
	ET	0.00638 ± 0.00886	$1.62^{+0.06}_{-0.06}$	$0.180^{+0.010}_{-0.015}$
1000	O4	-0.0113 ± 0.0154	$1.72^{+0.02}_{-0.02}$	$0.165^{+0.004}_{-0.006}$
	O5	-0.00404 ± 0.00653	$1.71^{+0.02}_{-0.02}$	$0.174^{+0.005}_{-0.005}$
	ET	-0.00646 ± 0.00261	$1.75^{+0.02}_{-0.02}$	$0.165^{+0.005}_{-0.005}$

$\sigma_{\Delta t} = 0.017$ s				
$N_{\rm obs}$	Detector Network	$\hat{\alpha}_0 \cdot 10^{-16}$	$\mu_{\Delta t}$ [s]	$\sigma_{\Delta t}$ [s]
4	O4	-0.0110 ± 0.0849	$1.69^{+0.10}_{-0.08}$	$0.01^{+0.03}_{-0.01}$
	O5	-0.0342 ± 0.0755	$1.70^{+0.08}_{-0.07}$	$0.01^{+0.03}_{-0.01}$
	ET	0.0008 ± 0.0138	$1.70^{+0.07}_{-0.07}$	$0.01^{+0.04}_{-0.01}$
10	O4	0.0673 ± 0.0492	$1.63^{+0.05}_{-0.06}$	$0.01^{+0.01}_{-0.01}$
	O5	0.0107 ± 0.0179	$1.66^{+0.04}_{-0.05}$	$0.01^{+0.02}_{-0.01}$
	ET	-0.0078 ± 0.0107	$1.77^{+0.07}_{-0.08}$	$0.012^{+0.013}_{-0.004}$
100	O4	-0.0084 ± 0.0175	$1.70^{+0.02}_{-0.02}$	$0.022^{+0.005}_{-0.007}$
	O5	-0.00280 ± 0.00638	$1.70^{+0.01}_{-0.01}$	$0.010^{+0.009}_{-0.004}$
	ET	-0.00232 ± 0.00193	$1.72^{+0.02}_{-0.01}$	$0.014^{+0.010}_{-0.004}$
1000	O4	-0.00070 ± 0.00547	$1.698^{+0.002}_{-0.002}$	$0.019^{+0.002}_{-0.003}$
	O5	0.00223 ± 0.00197	$1.715^{+0.002}_{-0.002}$	$0.016^{+0.0004}_{-0.0001}$
	ET	-0.00298 ± 0.00113	$1.720^{+0.003}_{-0.007}$	$0.012^{+0.006}_{-0.002}$

Table 5.3. Parameter measurement results for Scenario II. We divide the measurements by number of observation N_{obs}, and detection (O4, O5, ET) and prompt time delay model ($\sigma_{\Delta t} = [1.7, 0.17, 0.017]$ s) Scenario. If the "-" symbol appears, it means that Gaussian convergence was not reached for the inferred parameter.

$\sigma_{\Delta t} = 1.7$ s				
$N_{\rm obs}$	Detector Network	H_0 [km/s/Mpc]	$\mu_{\Delta t}$ [s]	$\sigma_{\Delta t}$ [s]
4	O4	–	–	–
	O5	–	–	–
	ET	–	–	–
10	O4	–	–	$1.73^{+0.51}_{-0.35}$
	O5	–	–	$2.23^{+0.68}_{-0.46}$
	ET	–	–	$1.28^{+0.40}_{-0.28}$
100	O4	–	$1.76^{+0.16}_{-0.16}$	$1.59^{+0.12}_{-0.11}$
	O5	–	$1.42^{+0.18}_{-0.18}$	$1.76^{+0.15}_{-0.13}$
	ET	–	$1.63^{+0.22}_{-0.21}$	$1.79^{+0.18}_{-0.17}$
1000	O4	–	$1.66^{+0.06}_{-0.06}$	$1.74^{+0.04}_{-0.04}$
	O5	–	$1.70^{+0.06}_{-0.07}$	$1.60^{+0.05}_{-0.05}$
	ET	–	$1.91^{+0.08}_{-0.08}$	$1.86^{+0.06}_{-0.07}$

$\sigma_{\Delta t} = 0.17$ s				
$N_{\rm obs}$	Detector Network	H_0 [km/s/Mpc]	$\mu_{\Delta t}$ [s]	$\sigma_{\Delta t}$ [s]
4	O4	–	$1.55^{+0.13}_{-0.13}$	$0.24^{+0.17}_{-0.08}$
	O5	–	$1.72^{+0.10}_{-0.09}$	$0.14^{+0.11}_{-0.05}$
	ET	–	$1.91^{+0.09}_{-0.18}$	$0.05^{+0.06}_{-0.04}$
10	O4	–	$1.79^{+0.09}_{-0.08}$	$0.26^{+0.08}_{-0.05}$
	O5	–	$1.67^{+0.09}_{-0.10}$	$0.24^{+0.07}_{-0.05}$
	ET	–	$1.61^{+0.21}_{-0.15}$	$0.31^{+0.11}_{-0.08}$
100	O4	–	$1.68^{+0.03}_{-0.03}$	$0.15^{+0.01}_{-0.01}$
	O5	–	$1.71^{+0.05}_{-0.05}$	$0.162^{+0.013}_{-0.008}$
	ET	$74.04^{+15.46}_{-13.88}$	$1.64^{+0.07}_{-0.06}$	$0.17^{+0.02}_{-0.01}$
1000	O4	$56.16^{+18.47}_{-15.33}$	$1.72^{+0.01}_{-0.01}$	$0.167^{+0.004}_{-0.004}$
	O5	$62.40^{+9.42}_{-9.43}$	$1.710^{+0.018}_{-0.020}$	$0.170^{+0.005}_{-0.005}$
	ET	$60.59^{+3.53}_{-3.45}$	$1.73^{+0.02}_{-0.02}$	$0.0167^{+0.006}_{-0.004}$

$\sigma_{\Delta t} = 0.017$ s				
$N_{\rm obs}$	Detector Network	H_0 [km/s/Mpc]	$\mu_{\Delta t}$ [s]	$\sigma_{\Delta t}$ [s]
4	O4	–	$1.66^{+0.04}_{-0.04}$	$0.01^{+0.02}_{-0.01}$
	O5	–	$1.71^{+0.06}_{-0.06}$	$0.01^{+0.02}_{-0.01}$
	ET	–	$1.70^{+0.06}_{-0.06}$	$0.01^{+0.04}_{-0.01}$
10	O4	–	$1.65^{+0.03}_{-0.01}$	$0.012^{+0.015}_{-0.005}$
	O5	–	$1.65^{+0.05}_{-0.04}$	$0.01^{+0.02}_{-0.01}$
	ET	–	$1.77^{+0.10}_{-0.12}$	$0.014^{+0.015}_{-0.004}$
100	O4	–	$1.69^{+0.02}_{-0.02}$	$0.010^{+0.009}_{-0.003}$
	O5	$60.44^{+9.93}_{-10.31}$	$1.71^{+0.02}_{-0.02}$	$0.018^{+0.008}_{-0.003}$
	ET	$63.69^{+2.81}_{-2.71}$	$1.72^{+0.02}_{-0.01}$	$0.015^{+0.012}_{-0.003}$
1000	O4	$68.02^{+6.10}_{-5.91}$	$1.705^{+0.007}_{-0.007}$	$0.018^{+0.002}_{-0.002}$
	O5	$70.50^{+3.95}_{-3.20}$	$1.702^{+0.007}_{-0.004}$	$0.020^{+0.004}_{-0.003}$
	ET	$64.70^{+1.14}_{-1.12}$	$1.710^{+0.008}_{-0.007}$	$0.023^{+0.004}_{-0.004}$

Table 5.4. Parameter measurement results for Scenario III. We divide the measurements by number of observation N_{obs}, and detection (O4, O5, ET) and prompt time delay model ($\sigma_{\Delta t} = [1.7, 0.17, 0.017]$ s) Scenario. If the "-" symbol appears, it means that Gaussian convergence was not reached for the inferred parameter.

$\sigma_{\Delta t} = 1.7$ s					
$N_{\rm obs}$	Detector Network	$\hat{\alpha}_0 \cdot 10^{-16}$	H_0 [km/s/Mpc]	$\mu_{\Delta t}$ [s]	$\sigma_{\Delta t}$ [s]
4	O4	-0.11 ± 2.49	–	–	–
	O5	-0.81 ± 1.23	–	–	–
	ET	-0.396 ± 0.396	–	–	–
10	O4	1.39 ± 0.78	–	–	$1.40^{+0.46}_{-0.31}$
	O5	-0.502 ± 0.574	–	–	$2.15^{+0.65}_{-0.45}$
	ET	-0.042 ± 0.175	–	–	$1.30^{+0.43}_{-0.29}$
100	O4	0.300 ± 0.390	–	$1.45^{+0.42}_{-0.43}$	$1.58^{+0.12}_{-0.11}$
	O5	0.089 ± 0.235	–	$1.24^{+0.50}_{-0.50}$	$1.76^{+0.14}_{-0.12}$
	ET	-0.0200 ± 0.0824	–	$1.74^{+0.61}_{-0.60}$	$1.79^{+0.12}_{-0.10}$
1000	O4	-0.193 ± 0.136	–	$1.88^{+0.16}_{-0.15}$	$1.74^{+0.04}_{-0.04}$
	O5	-0.0352 ± 0.0678	–	$1.76^{+0.15}_{-0.15}$	$1.58^{+0.06}_{-0.05}$
	ET	0.0284 ± 0.0208	–	$1.66^{+0.18}_{-0.19}$	$1.86^{+0.06}_{-0.06}$

$\sigma_{\Delta t} = 0.17$ s					
$N_{\rm obs}$	Detector Network	$\hat{\alpha}_0 \cdot 10^{-16}$	H_0 [km/s/Mpc]	$\mu_{\Delta t}$ [s]	$\sigma_{\Delta t}$ [s]
4	O4	0.016 ± 0.838	–	–	$0.31^{+0.28}_{-0.12}$
	O5	-0.002 ± 0.276	–	–	$0.19^{+0.16}_{-0.08}$
	ET	-0.0832 ± 0.0610	–	–	$0.03^{+0.06}_{-0.02}$
10	O4	-0.422 ± 0.220	–	$2.19^{+0.18}_{-0.18}$	$0.21^{+0.07}_{-0.05}$
	O5	-0.159 ± 0.096	–	$2.11^{+0.25}_{-0.25}$	$0.21^{+0.07}_{-0.05}$
	ET	0.0346 ± 0.0473	–	$1.39^{+0.32}_{-0.31}$	$0.32^{+0.11}_{-0.07}$
100	O4	-0.0116 ± 0.0469	–	$1.69^{+0.05}_{-0.05}$	$0.153^{+0.013}_{-0.012}$
	O5	-0.0059 ± 0.0292	–	$1.71^{+0.05}_{-0.05}$	$0.158^{+0.012}_{-0.012}$
	ET	0.0035 ± 0.0179	–	$1.61^{+0.07}_{-0.07}$	$0.182^{+0.008}_{-0.015}$
1000	O4	-0.0277 ± 0.0258	–	$1.72^{+0.02}_{-0.02}$	$0.166^{+0.006}_{-0.008}$
	O5	-0.0067 ± 0.0191	–	$1.71^{+0.02}_{-0.02}$	$0.175^{+0.005}_{-0.010}$
	ET	0.00558 ± 0.00937	–	$1.74^{+0.02}_{-0.02}$	$0.178^{+0.005}_{-0.004}$

$\sigma_{\Delta t} = 0.017$ s					
$N_{\rm obs}$	Detector Network	$\hat{\alpha}_0 \cdot 10^{-16}$	H_0 [km/s/Mpc]	$\mu_{\Delta t}$ [s]	$\sigma_{\Delta t}$ [s]
4	O4	-0.0453 ± 0.0892	–	$1.74^{+0.10}_{-0.11}$	$0.01^{+0.03}_{-0.01}$
	O5	-0.0459 ± 0.0857	–	$1.79^{+0.15}_{-0.13}$	$0.01^{+0.03}_{-0.01}$
	ET	-0.0163 ± 0.0260	–	$1.71^{+0.07}_{-0.07}$	$0.01^{+0.04}_{-0.01}$
10	O4	0.0607 ± 0.0648	–	$1.61^{+0.06}_{-0.05}$	$0.01^{+0.02}_{-0.00}$
	O5	0.0039 ± 0.0271	–	$1.65^{+0.04}_{-0.04}$	$0.01^{+0.02}_{-0.01}$
	ET	-0.0277 ± 0.0289	–	$1.79^{+0.07}_{-0.09}$	$0.015^{+0.03}_{-0.002}$
100	O4	-0.0049 ± 0.0231	–	$1.68^{+0.015}_{-0.010}$	$0.020^{+0.012}_{-0.006}$
	O5	-0.0111 ± 0.0226	–	$1.70^{+0.02}_{-0.02}$	$0.022^{+0.008}_{-0.004}$
	ET	0.0069 ± 0.0122	–	$1.73^{+0.015}_{-0.02}$	$0.018^{+0.06}_{-0.06}$
1000	O4	-0.0105 ± 0.019	–	$1.713^{+0.008}_{-0.006}$	$0.017^{+0.006}_{-0.003}$
	O5	0.0047 ± 0.0165	–	$1.695^{+0.005}_{-0.007}$	$0.017^{+0.005}_{-0.003}$
	ET	0.00978 ± 0.00541	–	$1.712^{+0.005}_{-0.006}$	$0.016^{+0.005}_{-0.003}$

Conclusion

In this thesis I studied if it will be possible to constrain the speed of gravity, the universe expansion, and prompt time delay distribution from joint GWsGRB observations. The results obtained allow us to conclude that it will be possible to jointly constrain the speed of gravity and prompt time delay distribution and to infer the Hubble constant without the need for a redshift measurement.

I began this dissertation by presenting the background knowledge necessary to understand this work: cosmology, GR deviations, GW and sGRB emission from BNS. Then after discussing the detection process of GWs and sGRBs, I presented the procedure followed to generate mock catalogs of joint GW-sGRB detections. I performed extensive simulations, considering 3 possible detection networks (O4,O5, and ET), 3 prompt time delay models Δt_s ($\sigma_{\Delta t} = [1.7, 0.17, 0.017]$ s), and 4 different observing scenarios with 4, 10, 100, and 1000 joint GW-sGRB detections. For each case, I generated realistic errors on the luminosity distance estimates and on the observed time delay between GWs and sGRBs. I then used these catalogs to jointly infer the speed of gravity, the prompt time delay distribution, and the Hubble constant.

First, we observe that for all catalogs and inference Scenarios, the parameters' true values lie within a 3σ confidence region of the posterior. Also, we find that a "sharper" prompt time delay distribution (smaller $\sigma_{\Delta t}$) increases the constraints on all 4 parameters. Meanwhile, enhancing the sensitivity of the GW detector network only increases the constraints for the speed of gravity $\hat{\alpha}_0$ and cosmology H_0.

In general, the results show that, for $N_{\rm obs} \gtrsim 100$, we will be able to jointly constrain the speed of gravity and the prompt time delays across all detector sensitivities and prompt time delay distribution models. In fact, $N_{\rm obs} = 4$ detections, while sufficient to constrain the speed of gravity, are insufficient to infer the prompt time delay parameters. As an example, we predict that, with 100 detections observed during O4 and a true value of $\sigma_{\Delta t} = 1.7s$, we will set a constraint on $\hat{\alpha}_0$ of order $O(10^{-17})$ (100 times better than the current measurement from GW170817) and also reconstruct the mean and standard deviation of the Δt_s distribution with 60% and 16% precision respectively.

Furthermore, our study shows, that for specific GW detector networks and prompt time delay distribution models, we will be able to infer the cosmology H_0 without the need for a direct redshift measurement. To set constraints on the Hubble constant, we require a significantly larger dataset $N_{\rm obs} \gtrsim 100$ compared to the speed of gravity case. For instance, with 100 events detected by ET and standard deviation $\sigma_{\Delta t} = 0.17s$, we measure $H_0 = 74.^{+15}_{-14}\ \frac{\rm km}{\rm s\ Mpc}$. The sensitivity of the Einstein Telescope will reach this detection number (we expect ~ 100 joint GW-sGRB detections per year for

ET). In the extreme case of 1000 events detected by ET and standard deviation $\sigma_{\Delta t} = 0.017$ s, we measure $H_0 = 64.70^{+1.14}_{-1.12}\ \frac{\text{km}}{\text{s Mpc}}$. This measure can be combined with the one from other GW sources (e.g. galaxy catalogs) to further improve the H_0 measure.
Finally, by observing the results, we find that, when jointly inferring the cosmology, speed of gravity, and prompt time delay distribution, we will not be able to constrain H_0 for any of the GW-sGRB catalogs considered in this work.
In conclusion, these findings show the potential of applying this new method to future cosmological analyses. As we move forward, with observation runs such as O4, O5, and ET expected to detect numerous GW signals at large redshift, this method could prove to be particularly useful when precise source localization becomes more challenging.

Bibliography

[1] B. P. et al. Abbott. Gw170817: Observation of gravitational waves from a binary neutron star inspiral. *Phys. Rev. Lett.*, 119:161101, Oct 2017.

[2] and B. P. Abbott et al. A gravitational-wave standard siren measurement of the hubble constant. *Nature*, 551(7678):85–88, oct 2017.

[3] S. Ronchini, M. Branchesi, G. Oganesyan, B. Banerjee, U. Dupletsa, G. Ghirlanda, J. Harms, M. Mapelli, and F. Santoliquido. Perspectives for multimessenger astronomy with the next generation of gravitational-wave detectors and high-energy satellites. *Astronomy &amp Astrophysics*, 665:A97, sep 2022.

[4] V. Ferrari, L. Gualtieri, and P. Pani. *General Relativity and Its Applications: Black Holes, Compact Stars and Gravitational Waves*. CRC Press, 2020.

[5] Stefano Ascenzi, Gor Oganesyan, Marica Branchesi, and Riccardo Ciolfi. Electromagnetic counterparts of compact binary mergers. *Journal of Plasma Physics*, 87(1), feb 2021.

[6] S. Mastrogiovanni, D. A. Steer, and M. Barsuglia. Probing modified gravity theories and cosmology using gravitational-waves and associated electromagnetic counterparts. *Physical Review D*, 102(4), aug 2020.

[7] B. P. Abbott others. Gravitational waves and gamma-rays from a binary neutron star merger: GW170817 and GRB 170817a. *The Astrophysical Journal*, 848(2):L13, oct 2017.

[8] George Efstathiou and Steven Gratton. The evidence for a spatially flat universe. *Monthly Notices of the Royal Astronomical Society: Letters*, 496(1):L91–L95, may 2020.

[9] and P. A. R. Ade, N. Aghanim, and M. Arnaud et al. iplanck/i2015 results. *Astronomy &amp Astrophysics*, 594:A13, sep 2016.

[10] Adam G. Riess, Lucas M. Macri, Samantha L. Hoffmann, Dan Scolnic, Stefano Casertano, Alexei V. Filippenko, Brad E. Tucker, Mark J. Reid, David O. Jones, Jeffrey M. Silverman, Ryan Chornock, Peter Challis, Wenlong Yuan, Peter J. Brown, and Ryan J. Foley. A 2.4% DETERMINATION OF THE LOCAL VALUE OF THE HUBBLE CONSTANT. *The Astrophysical Journal*, 826(1):56, jul 2016.

[11] Jose María Ezquiaga and Miguel Zumalacárregui. Dark energy in light of multi-messenger gravitational-wave astronomy. *Frontiers in Astronomy and Space Sciences*, 5, dec 2018.

[12] Omer Bromberg, Ehud Nakar, Tsvi Piran, and Re'em Sari. THE PROPAGATION OF RELATIVISTIC JETS IN EXTERNAL MEDIA. *The Astrophysical Journal*, 740(2):100, oct 2011.

[13] Davide Lazzati and Rosalba Perna. Jet–cocoon outflows from neutron star mergers: Structure, light curves, and fundamental physics. *The Astrophysical Journal*, 881(2):89, aug 2019.

[14] O. S. Salafia, C. Barbieri, S. Ascenzi, and M. Toffano. Gamma-ray burst jet propagation, development of angular structure, and the luminosity function. *Astronomy &amp Astrophysics*, 636:A105, apr 2020.

[15] J. M. Lattimer and D. N. Schramm. Black-Hole-Neutron-Star Collisions. , 192:L145, September 1974.

[16] E. Symbalisty and D. N. Schramm. Neutron Star Collisions and the r-Process. , 22:143, January 1982.

[17] Ehud Nakar and Tsvi Piran. Detectable radio flares following gravitational waves from mergers of binary neutron stars. , 478(7367):82–84, October 2011.

[18] Katharine C. Walker, Bradley E. Schaefer, and E. E. Fenimore. Gamma-Ray Bursts Have Millisecond Variability. , 537(1):264–269, July 2000.

[19] Chryssa Kouveliotou, Charles A. Meegan, Gerald J. Fishman, Narayana P. Bhat, Michael S. Briggs, Thomas M. Koshut, William S. Paciesas, and Geoffrey N. Pendleton. Identification of Two Classes of Gamma-Ray Bursts. , 413:L101, August 1993.

[20] M. S. Briggs, D. L. Band, R. M. Kippen, R. D. Preece, C. Kouveliotou, J. van Paradijs, G. H. Share, R. J. Murphy, S. M. Matz, A. Connors, C. Winkler, M. L. McConnell, J. M. Ryan, O. R. Williams, C. A. Young, B. Dingus, J. R. Catelli, and R. A. M. J. Wijers. Observations of GRB 990123 by theicompton gamma ray observatory/i. *The Astrophysical Journal*, 524(1):82–91, oct 1999.

[21] A. A. Abdo and Fermi GBM Collaboration et al. Ackermann, Fermi LAT Collaboration. Fermi Observations of High-Energy Gamma-Ray Emission from GRB 080916C. *Science*, 323(5922):1688, March 2009.

[22] James E. Rhoads. How to tell a jet from a balloon: A proposed test for beaming in gamma-ray bursts. *The Astrophysical Journal*, 487(1):L1–L4, sep 1997.

[23] James E. Rhoads. The dynamics and light curves of beamed gamma-ray burst afterglows. *The Astrophysical Journal*, 525(2):737–749, nov 1999.

[24] D. A. Frail, S. R. Kulkarni, R. Sari, S. G. Djorgovski, J. S. Bloom, T. J. Galama, D. E. Reichart, E. Berger, F. A. Harrison, P. A. Price, S. A. Yost, A. Diercks,

R. W. Goodrich, and F. Chaffee. Beaming in gamma-ray bursts: Evidence for a standard energy reservoir. *The Astrophysical Journal*, 562(1):L55–L58, nov 2001.

[25] E NAKAR. Short-hard gamma-ray bursts. *Physics Reports*, 442(1-6):166–236, apr 2007.

[26] A. Panaitescu, P. Kumar, and R. Narayan. Observational prospects for afterglows of short-duration gamma-ray bursts. *The Astrophysical Journal*, 561(2):L171–L174, nov 2001.

[27] E. Berger. THE HOST GALAXIES OF SHORT-DURATION GAMMA-RAY BURSTS: LUMINOSITIES, METALLICITIES, AND STAR FORMATION RATES. *The Astrophysical Journal*, 690(1):231–237, dec 2008.

[28] S.E. Woosley and J.S. Bloom. The supernova–gamma-ray burst connection. *Annual Review of Astronomy and Astrophysics*, 44(1):507–556, sep 2006.

[29] A. S. Fruchter, A. J. Levan, L. Strolger, P. M. Vreeswijk, S. E. Thorsett, D. Bersier, I. Burud, J. M. Castro Cerón, A. J. Castro-Tirado, C. Conselice, T. Dahlen, H. C. Ferguson, J. P. U. Fynbo, P. M. Garnavich, R. A. Gibbons, J. Gorosabel, T. R. Gull, J. Hjorth, S. T. Holland, C. Kouveliotou, Z. Levay, M. Livio, M. R. Metzger, P. E. Nugent, L. Petro, E. Pian, J. E. Rhoads, A. G. Riess, K. C. Sahu, A. Smette, N. R. Tanvir, R. A. M. J. Wijers, and S. E. Woosley. Long -ray bursts and core-collapse supernovae have different environments. *Nature*, 441(7092):463–468, may 2006.

[30] Wen-fai Fong, E. Berger, and D. Fox. Hubble Space Telescope Observations of Short GRB Host Galaxies: Morphologies, Offsets and Local Environments. In *American Astronomical Society Meeting Abstracts #215*, volume 215 of *American Astronomical Society Meeting Abstracts*, page 405.01, January 2010.

[31] S. I. Blinnikov, I. D. Novikov, T. V. Perevodchikova, and A. G. Polnarev. Exploding neutron stars in close binaries, 2018.

[32] B. Paczynski. Gamma-ray bursters at cosmological distances. , 308:L43–L46, September 1986.

[33] David Eichler, Mario Livio, Tsvi Piran, and David N. Schramm. Nucleosynthesis, neutrino bursts and γ-rays from coalescing neutron stars. , 340(6229):126–128, July 1989.

[34] Saeed Mirshekari, Nicolá s Yunes, and Clifford M. Will. Constraining lorentz-violating, modified dispersion relations with gravitational waves. *Physical Review D*, 85(2), jan 2012.

[35] B. P. Abbott et al. Multi-messenger observations of a binary neutron star merger*. *The Astrophysical Journal Letters*, 848(2):L12, oct 2017.

[36] A. Goldstein, P. Veres, E. Burns, M. S. Briggs, R. Hamburg, D. Kocevski, C. A. Wilson-Hodge, R. D. Preece, S. Poolakkil, O. J. Roberts, C. M. Hui,

V. Connaughton, J. Racusin, A. von Kienlin, T. Dal Canton, N. Christensen, T. Littenberg, K. Siellez, L. Blackburn, J. Broida, E. Bissaldi, W. H. Cleveland, M. H. Gibby, M. M. Giles, R. M. Kippen, S. McBreen, J. McEnery, C. A. Meegan, W. S. Paciesas, and M. Stanbro. An ordinary short gamma-ray burst with extraordinary implications: Fermi-gbm detection of grb 170817a. *The Astrophysical Journal Letters*, 848(2):L14, oct 2017.

[37] Feryal Özel and Paulo Freire. Masses, radii, and the equation of state of neutron stars. *Annual Review of Astronomy and Astrophysics*, 54(1):401–440, 2016.

[38] T. M. Tauris, M. Kramer, P. C. C. Freire, N. Wex, H.-T. Janka, N. Langer, Ph. Podsiadlowski, E. Bozzo, S. Chaty, M. U. Kruckow, E. P. J. van den Heuvel, J. Antoniadis, R. P. Breton, and D. J. Champion. Formation of double neutron star systems. *The Astrophysical Journal*, 846(2):170, sep 2017.

[39] Wendy L. Freedman, Barry F. Madore, Brad K. Gibson, Laura Ferrarese, Daniel D. Kelson, Shoko Sakai, Jeremy R. Mould, Jr. Robert C. Kennicutt, Holland C. Ford, John A. Graham, John P. Huchra, Shaun M. G. Hughes, Garth D. Illingworth, Lucas M. Macri, and Peter B. Stetson. Final results from the hubble space telescope key project to measure the hubble constant*. *The Astrophysical Journal*, 553(1):47, may 2001.

[40] R. Abbott et al. All-sky search for long-duration gravitational-wave bursts in the third advanced LIGO and advanced virgo run. *Physical Review D*, 104(10), nov 2021.

[41] Curt Cutler and É anna E. Flanagan. Gravitational waves from merging compact binaries: How accurately can one extract the binary's parameters from the inspiral waveform? *Physical Review D*, 49(6):2658–2697, mar 1994.

[42] B. P. Abbott others. Prospects for observing and localizing gravitational-wave transients with advanced LIGO, advanced virgo and KAGRA. *Living Reviews in Relativity*, 23(1), sep 2020.

[43] Michele Maggiore, Chris Van Den Broeck, Nicola Bartolo, Enis Belgacem, Daniele Bertacca, Marie Anne Bizouard, Marica Branchesi, Sebastien Clesse, Stefano Foffa, Juan Garcí a-Bellido, Stefan Grimm, Jan Harms, Tanja Hinderer, Sabino Matarrese, Cristiano Palomba, Marco Peloso, Angelo Ricciardone, and Mairi Sakellariadou. Science case for the einstein telescope. *Journal of Cosmology and Astroparticle Physics*, 2020(03):050–050, mar 2020.

[44] David J. Thompson and Colleen A. Wilson-Hodge. Fermi gamma-ray space telescope. In *Handbook of X-ray and Gamma-ray Astrophysics*, pages 1–31. Springer Nature Singapore, nov 2022.

[45] ET Steering Committee Editorial Team. Design report update 2020. Technical report, Einstein Telescope, September 2020. First release.

[46] Curt Cutler, Theocharis A. Apostolatos, Lars Bildsten, Lee Smauel Finn, Eanna E. Flanagan, Daniel Kennefick, Dragoljub M. Markovic, Amos Ori, Eric

Poisson, Gerald Jay Sussman, and Kip S. Thorne. The last three minutes: Issues in gravitational-wave measurements of coalescing compact binaries. *Phys. Rev. Lett.*, 70:2984–2987, May 1993.

[47] B. S. Sathyaprakash and Bernard F. Schutz. Physics, astrophysics and cosmology with gravitational waves. *Living Reviews in Relativity*, 12(1), mar 2009.

[48] and J Aasi and B P Abbott et al. Advanced LIGO. *Classical and Quantum Gravity*, 32(7):074001, mar 2015.

[49] F Acernese, M Agathos, and K Agatsuma et al. Advanced virgo: a second-generation interferometric gravitational wave detector. *Classical and Quantum Gravity*, 32(2):024001, dec 2014.

[50] K L Dooley, J R Leong, and T Adams et al. GEO 600 and the GEO-HF upgrade program: successes and challenges. *Classical and Quantum Gravity*, 33(7):075009, mar 2016.

[51] T Akutsu, M Ando, and S Araki et al. Construction of KAGRA: an underground gravitational-wave observatory. *Progress of Theoretical and Experimental Physics*, 2018(1), jan 2018.

[52] B. Iyer et al. Ligo-india. Technical Report M1100296-v2, IndIGO, India, 2011.

[53] A. et al. Allocca. Seismic glitchness at Sos Enattos site: impact on intermediate black hole binaries detection efficiency. *European Physical Journal Plus*, 136(5):511, May 2021.

[54] Charles Meegan, Giselher Lichti, P. N. Bhat, Elisabetta Bissaldi, Michael S. Briggs, Valerie Connaughton, Roland Diehl, Gerald Fishman, Jochen Greiner, Andrew S. Hoover, Alexander J. van der Horst, Andreas von Kienlin, R. Marc Kippen, Chryssa Kouveliotou, Sheila McBreen, W. S. Paciesas, Robert Preece, Helmut Steinle, Mark S. Wallace, Robert B. Wilson, and Colleen Wilson-Hodge. THEiFERMI/iGAMMA-RAY BURST MONITOR. *The Astrophysical Journal*, 702(1):791–804, aug 2009.

[55] W. B. Atwood et al. The large area telescope on the fermi gamma-ray space telescope mission. *The Astrophysical Journal*, 697(2):1071, may 2009.

[56] A. von Kienlin, C. A. Meegan, W. S. Paciesas, P. N. Bhat, E. Bissaldi, M. S. Briggs, E. Burns, W. H. Cleveland, M. H. Gibby, M. M. Giles, A. Goldstein, R. Hamburg, C. M. Hui, D. Kocevski, B. Mailyan, C. Malacaria, S. Poolakkil, R. D. Preece, O. J. Roberts, P. Veres, and C. A. Wilson-Hodge. The fourth fermi-gbm gamma-ray burst catalog: A decade of data. *The Astrophysical Journal*, 893(1):46, apr 2020.

[57] L. Amati, P. O'Brien, and D. Götz et al. The THESEUS space mission concept: science case, design and expected performances. *Advances in Space Research*, 62(1):191–244, jul 2018.

[58] L. Amati, P.T. O'Brien, and D. Götz et al. The THESEUS space mission: science goals, requirements and mission concept. *Experimental Astronomy*, 52(3):183–218, nov 2021.

[59] Hsin-Yu Chen and Daniel E. Holz. The loudest gravitational wave events, 2014.

[60] Amanda Farah, Reed Essick, Zoheyr Doctor, Maya Fishbach, and Daniel E. Holz. Counting on short gamma-ray bursts: Gravitational-wave constraints of jet geometry. *The Astrophysical Journal*, 895(2):108, jun 2020.

[61] Bing Zhang. The delay time of gravitational wave — gamma-ray burst associations. *Frontiers of Physics*, 14(6), jul 2019.

[62] G. Ghirlanda, O. S. Salafia, A. Pescalli, G. Ghisellini, R. Salvaterra, E. Chassande–Mottin, M. Colpi, F. Nappo, P. D'Avanzo, A. Melandri, M. G. Bernardini, M. Branchesi, S. Campana, R. Ciolfi, S. Covino, D. Götz, S. D. Vergani, M. Zennaro, and G. Tagliaferri. Short gamma-ray bursts at the dawn of the gravitational wave era. *Astronomy &amp Astrophysics*, 594:A84, oct 2016.

[63] and N. Aghanim, Y. Akrami, and M. Ashdown et al. iplanck/i2018 results. *Astronomy &amp Astrophysics*, 641:A6, sep 2020.

[64] The LIGO Scientific Collaboration, the Virgo Collaboration, the KAGRA Collaboration, and R. Abbott et al. The population of merging compact binaries inferred using gravitational waves through gwtc-3, 2022.

[65] Piero Madau and Mark Dickinson. Cosmic star-formation history. *Annual Review of Astronomy and Astrophysics*, 52(1):415–486, aug 2014.

[66] and Thomas P. Robitaille, Erik J. Tollerud, and Perry Greenfield et al. Astropy: A community python package for astronomy. *Astronomy &amp Astrophysics*, 558:A33, sep 2013.

[67] Koustav Chandra, V. Villa-Ortega, T. Dent, C. McIsaac, Archana Pai, I. W. Harry, G. S. Cabourn Davies, and K. Soni. Optimized PyCBC search for gravitational waves from intermediate-mass black hole mergers. *Physical Review D*, 104(4), aug 2021.

[68] Rosalba Perna, Re'em Sari, and Dale Frail. Jets in gamma-ray bursts: Tests and predictions for the structured jet model. *The Astrophysical Journal*, 594(1):379, sep 2003.

[69] W. Fong, E. Berger, R. Margutti, B. A. Zauderer, E. Troja, I. Czekala, R. Chornock, N. Gehrels, T. Sakamoto, D. B. Fox, and P. Podsiadlowski. A jet break in the x-ray light curve of short grb 111020a: Implications for energetics and rates. *The Astrophysical Journal*, 756(2):189, aug 2012.

[70] W. Fong and E. Berger. The locations of short gamma-ray bursts as evidence for compact object binary progenitors. *The Astrophysical Journal*, 776(1):18, sep 2013.

[71] O. S. Salafia, G. Ghisellini, A. Pescalli, G. Ghirlanda, and F. Nappo. Structure of gamma-ray burst jets: intrinsic versus apparent properties. *Monthly Notices of the Royal Astronomical Society*, 450(4):3549–3558, may 2015.

[72] Ilya Mandel, Will M Farr, and Jonathan R Gair. Extracting distribution parameters from multiple uncertain observations with selection biases. *Monthly Notices of the Royal Astronomical Society*, 486(1):1086–1093, mar 2019.

[73] Simone Mastrogiovanni, Grégoire Pierra, Stéphane Perriès, Danny Laghi, Giada Caneva Santoro, Archisman Ghosh, Rachel Gray, Christos Karathanasis, and Konstantin Leyde. Icarogw: A python package for inference of astrophysical population properties of noisy, heterogeneous and incomplete observations, 2023.

[74] Salvatore Vitale, Davide Gerosa, Will M. Farr, and Stephen R. Taylor. Inferring the Properties of a Population of Compact Binaries in Presence of Selection Effects. In *Handbook of Gravitational Wave Astronomy. Edited by C. Bambi*, page 45. 2022.

[75] Jonathan R. Gair, Archisman Ghosh, Rachel Gray, Daniel E. Holz, Simone Mastrogiovanni, Suvodip Mukherjee, Antonella Palmese, Nicola Tamanini, Tessa Baker, Freija Beirnaert, Maciej Bilicki, Hsin-Yu Chen, Gergely Dálya, Jose Maria Ezquiaga, Will M. Farr, Maya Fishbach, Juan Garcia-Bellido, Tathagata Ghosh, Hsiang-Yu Huang, Christos Karathanasis, Konstantin Leyde, Ignacio Magaña Hernandez, Johannes Noller, Gregoire Pierra, Peter Raffai, Antonio Enea Romano, Monica Seglar-Arroyo, Danièle A. Steer, Cezary Turski, Maria Paola Vaccaro, and Sergio Andrés Vallejo-Peña. The hitchhiker's guide to the galaxy catalog approach for dark siren gravitational-wave cosmology. *The Astronomical Journal*, 166(1):22, jun 2023.

[76] Will M. Farr. Accuracy requirements for empirically measured selection functions. *Research Notes of the AAS*, 3(5):66, may 2019.

[77] R. Abbott, VIRGO Collaboration, and Kagra Collaboration et al. Constraints on the Cosmic Expansion History from GWTC-3. , 949(2):76, June 2023.

[78] B. P. Abbott, The LIGO Scientific Collaboration, and the Virgo Collaboration et al. A gravitational-wave measurement of the hubble constant following the second observing run of advanced ligo and virgo. *The Astrophysical Journal*, 909(2):218, mar 2021.

[79] Gregory et al. Ashton. BILBY: A User-friendly Bayesian Inference Library for Gravitational-wave Astronomy. , 241(2):27, April 2019.

[80] Daniel Foreman-Mackey et al. emcee: The mcmc hammer. *Publications of the Astronomical Society of the Pacific*, 125(925):306–312, 2013.

[81] N Metropolis, AW Rosenbluth, MN Rosenbluth, AH Teller, and E Teller. Equation of state calculations by fast computing machines. *The Journal of Chemical Physics*, 21(6):1087–1092, 1953.

[82] WK Hastings. Monte carlo sampling methods using markov chains and their applications. *Biometrika*, 57(1):97–109, 1970.

[83] Jonathan Goodman and Jonathan Weare. Ensemble samplers with affine invariance. *Communications in applied mathematics and computational science*, 5(1):65–80, 2010.

[84] A. W. van der Vaart. *Asymptotic Statistics*. Cambridge Series in Statistical and Probabilistic Mathematics. Cambridge University Press, 1998.